MgH_2-BASED HYDROGEN AND THERMAL STORAGES

PHUTTHIMET THONGTAN

A Thesis Submitted in Partial Fulfillment of the Requirements for the

Degree of Doctor of Philosophy in Chemistry

Suranaree University of Technology

Academic Year 2023

ตัวกักเก็บไฮโดรเจนและความร้อนที่มีแมกนีเซียมไฮไดรด์เป็นฐาน

นายพุฒิเมธ ทองตัน

วิทยานิพนธ์นี้เป็นส่วนหนึ่งของการศึกษาตามหลักสูตรปริญญาวิทยาศาสตรดุษฎีบัณฑิต

สาขาวิชาเคมี

มหาวิทยาลัยเทคโนโลยีสุรนารี

ปีการศึกษา 2566

MgH_2-BASED HYDROGEN AND THERMAL STORAGES

Suranaree University of Technology has approved this thesis submitted in partial fulfillment of the requirements for the Degree of Doctor of Philosophy.

Thesis Examining Committee

(Assoc. Prof. Dr. Anyanee Kamkaew)
Chairperson

(Assoc. Prof. Dr. Rapee Utke)
Member (Thesis Advisor)

(Dr. Claudio Pistidda)
Member (Thesis Co-advisor)

(Dr. Thi Thu Le)
Member

(Prof. Dr. Jatuporn Wittayakun)
Member

(Assoc. Prof. Dr. Theeranun Siritanon)
Member

(Assoc. Prof. Dr. Yupaporn Ruksakulpiwat)
Vice Rector for Academic Affairs
and Quality Assurance

(Prof. Dr. Santi Maensiri)
Dean of Institute of Science

พุฒิเมธ ทองตัน : ตัวกักเก็บไฮโดรเจนและความร้อนที่มีแมกนีเซียมไฮไดรด์เป็นฐาน (MgH_2-BASED HYDROGEN AND THERMAL STORAGES) อาจารย์ที่ปรึกษา : รองศาสตราจารย์ ดร.ระพี อูทเคอ, 98 หน้า

คำสำคัญ: การกักเก็บไฮโดรเจนชนิดของแข็ง วัสดุไฮไดรด์แมกนีเซียม คาร์บอนกัมมันต์ จลนพลศาสตร์ของปฏิกิริยาการปลดปล่อยไฮโดรเจน การกักเก็บความร้อนจากปฏิกิริยาเคมี

วิทยานิพนธ์เล่มนี้มีจุดประสงค์เพื่อศึกษาและพัฒนาคุณสมบัติในการกักเก็บและปลดปล่อยไฮโดรเจนของวัสดุไฮไดรด์แมกนีเซียม (MgH_2) ในระดับห้องปฏิบัติการและขยายไปสู่ระดับถังกักเก็บ โดยการเติมด้วยตัวเร่งปฏิกิริยาและวัสดุคาร์บอน สำหรับใช้เป็นวัสดุกักเก็บไฮโดรเจนประเภทของแข็ง จากการศึกษาพบว่า การเติมด้วยด้วย TiF_4 และวัสดุคาร์บอนกัมมันต์ช่วยลดอุณหภูมิในการปลดปล่อยไฮโดรเจนของ MgH_2 ลงมากกว่า 100 องศาเซลเซียส โดยมีความจุไฮโดรเจน 4.4 ร้อยละโดยน้ำหนัก ซึ่งต่ำกว่าความจุไฮโดรเจนทางทฤษฎี (6.8 ร้อยละโดยน้ำหนัก) เกิดจากการเกิดปฏิกิริยาที่ไม่สมบูรณ์ การปรับปรุงทำได้โดยการเพิ่มจำนวนชั้นการบรรจุและการใส่ท่อตาข่ายสแตนเลสที่บริเวณกลางถังกักเก็บ ซึ่งช่วยเพิ่มความสามารถในการซึมผ่านของไฮโดรเจนและจลนพลศาสตร์ของการกักเก็บและปลดปล่อยไฮโดรเจน โดยถังกักเก็บที่ปรับปรุงแล้วมีความจุไฮโดรเจน 4.46 ร้อยละโดยน้ำหนัก และมีความจุไฮโดรเจนที่ผันกลับได้ 3.42-3.62 ร้อยละโดยน้ำหนัก นอกจากนี้ยังพบว่าความสามารถในการเกิดปฏิกิริยาของสารตัวอย่างแตกต่างกันออกไปในแต่ละตำแหน่ง ซึ่งเป็นผลมาจากการถ่ายเทความร้อนที่ไม่มีประสิทธิภาพ และการแพร่ผ่านของแก๊สไฮโดรเจนที่ถูกปิดกั้นจากการรวมตัวของอนุภาคของสารตัวอย่างภายในถังกักเก็บ

นอกจากการเติมด้วย TiF_4 และวัสดุคาร์บอนกัมมันต์แล้ว ยังมีการศึกษาการพัฒนาคุณสมบัติการกักเก็บและปลดปล่อยไฮโดรเจนของ MgH_2 โดยการเติมด้วย NbF_5 และวัสดุท่อคาร์บอนระดับนาโนเมตรแบบหลายชั้นที่ปริมาณ 5-10 ร้อยละโดยน้ำหนัก โดยทำการศึกษาด้วยถังกักเก็บขนาด 337.4 มิลลิลิตร พบว่าสารตัวอย่างสามารถเกิดปฏิกิริยาได้ดีที่ตำแหน่งรัศมีกลางถังกักเก็บ เนื่องจากได้รับความร้อนที่เพียงพอจากขดลวดความร้อนที่อยู่ตรงกลางถังกักเก็บ จากคุณสมบัติการนำความร้อนที่ดีของวัสดุท่อคาร์บอนระดับนาโนเมตรแบบหลายชั้น ทำให้สารตัวอย่างที่เติมด้วยวัสดุท่อคาร์บอนระดับนาโนเมตรแบบหลายชั้นปริมาณ 10 ร้อยละโดยน้ำหนัก แสดงการถ่ายเทของความร้อนภายในถังกักเก็บได้ดีกว่า ส่งผลให้สามารถเกิดปฏิกิริยาการกักเก็บและปลดปล่อยไฮโดรเจนที่ดีกว่า โดยสารตัวอย่างที่เติมด้วยวัสดุท่อคาร์บอนระดับนาโนเมตรแบบหลายชั้นปริมาณ 5 และ 10 ร้อยละโดย

ตัวอย่างที่เติมด้วยวัสดุท่อคาร์บอนระดับนาโนเมตรแบบหลายชั้นปริมาณ 5 และ 10 ร้อยละโดยน้ำหนัก มีความจุไฮโดรเจน 2.66 และ 3.39 ร้อยละโดยน้ำหนัก ตามลำดับ อย่างไรก็ตาม ยังพบการถ่ายเทความร้อนที่ไม่ทั่วถึง รวมถึงการรวมตัวของอนุภาคภายในถังกักเก็บหลังเกิดปฏิกิริยา ซึ่งสามารถพัฒนาได้โดยการออกแบบถังกักเก็บและระบบจัดการความร้อนที่มีประสิทธิภาพ

นอกจากการใช้ประโยชน์เป็นวัสดุกักเก็บไฮโดรเจนแล้ว MgH_2 ยังสามารถใช้เป็นวัสดุกักเก็บความร้อนจากปฏิกิริยาเคมีได้อีกด้วย โดยวิทยานิพนธ์นี้ได้ศึกษาการจับคู่กันของ MgH_2 และ $LaNi_5$ ในการใช้เป็นระบบกักเก็บความร้อน โดย MgH_2 ทำหน้าที่เป็นวัสดุกักเก็บความร้อน ส่วน $LaNi_5$ ทำหน้าที่กักเก็บไฮโดรเจน และใช้อากาศเป็นวัสดุถ่ายเทความร้อน ผลการทดลองแสดงให้เห็นความเสถียรตลอดการเก็บความร้อนจำนวน 16 รอบ โดยปริมาณไฮโดรเจนที่แลกเปลี่ยนระหว่าง MgH_2 และ $LaNi_5$ มีค่า 0.82 ± 0.02 โมลไฮโดรเจน หรือ 4.14 ± 0.2 ร้อยละโดยน้ำหนัก ซึ่งมีค่าประมาณร้อยละ 86 ของความจุเริ่มต้นของ MgH_2 (4.78 ร้อยละโดยน้ำหนัก) พลังงานความร้อนที่ได้รับระหว่างการกักเก็บและปลดปล่อยคือ 1406 ± 31 และ 1513 ± 36 กิโลจูลต่อกิโลกรัม ตามลำดับ เมื่อคำนวณพลังงานความร้อนที่วัสดุถ่ายเทความร้อนสามารถนำออกมาได้ พบว่ามีค่า 1583 ± 91 กิโลจูลต่อกิโลกรัม

สาขาวิชาเคมี ลายมือชื่อนักศึกษา _____

ปีการศึกษา 2566 ลายมือชื่ออาจารย์ที่ปรึกษา _____

PHUTTHIMET THONGTAN : MgH_2-BASED HYDROGEN AND THERMAL STORAGES. THESIS ADVISOR : ASSOC. PROF. RAPEE UTKE, Ph.D. 98 PP.

Keywords: Solid-state hydrogen storage, Mg-based hydride materials, Activated carbon, Dehydrogenation kinetics, Thermochemical storage

This thesis investigates the development of hydrogen storage properties of magnesium hydride (MgH_2) by doping with catalysts and carbon materials in laboratory and tank scales. MgH_2 doped with TiF_4 and activated carbon (AC) demonstrates the notable reduction in dehydrogenation temperatures, although incomplete hydrogenation during sample preparation degrades hydrogen capacity to 4.4 wt. % H_2. Improvements are made by increasing the number of hydride beds and inserting the stainless-steel mesh tubes at the tank center. This enhances hydrogen permeability and de/rehydrogenation kinetics. Initial cycles exhibit gravimetric and volumetric capacities of 4.46 wt. % H_2 and 28 gH_2/L, respectively. Upon cycling, the capacities stabilize at 3.42-3.62 wt. % H_2 and 22-23 gH_2/L, respectively. Despite homogeneous heat transfer along the tank radius, the decayed hydrogen permeability towards the tank wall results in inferior kinetics. Challenges relating to particle sintering and/or agglomeration upon cycling are responsible for the inferior hydrogen content.

MgH_2 doped with NbF_5 and 5-10 wt. % MWCNTs exhibits superior de/rehydrogenation kinetics in tank scale. Optimal performance is observed at the middle positions due to effective heat supply and hydrogen diffusion. Increasing MWCNTs content up to 10 wt. % significantly improvs hydrogen de/absorption kinetics at all tank positions. This elevates the hydrogen capacities over multiple cycles. Suggestions for tank design and fabrication with superior heat exchanger and gas diffusion pathways are proposed to address these issues.

Additionally, the experimental study of coupled MgH_2-Nb_2O_5-Graphite (HTMH) with $LaNi_5H_6$ (LTMH) thermochemical storage is carried out. The temperature, pressure, and H_2 flow rate behaviors during the heat storage/release reaction, energy storage

and H_2 flow rate behaviors during the heat storage/release reaction, energy storage density as well as the cycling stability are investigated. Thermal storage system demonstrates stability over 16 heat storage cycles. Hydrogen contents exchanged between HTMH and LTMH are up to 4.14 ± 0.2 wt. % H_2. Approximately 86% of the theoretical capacity of HTMH (4.78 wt. % H_2) participates in the heat storage cycles. The obtained heat storage densities during discharging and charging are 1406 ± 31 and 1513 ± 36 kJ/kg, respectively. The calculated heat storage density based on temperature changes of the heat transfer fluid (compressed air) used during heat discharging is 1583 ± 91 kJ/kg.

School of Chemistry
Academic Year 2023

Student's Signature _____
Advisor's Signature _____

ACKNOWLEDGEMENT

The completion of this thesis would not have been possible without the support and guidance. A special acknowledgment goes to my esteemed advisor, Assoc. Prof. Dr. Rapee Utke for her invaluable guidance, support, and encouragement throughout my research journey. Her mentorship and expertise have been instrumental in my development as a researcher. I am grateful for her patience and understanding during challenging times, and for always believing in my potential.

I would like to express my sincere gratitude to the School of Chemistry, Suranaree University of Technology for providing me with the opportunity to pursue my research and for the excellent resources and facilities.

I express my gratitude to Helmholtz Zentrum Hereon, Germany, for providing a conducive research environment. Heartfelt appreciation is extended to Dr. Claudio Pistidda, my co-advisor from Helmholtz Zentrum Hereon, for his insightful feedback, encouragement, and support during my research abroad. Special thanks to Dr. Thi Thu Le and other colleagues at Hereon for their collaboration, support, and friendship during my research stay in Germany.

I am truly grateful for financial support from the Royal Golden Jubilee (RGJ) for awarding me this scholarship, which has played a pivotal role in supporting my academic pursuits.

A shout-out to my colleagues in the Hydrogen Storage Laboratory, especially Ms. Sophida Thiangviriya, for their support, encouragement, and friendship.

To my friend Palm and Gartoon, as we celebrate our achievements, I want you to know how much your friendship means to me. I am proud of each and every one of you, and I am so fortunate to have you in my life.

And most importantly, my deepest appreciation goes to my family for their unconditional love, support, and encouragement throughout my life. Their sacrifices and belief in me have made this achievement possible.

Finally, I would like to show appreciation to all those who have contributed to this thesis in any way. Your support, encouragement, and friendship have been invaluable to me.

Phutthimet Thongtan

CONTENTS

CONTENTS (Continued)

LIST OF TABLES

Table **Page**

LIST OF FIGURES

LIST OF FIGURES (Continued)

LIST OF FIGURES (Continued)

LIST OF FIGURES (Continued)

LIST OF FIGURES (Continued)

Figure **Page**

CHAPTER I

INTRODUCTION

1.1 World energy consumption

The world is facing energy challenges, including climate change and air pollution. Fossil fuels, which are the world's primary source of energy, significantly contribute to these challenges. Burning fossil fuels releases greenhouse gases into the atmosphere, which trap heat and cause the earth's temperature to rise. This leads to a number of problems, including an increase of sea level, extreme weather events, and changes in plant and animal lifes. Besides, the energy demand increases every year, whereas the reserves of fossil fuels decrease steadily.

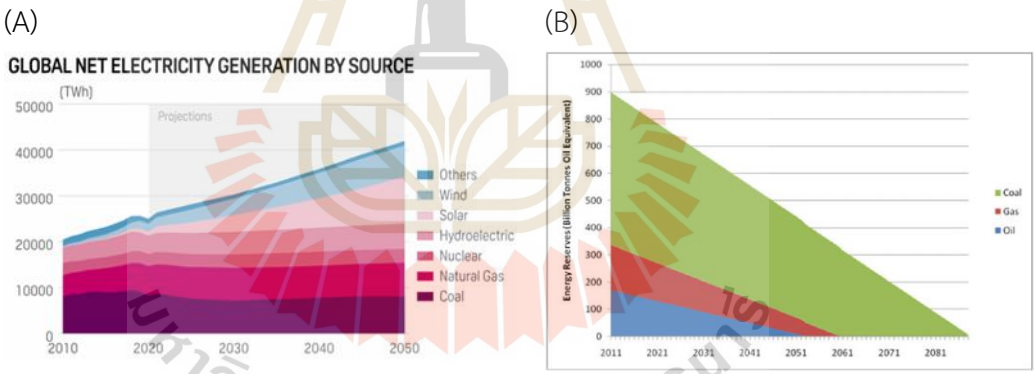

Figure 1.1 The projected global net electricity generation from 2010-2050 ("International Energy Outlook Introduction - Key Takeaways from the Reference and Side Cases - U.S. Enfergy Information Administration (EIA)," n.d.) (A) and the estimated reducing of energy sources from 2011-2081 (Zhao and Zhenghang, 2017) (B).

Therefore, renewable energy resources based on hydrogen energy, sun, wind, hydropower, and geothermal sources become significantly important as the world seeks to transition away from fossil fuels. Among these renewable energies, hydrogen energy is one of the promising solutions for these energy challenges and it is getting

more economically viable particularly for long-term and large-scale energy storage for a wide range of mobile/transportation and stationary applications (Assaf and Shabani, 2016; Gray et al., 2011; Kharel and Shabani, 2018; Maniatopoulos, Andrews, and Shabani, 2015; Shabani and Andrews, 2015; Shin, Hwang, and Choi, 2019). Hydrogen has high energy density (~142 MJ/kg), up to three times higher than conventional hydrocarbons fuel (e.g., diesel, gasoline, and LPG) (Andrews and Shabani, 2012b, 2012a, 2014).

1.2 Hydrogen storge technology

Hydrogen can be produced by various methods, such as steam reforming, electrolysis, photoelectrolysis and gasification. (Megia, Vizcaino, Calles, and Carrero, 2021) Hydrogen has ability to generate clean electricity through electrochemical reactions. Proton exchange membrane fuel cells (PEMFC) is an electrochemical device that converts the chemical energy stored in hydrogen and oxygen into electrical energy. The basic principle of PEMFC is based on the proton exchange reaction, where hydrogen molecules are oxidized into protons and electrons at the anode, and the protons transport across the proton exchange membrane to the cathode and combine with oxygen molecules to form water (Figure 1.2). These mechanisms result in the energy in the forms of electricity and heat.

To use hydrogen efficiently, hydrogen storage systems with high capacities and moderate operating temperature and pressure are required. Hydrogen can be stored by physical- and material-based materials (Figure 1.3). In the physical-based method, hydrogen is stored either as compressed gas (up to 700 bar H_2 at room temperature) or as liquefied hydrogen (at cryogenic temperatures of -253 °C), with storage capacities of 40 and 71 g H_2/L, respectively. Table 1.1 show the technical system for onboard Hydrogen targeted by U.S. Department Of Energy (DOE).

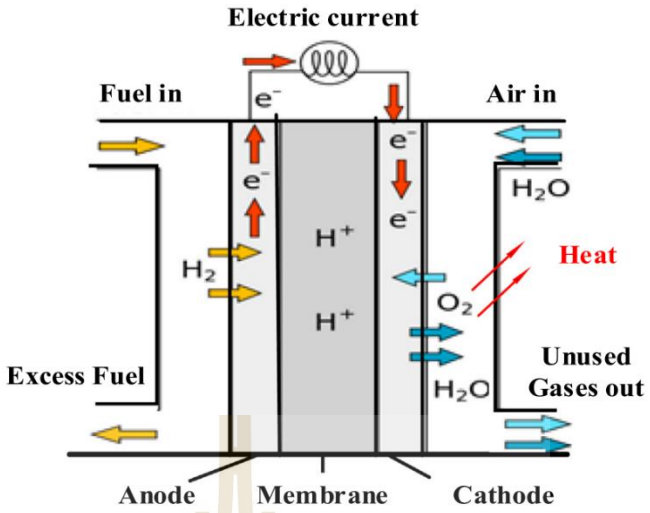

Figure 1.2 Schematic diagram of PEMFC (Bargal et al., 2020).

Currently, hydrogen can be stored in 3 mainly methods: compressed gas, liquefy hydrogen, and solid-state storage (Aceves, Martinez-Frias, and Garcia-Villazana, 2000; Irani, 2002; Walker, 2008). Although compressed hydrogen technique is the most widely used, it has considerable limitations due to the high storage pressure of compressed gas system, not only safety concerns rise but also cost for tank fabrication with demanding specifications, i.e. high tensile strength. Furthermore, the resulting volumetric energy density remains significantly lower than that of gasoline, offering a significant disadvantage in comparison (Shang, Pistidda, Gizer, Klassen, and Dornheim, 2021) Storage of hydrogen as a liquid requires cryogenic temperatures because the boiling point of hydrogen at one atmosphere pressure is –253 °C which consume ~10% of the total energy content of hydrogen and could reach ~20-30% in practical applications. Additionally, due to the natural tendency to evaporate of liquid hydrogen, storage tanks with highly insulating properties are required. Another one is material-based method, which are involve chemical absorption either in solid-state hydrides (metal, complex, and composite hydrides, e.g. MgH_2, $LiAlH_4$, $LiBH_4$, Mg_2NiH_4, and Mg_2FeH_6) or in liquid organic hydrogen carriers (e.g. toluene/methylcyclohexane). Additionally, physical adsorption through Van der Waals interaction in porous materials with high surface area is significant interest.

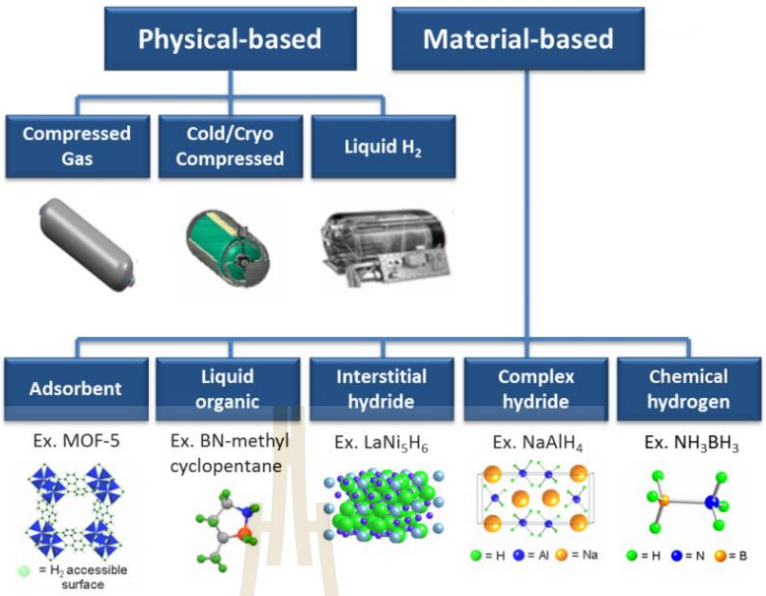

Figure 1.3 Hydrogen storage methods ("Hydrogen Storage | Department of Energy," n.d.).

Table 1.1 Technical system targets: onboard hydrogen storage for light-duty fuel cell vehicles by U.S.Department of Energy ("Hydrogen Storage | Department of Energy," n.d.).

Storage parameters	Units	2020	2025	ultimate
Gravimetric capacity				
Usable, specific-energy from H_2	kWh/kg (kg H_2/kg system)	1.5 (0.045)	1.8 (0.055)	2.2 (0.065)
Volumetric capacity				
Usable energy density from H_2	kWh/L (kg H_2/L system)	1.0 (0.030)	1.3 (0.040)	1.7 (0.050)

Table 1.2 Hydrogen storage characteristics of metal hydrides (Usman, 2022).

Metal hydride	Capacity (wt. % H_2)	Desorption temperature (°C)	Desorption enthalpy (kJ/mol H_2)
MgH_2	7.6	>300	75
Mg_2NiH_4	3.59	>280	65
Mg_2FeH_6	5.5	5.5	77.6
$FeTiH_2$	1.89	>30	300
$LaNi_5H_6$	1.4	>100	28
MgH_2-$LaAlH_4$	9.4	7.6	31
MgH_2-$NaAlH_4$	7.6	>175	45
MgH_2-$LiBH_4$	11.4	11.4	45

Metal hydrides can store hydrogen through a chemisorption process, in which hydrogen atoms are bonded to metal atoms. Once the metal hydride is formed, hydrogen is stored at ambient temperature and pressure. Hydride materials have high volumetric and gravimetric capacities up to 70-150 gH_2/L and 2-25 wt. % H_2, respectively. Not only their high storage capacities are attractive for hydrogen storage applications but also a wide range of operating temperatures and pressures, and high hydrogen purity. However, practical uses of metal hydrides are still limited due to high temperature and pressure requirement and particle agglomeration at high temperatures. Table 1.2 shows some examples of metal hydrides with H_2 capacities and operating temperatures.

Among several metal hydrides, magnesium hydride (MgH_2) is one of the most interesting due to its high gravimetric and volumetric storage capacities (7.6 wt. % and 110 kg H_2/m^3, respectively), abundance, long range operating condition, and cheap price. Nevertheless, kinetics of MgH_2 is obstructed by not only high operating pressure and temperature but also particle sintering and agglomeration at 400 °C (Hou, Yang, and Zhang, 2021). Kinetics of MgH_2 is expected to be improved by doping catalysts and additives.

This thesis aims to improve the kinetics properties of MgH_2 in terms of reducing dehydrogenation temperature and improving gas diffusion pathway in storage tank. Design and fabrication of the storage tanks and packing methods are also involved.

1.3 Concentrating solar power and thermal storage

Concentrating solar power (CSP) is one of the sustainable energies utilizing the heat collected from the sun to generate electricity. The research and development of the CSP system is attractive because of its advantages in terms of economic operating cost, good scale-up potential, and high efficiency (Goyal, Aggarwal, and Kumar, 2022). The heat from the sun can be collected by mirrors to the central location and stored in storage materials. The stored heat can be used to boil the water or generate electricity (Figure 1.4). To utilize the collected heat effectively, thermal storage materials with high thermal storage density for generating the electricity during sunless hours are required.

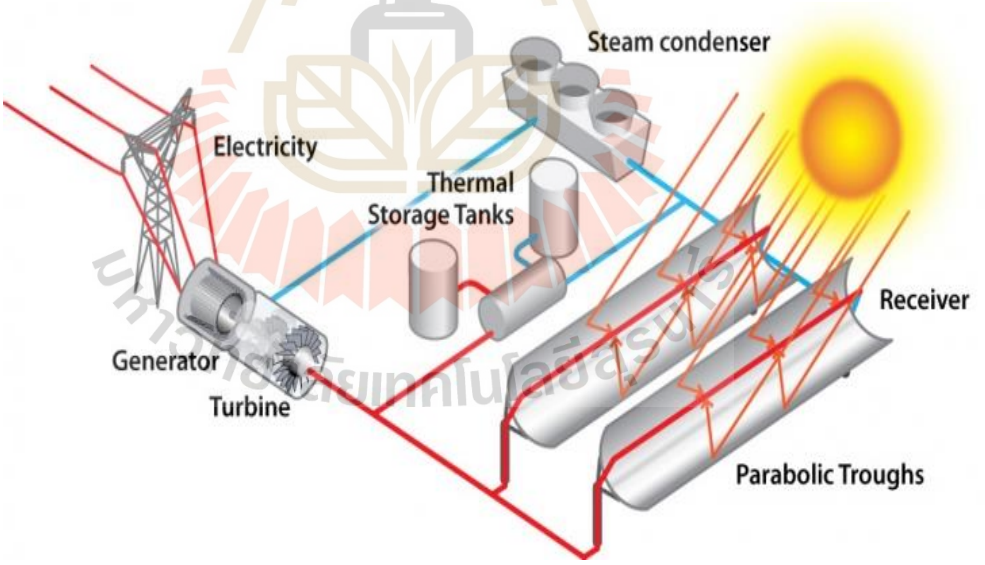

Figure 1.4 Schematic diagram of parabolic troughs power plant ("Linear Concentrator Solar Power Plant Illustration | Department of Energy," n.d.).

Thermal energy storage (TES) methods are typically categorized into 3 types. Firstly, sensible heat storage involves increasing the temperature of materials like water, rocks, and molten salts to store heat. Secondly, latent heat storage (LHS) relies on materials undergoing phase changes during melting or freezing, such as paraffin

wax, ice, and salt hydrates. Thirdly, thermochemical heat storage (THS) stores energy through reversible endothermic and exothermic reactions, utilizing substances like metal oxides, metal hydrides, and zeolites. The schematic of thermal storage methods is shown in Figure 1.5.

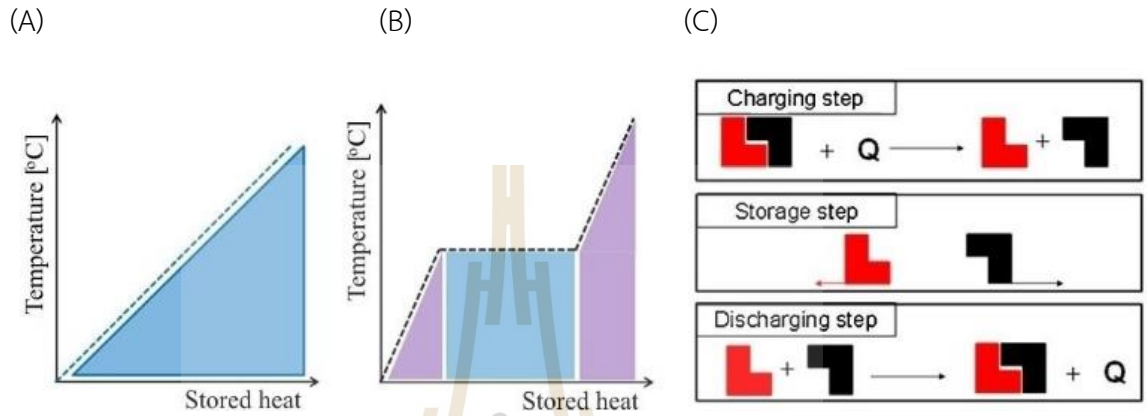

Figure 1.5 Thermal storage methods (A) Sensible heat storage, (B) Latent heat storage and (C) Thermochemical heat storage. Reprinted with permission from Pardo et al. Copyright 2014 Elsevier Ltd.

Among these technologies, THS is outstanding compared to SHS and LHS systems due to its high volumetric heat capacity of 500 kWh/m^3 which is higher than those of sensible and latent heat technology (50 and 100 kWh/m^3, respectively) (Aydin, Casey, and Riffat, 2015; Pardo et al., 2014). Metal hydride can be used as thermochemical storage materials which have the potential to apply for solar thermal energy storage due to its high energy density and wide working temperature range. Among many types of metal hydrides, MgH_2 is one of the most attractive materials for TES according to its high reaction enthalpy of 74.5 kJ/mol, leading to a large amount of heat released during the exothermic reaction (Li, Li, Shao, and He, 2018).

Table 1.3 Properties of heat storage materials (Pardo et al., 2014).

	Sensible heat storage system	Latent heat storage system	Thermochemical storage system
Volumetric density (kWh/m³)	50	100	500
Gravimetric density (kWh/kg)	0.02-0.03	0.05-0.1	0.5-1
Storage temperature (°C)	Charging step temperature	Charging step temperature	Ambient temperature
Storage period	Limited (thermal losses)	Limited (thermal losses)	Theoretically unlimited
Transport	Small distance	Small distance	Distance theoretically unlimited
Maturity	Industrial scale	Pilot scale	Laboratory scale
Technology	Simple	Medium	Complex

The purpose of this work is to develop a thermochemical storage system utilizing MgH_2 as thermal storage medium and the principle of coupling high-temperature metal hydrides (HTMH) and low-temperature metal hydrides (LTMH). The details of the technology will be discussed in the next chapter.

1.4 References

Aceves, S. M., Martinez-Frias, J., and Garcia-Villazana, O. (2000). Analytical and experimental evaluation of insulated pressure vessels for cryogenic hydrogen storage. *International Journal of Hydrogen Energy*, *25*(11), 1075–1085. https://doi.org/10.1016/S0360-3199(00)00016-1

Andrews, J., and Shabani, B. (2012a). Re-envisioning the role of hydrogen in a sustainable energy economy. *International Journal of Hydrogen Energy*, *37*(2), 1184–1203. https://doi.org/10.1016/j.ijhydene.2011.09.137

Andrews, J., and Shabani, B. (2012b). Where does hydrogen fit in a sustainable energy economy? *Procedia Engineering*, *49*, 15–25. Elsevier Ltd. https://doi.org/10.1016/j.proeng.2012.10.107

Andrews, J., and Shabani, B. (2014). The role of hydrogen in a global sustainable energy strategy. *Wiley Interdisciplinary Reviews: Energy and Environment*, Vol. 3, pp. 474–489. John Wiley and Sons Ltd. https://doi.org/10.1002/wene.103

Assaf, J., and Shabani, B. (2016). Economic analysis and assessment of a standalone solar-hydrogen combined heat and power system integrated with solar-thermal collectors. *International Journal of Hydrogen Energy*, *41*(41), 18389–18404. https://doi.org/10.1016/j.ijhydene.2016.08.117

Aydin, D., Casey, S. P., and Riffat, S. (2015). The latest advancements on thermochemical heat storage systems. *Renewable and Sustainable Energy Reviews*, Vol. 41, pp. 356–367. Elsevier Ltd. https://doi.org/10.1016/j.rser.2014.08.054

Bargal, M. H. S., Abdelkareem, M. A. A., Tao, Q., Li, J., Shi, J., and Wang, Y. (2020). Liquid cooling techniques in proton exchange membrane fuel cell stacks: A detailed survey. *Alexandria Engineering Journal*, *59*(2), 635–655. https://doi.org/10.1016/J.AEJ.2020.02.005

Goyal, N., Aggarwal, A., and Kumar, A. (2022). Concentrated solar power plants: A critical review of regional dynamics and operational parameters. *Energy Research and Social Science*, *83*(October 2021), 102331. https://doi.org/10.1016/j.erss.2021.102331

Gray, E. M., Webb, C. J., Andrews, J., Shabani, B., Tsai, P. J., and Chan, S. L. I. (2011). Hydrogen storage for off-grid power supply. *International Journal of Hydrogen Energy*, *36*(1), 654–663. https://doi.org/10.1016/j.ijhydene.2010.09.051

Hou, Q., Yang, X., and Zhang, J. (2021, February 17). Review on Hydrogen Storage Performance of MgH_2: Development and Trends. *ChemistrySelect*, Vol. 6, pp. 1589–1606. Wiley-Blackwell. https://doi.org/10.1002/slct.202004476

Hydrogen Storage | Department of Energy. (n.d.). Retrieved January 24, 2024, from https://www.energy.gov/eere/fuelcells/hydrogen-storage

International Energy Outlook Introduction - Key takeaways from the Reference and side cases - U.S. Energy Information Administration (EIA). (n.d.). Retrieved October 21, 2023, from https://www.eia.gov/outlooks/ieo/introduction/sub-topic-01.php

Irani, R. S. (2002). Hydrogen storage: High-pressure gas containment. *MRS Bulletin*, *27*(9), 680–682. https://doi.org/10.1557/MRS2002.221/METRICS

Kharel, S., and Shabani, B. (2018). Hydrogen as a long-term large-scale energy storage solution to support renewables. *Energies*, *11*(10). https://doi.org/10.3390/en11102825

Li, B., Li, J., Shao, H., and He, L. (2018, August 15). Mg-based hydrogen absorbing materials for thermal energy storage-A review. *Applied Sciences (Switzerland)*, Vol. 8. MDPI AG. https://doi.org/10.3390/app8081375

Linear Concentrator Solar Power Plant Illustration | Department of Energy. (n.d.). Retrieved October 21, 2023, from https://www.energy.gov/eere/solar/articles/linear-concentrator-solar-power-plant-illustration

Maniatopoulos, P., Andrews, J., and Shabani, B. (2015, August 11). Towards a sustainable strategy for road transportation in Australia: The potential contribution of hydrogen. *Renewable and Sustainable Energy Reviews*, Vol. 52, pp. 24–34. Elsevier Ltd. https://doi.org/10.1016/j.rser.2015.07.088

Megia, P. J., Vizcaino, A. J., Calles, J. A., and Carrero, A. (2021). Hydrogen Production Technologies: From Fossil Fuels toward Renewable Sources. A Mini Review. *Energy and Fuels*, *35*(20), 16403–16415. https://doi.org/https://doi.org/10.1021/acs.energyfuels.1c02501

Pardo, P., Deydier, A., Anxionnaz-Minvielle, Z., Rougé, S., Cabassud, M., and Cognet, P. (2014, April). A review on high temperature thermochemical heat energy storage. *Renewable and Sustainable Energy Reviews*, Vol. 32, pp. 591–610. https://doi.org/10.1016/j.rser.2013.12.014

Shabani, B., and Andrews, J. (2015). Standalone solar-hydrogen systems powering Fire Contingency Networks. *International Journal of Hydrogen Energy*, *40*(15), 5509–5517. https://doi.org/10.1016/j.ijhydene.2015.01.183

Shang, Y., Pistidda, C., Gizer, G., Klassen, T., and Dornheim, M. (2021, November 15). Mg-based materials for hydrogen storage. *Journal of Magnesium and Alloys*, Vol. 9, pp. 1837–1860. National Engg. Reaserch Center for Magnesium Alloys. https://doi.org/10.1016/j.jma.2021.06.007

Shin, J., Hwang, W. S., and Choi, H. (2019). Can hydrogen fuel vehicles be a sustainable alternative on vehicle market?: Comparison of electric and hydrogen fuel cell vehicles. *Technological Forecasting and Social Change*, *143*, 239–248. https://doi.org/10.1016/j.techfore.2019.02.001

Usman, M. R. (2022, October 1). Hydrogen storage methods: Review and current status. *Renewable and Sustainable Energy Reviews*, Vol. 167. Elsevier Ltd. https://doi.org/10.1016/j.rser.2022.112743

Walker, G. (2008). Hydrogen storage technologies. *Solid-State Hydrogen Storage: Materials and Chemistry*, 3–17. https://doi.org/10.1533/9781845694944.1.3

Zhao, and Zhenghang. (2017). DESIGN PRINCIPLE ON CARBON NANOMATERIALS ELECTROCATALYSTS FOR ENERGY STORAGE AND CONVERSION. https://doi.org/10.13140/RG.2.2.25704.16641

CHAPTER II

LITERATURE REVIEWS

2.1 Hydrogen storage in metal hydrides

Chemisorption processes in solid-state form, metal hydrides gain attention for its high storage capacity, impressive stability, and small space occupancy (Lee et al., 2022; Nguyen and Shabani, 2021). Metal hydrides store and release hydrogen by reversible interaction between hydrogen and metal. Initially, Hydrogen molecule interacts with the metallic host by Vander Waals' forces (physisorption), following by the dissociation to hydrogen atoms and diffusion to the metal's interstitial sites to form a solid solution (chemisorption). This phase transformation results in the change of crystal structure and/or lattice parameters (Figure 2.1) (Gupta et al., 2021).

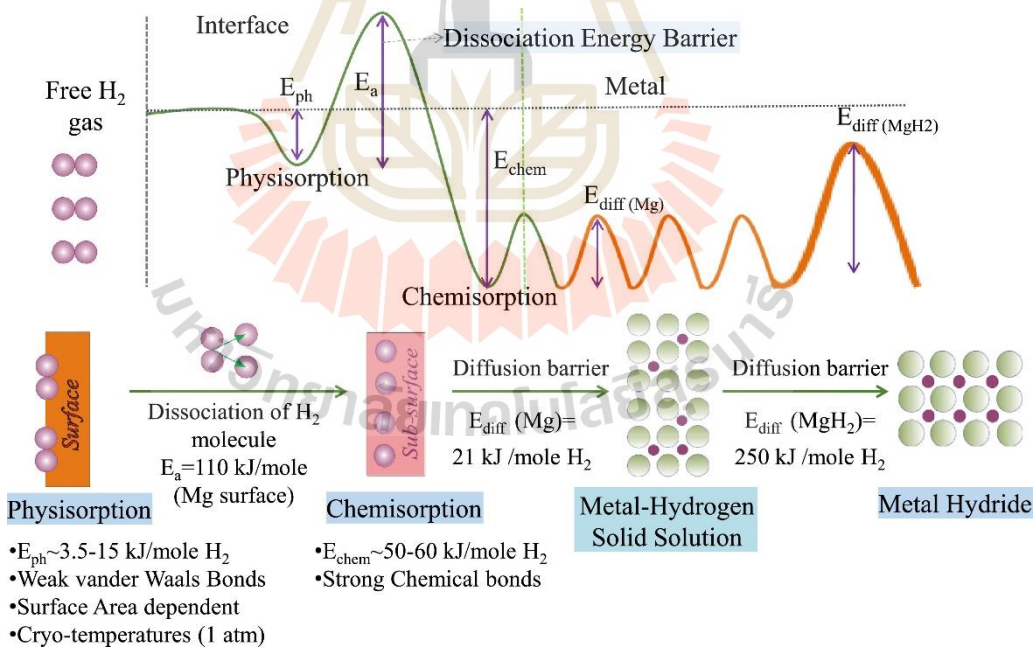

Figure 2.1 Interaction of hydrogen with material in various steps: (i) physisorption, (ii) chemisorption, (iii) solid solution and (iv) compound formation (Gupta et al., 2021).

Van't Hoff plots (Figure 2.2(B)) shows the relationship between equilibrium pressure (P_{eq}) and the hydrogen storage capacity at various temperatures of hydride nucleation and growth. The **α**-phase corresponds to low-pressure metal hydride formation, followed by the plateau region representing equilibrium between **α** and β phases. The β-phase region indicates the stability of metal hydride nucleation and growth (Schlapbach and Züttel, 2001). P_{eq} as a function of temperature is related to the changes of enthalpy (ΔH) and entropy (ΔS) as explained by the following equation.

$$\ln\left(\frac{P_{eq}}{P_0}\right) = \frac{\Delta H}{RT} - \frac{\Delta S}{R} \tag{2.1}$$

where P_{eq} is the plateau pressure, T is the temperature (K), P_0 is the reference pressure (1 bar), R is the gas constant (R = 8.314 J/mol·K), ΔH and ΔS are the enthalpy and entropy changes during the **α** to β transformation, respectively (Klopčič, Grimmer, Winkler, Sartory, and Trattner, 2023; Züttel, 2003).

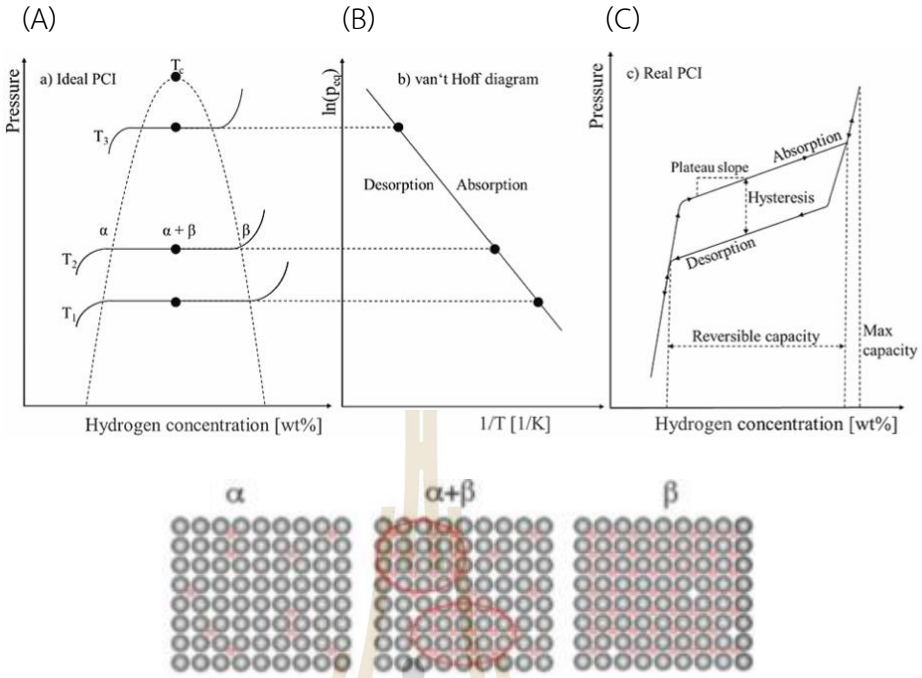

Figure 2.2 Ideal pressure composition isotherm (PCI) at different temperatures (A) with the corresponding van't Hoff plot (B) and PCI with hysteresis and plateau slope (C) together with hydride nucleation and growth (Dornheim, 2011; Klopčič et al., 2023).

The absorption requires hydrogen pressure to exceed the P_{eq} pressure at specific temperature. During desorption, the hydrogen pressure falls below the equilibrium pressure (Figure 2.2(B)). As the temperature rises, the equilibrium pressure also increases. Hydride materials undergo an exothermic absorption reaction and the released heat elevates the temperature. Without proper thermal management, this process is hindered, causing prolonged absorption time. For effective desorption, sufficient heat is required to maintain the desired hydrogen dissociation pressure. Practically, the PCI diagram typically exhibits a sloping plateau and hysteresis due to the kinetics different between the absorption and desorption processes (Figure 2.2(C)) (Klopčič et al., 2023).

2.2 MgH_2-based hydrogen storages and their tuning strategies

Among many hydrides, MgH_2 has been intensively investigated for hydrogen storage applications owing to its remarkable volumetric and gravimetric hydrogen capacities of 110 kg H/m^3 and 7.6 wt. % H_2, respectively. These capacities are greater than those of conventional compressed hydrogen technology (23 kg H/m^3 at 350 bar and 38 kg H/m^3 at 700 bar) and liquid hydrogen (71 kg H/m^3) (Sheffield, Martin, and Folkson, 2014; Zaluska, Zaluski, and Strom-Olsen´centre, 1999). Although MgH_2 owns high hydrogen capacities, its high decomposition temperature up to ~400 °C, poor hydrogen absorption/desorption kinetics due to high thermal stability (ΔH = 76 kJ/mol) result in high activation energy (E_a) of ~160 kJ/mol for the dehydrogenation and obstruct practical applications (Dornheim et al., 2007; Lee et al., 2022; Ley et al., 2014; Thaweelap et al., 2017). MgH_2 stores and releases hydrogen reversibly as shown in equation (2.2).

$$MgH_{2\,(s)} \leftrightarrow Mg_{(s)} + H_{2\,(g)} \tag{2.2}$$

MgH_2 has mixed ionic-covalent type of chemical bond with a rutile-type crystal structure (space group #136; a=4.517A, c=3.020 A) (Zhang et al., 2017). The conversion of hexagonal Mg into tetragonal MgH_2 (bulk density of 1.45 g/cm^3) results in 20% expansion in volume. Several studies to improve the properties of MgH_2 have been proposed, such as alloy formations (Hardian et al., 2018; Hitam, Aziz, Ruhaimi, and Taib, 2021; Ouyang et al., 2020), nanostructures (Sterl et al., 2018; Yu, Bennici, and Auroux, 2014), (Nielsen, Manickam, Hirscher, Besenbacher, and Jensen, 2009; Zlotea et al., 2015)), and doping with catalysts and/or additives. For practical applications, up scaling to tank scale have been intensively investigated.

2.2.1 Alloy formations

MgH_2 can be alloyed with other elements to form binary, ternary, or multinary hydrides, resulting in the decrease of MgH_2 stability. A study on hydrogen storage using binary Mg_2Ni nanoparticles (20-50 nm) showed that the compacted $2MgH_2$-Ni demonstrated a lower dehydrogenation temperature at 290 °C. The PCI results showed the single-step dehydrogenation and exhibited low absorption and desorption enthalpies of 57.5 and 61.3 kJ mol^{-1} H_2, respectively. Moreover, Mg_2Ni demonstrated fast H_2 absorption kinetics ~3.4 wt. % H_2 at 375 °C in less than 5 min (Khan, Zou, Zeng, and Ding, 2018). Mg_2FeH_6 has been highly observed for hydrogen storage due to its high volumetric and gravimetric hydrogen density of 150 kg H_2/m^3 and 5.43 wt. % H_2. However, the practical utilization is hindered by sluggish kinetics according to long distance for hydrogen diffusion (Herrich et al., 2004). $Mg_2Fe(Ni)H_6$ nanowires were synthesized using coarse-grained Mg and nano-sized Fe(Ni) precursors. The γ-Fe with the same fcc lattice structure Mg_2FeH_6 contributed to reducing the diffusion distance of Fe during the Mg_2FeH_6 formation. Dehydrogenation temperature of $Mg_2Fe(Ni)H_6$ reduced for 21.6 °C as compared to pure Mg_2FeH_6 as well as the decrease in sorption enthalpy from 89 to 69 kJ/mol H_2 (Xi Chen, Zou, Zeng, and Ding, 2016).

2.2.2 Nanostructure

2.2.2.1 Mechanical ball milling

Mechanical ball milling is highly effective method for processing powders and extensively used in material fabrication and chemical processes. For metal hydrides, ball milling generates new surfaces, enhances area, develops micro/nanostructures, and creates defects. These facilitate hydrogen dissociation and accelerate its diffusion. Rahmaninasab et al. explored the impact of different ball milling times (10, 30, and 40 h) on MgH_2 nanostructure. After 40 h, the crystallite size reduced from 87 to 32 nm. Onset desorption temperature of 40-h milled MgH_2 decreased by 80 °C lower than that of as-received MgH_2 (Figure 2.3) (Rahmaninasab, Raygan, Abdizadeh, Pourabdoli, and Mirghaderi, 2018)

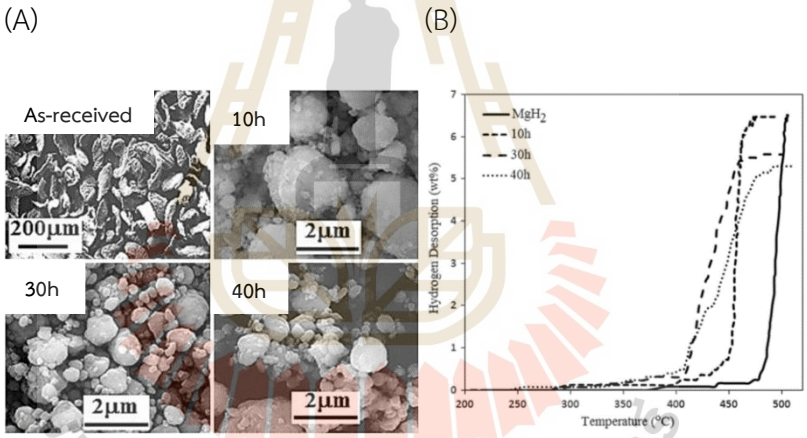

Figure 2.3 SEM images of as-received MgH_2 and as-milled MgH_2 for 10, 30, and 40 h (A) and Hydrogen desorption behavior of as-received MgH_2 and as-milled MgH_2 (B) (Rahmaninasab et al., 2018).

Huot et al. investigated the effect of ball milling on the structures and sorption kinetics of MgH_2. Hydrogen sorption kinetics of MgH_2 obviously improved after milling for 20. Ball-milled MgH_2 exhibited complete absorption at 300 °C and desorption at 350 °C within 1 min, 5 times faster kinetics than as-received MgH_2 (Figure 2.4). This enhancement is attributed to the defects formed during ball milling. The latter reduced particle size and increased specific surface area, promoting faster nucleation and shorter diffusion lengths (Huot, Liang, Boily, Van Neste, and Schulz, 1999). Varin et al. explored the impacts of particle size, grain size, and the γ-MgH_2 phase on desorption characteristics of nanocrystalline MgH_2. Dehydrogenation peak temperatures gradually decreased with reduced the particle size and the presence of γ-MgH_2 acting as a catalyst. Besides, desorption temperatures reduced by 30–60 °C after 10 h or more milling (Varin, Czujko, Chiu, and Wronski, 2006).

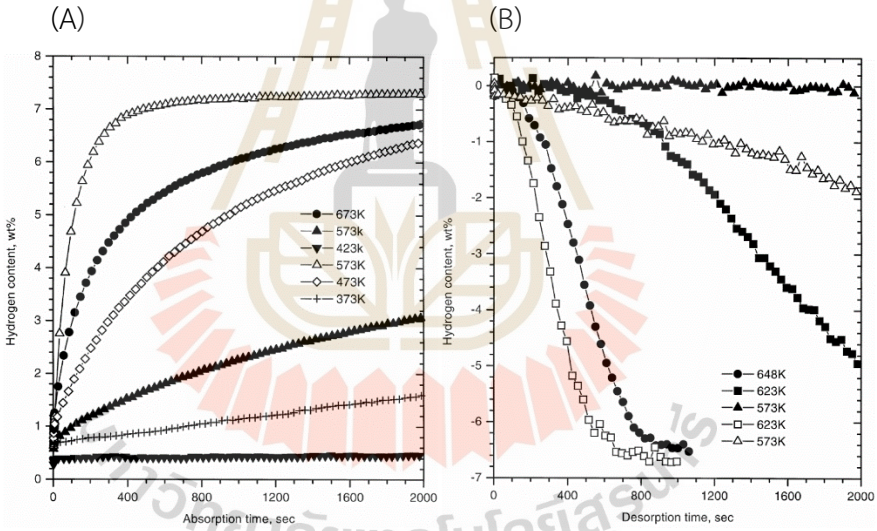

Figure 2.4 Hydrogen absorption under 1.0 MPa H_2 (A) and desorption under 0.0152 MPa H_2 (B) of as-received (hollow marks) MgH_2 and ball-milled (filled marks) MgH_2 (Huot et al., 1999).

2.2.2.2 Nanoconfinement

Nanoconfinement of MgH_2 into porous materials has been developed to prevent particle growth as well as to enhance dispersion and active surface. Nielsen et al. investigated the kinetics of de/hydrogenation of confined MgH_2 in nanoporous carbon aerogel scaffold materials. Two samples of nanoporous carbon aerogel with the pore volumes of 1.27 and 0.65 mL/g and average pore sizes of 22 and 7 nm were employed as the hosts for MgH_2. ~12 vol. % of MgH_2 were confined in nanoporous carbon aerogel allowed ~81% of reversible hydrogen sorption from loaded MgH_2. The hydrogen absorption of nanoconfined deepened on the pore volume. And pore size distribution of the scaffold material. Smaller pores exhibited faster desorption rates, possibly attributed to the size reduction of the confined MgH_2 (Nielsen et al., 2009). Zlotea et al. embedded MgH_2 nanoparticles in microporous carbon by adjusting the Mg content. With 15 and 25 wt. % Mg contents, ultrasmall particles with mean the sizes of 1.3 and 3.0 nm were obtained. Dehydrogenation properties were found to strongly depend on nanoparticle size. The onset temperature dehydrogenation for MgH_2 nanoparticles below 3 nm was 245 °C lower than that of crystalline MgH_2. ^1H NMR data revealed the presence of two distinct MgH_2 populations exhibiting elevated hydrogen mobility. The enhanced kinetics could be explained by the shortened hydrogen diffusion path and the increased hydrogen mobility (Zlotea et al., 2015).

2.2.3 Doping with catalysts and additives

2.2.3.1 Transition metal based catalyst

The sluggish kinetics of Mg/MgH_2 hydrogen sorption is due to slow H_2 dissociation at the metal surface, limited hydrogen penetration due to the oxide layer, and slow diffusion of dissociated H atoms in the metal (Kondo Franois Aguey-Zinsou and Ares-Fernández, 2010; Nishimura, Komaki, and Amano, 1999; S. Zhou et al., 2014). Catalyst doping is a practical method to enhance MgH_2 de/hydrogenation kinetics by providing more active areas for hydrogen sorption, thus accelerating the reaction. Several transition metals (Fe, Co, Ni, Cu Sc, Ti, V, Cr, Y, Zr, Nb, Mo, and Mn (El Khatabi et al., 2016; G. Liang, J. Huot, S. Boily, A. Van Neste, and R. Schulz, 1999; Hanada, Ichikawa, and Fujii, 2005; Lu et al., 2021; Si, Zhang, Feng, Ding, and Li, 2021)) as well as

transition metal oxides (TiO_2, V_2O_5, $VNbO_5$, Co_3O_4, $NiCo_2O_4$, NiO, and Nb_2O_5 (Cabo et al., 2011; Korablov, Nielsen, Besenbacher, and Jensen, 2015; Z. Ma et al., 2020; Nielsen and Jensen, 2012; Valentoni, Mulas, Enzo, and Garroni, 2018)), halides (VCl_3, $ScCl_3$, NbF_5, and TiF_3 (Korablov et al., 2015), (L. P. Ma et al., 2009a; Plerdsranoy et al., 2019; P. Wang et al., 2021; Xie, Liu, Wang, Zheng, and Li, 2007)), hydrides (YiH_2 and ZrH_2 (Korablov et al., 2015)), and sulfides (NbS_2, MoS_2, MnS, CoS_2, CuS, and TiS_2 (P. Wang et al., 2021)) have been added to improve the kinetics of MgH_2. Cui et al. applied various nanoscale transition metals (Ti, Nb, V, Co, Mo, Ni) on Mg surface to create a core-shell structure. Experimental revealed that Ti exhibited the most effective dehydrogenation performance as shown in TPD profiles (Figure 2.5). The dehydrogenation performance diminished in sequence with decreasing electronegativity of the transition metals (Cui et al., 2014).

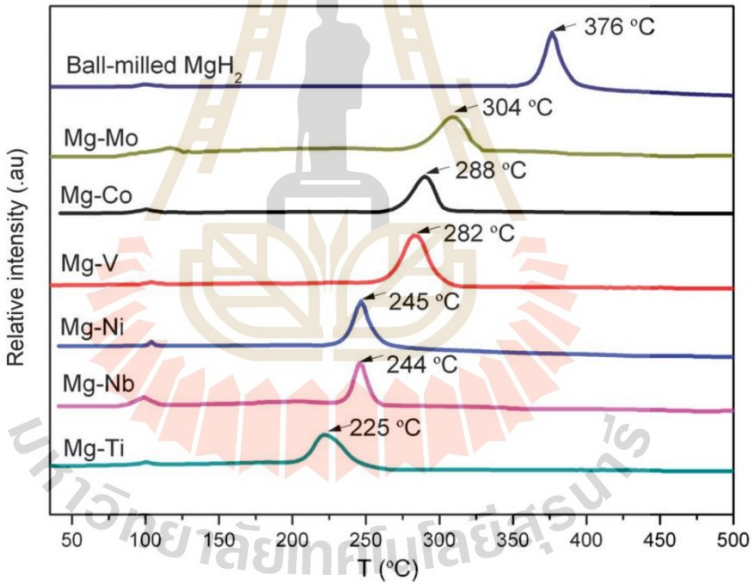

Figure 2.5 Temperature programmed desorption (TPD)-mass spectrometry (MS) curves of Mg doped with transition metal-based catalysts. Reprinted with permission from Cui et al., 2014. Copyright 2014 Royal Society of Chemistry.

Pukazhselvan et al. demonstrated the formation of TiH_{2-x} in MgH_2/Ti nanocomposites through ball milling. During de/rehydrogenation, TiH_{2-x} transformed into TiH_2, leading to the reduced activation energy of MgH_2 to 89.4 kJ/mol (Pukazhselvan, Sandhya, Ramasamy, Shaula, and Fagg, 2020). Wang et al. found that TiH_2 and $TiH_{1.971}$ occur in MgH_2-Ti composite under high energy ball milling. Onset dehydrogenation temperature

of the composite decreased by ~51 °C as compared to pure MgH_2. Further examination indicated the active role of TiH_2 and $TiH_{1.971}$ as catalysts for MgH_2 (Y. Wang, Wang, Zhang, Jiao, and Yuan, 2015; C. Zhou, Zhang, Bowman, and Fang, 2021). The presence of multiple valence Ti acted as an intermediate and catalytic active site, facilitating electron transfers between Mg^{2+} and H during the de/hydrogenation and leading to significantly improved kinetic performance (Figure 2.6).

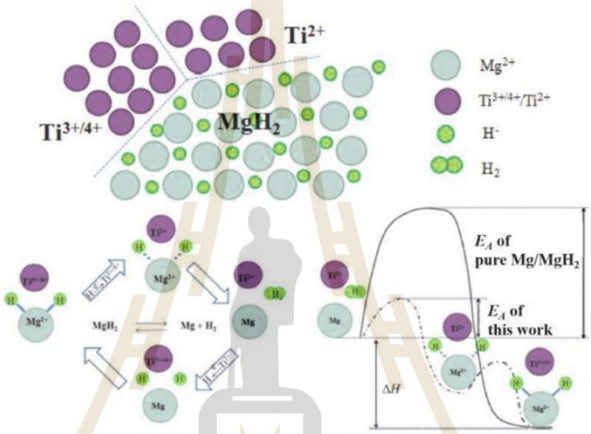

Figure 2.6 Schematic diagram of the catalytic mechanism in de/hydrogenation of MgH_2-multi-valences Ti. Reprinted with permission from Cui et al., 2013. Copyright 2013 Royal Society of Chemistry.

Tong et al. prepared Mg doped with 7.5 wt. % Nb nanocomposites by hydrogen plasma-metal reaction (HPMR) method. At 200 °C, the nanocomposite absorbed 4.0 wt. % H_2 in 10 min and achieved 5.6 wt. % H_2 in 60 min. Furthermore, at 300 °C, it released 4.0 wt. % H_2 within the same timeframe. The study observed the conversion of Nb to NbH, hindering Mg growth and enhancing the diffusion of H atoms. This resulted in the reduction of activation energy for hydrogenation and dehydrogenation to 70.9 and 86.4 kJ/mol, respectively. The authors also mentioned that the decrease in the electronegativity of metal elements led to an increased affinity between metal elements and hydrogen, resulting in the weaker Nb-H bond. The mechanism of Nb catalytic effect is illustrated in Figure 2.7 (Liu, Ma, Chen, Xu, and Li, 2015).

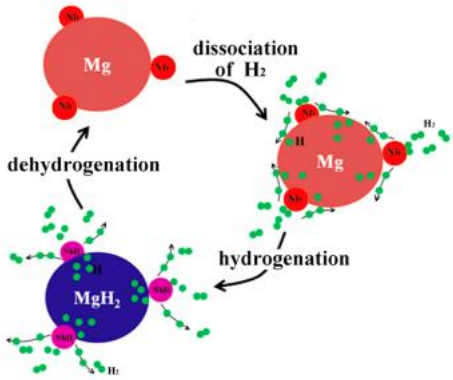

Figure 2.7 Schematic diagram of the catalytic mechanism of Nb nanoparticles during the hydrogenation/dehydrogenation of the Mg–Nb composite (Liu et al., 2015).

Oelerich et al. used ball milling to synthesize nanocrystalline Mg-based materials doping with metal oxides (TiO, V_2O_5, Cr_2O_3, MnO, Fe_2O_3, CuO). The results showed faster absorption and desorption kinetics as compared to pure materials. Cr_2O_3 exhibited superior hydrogen absorption, reaching 4.7 wt. % within 2 min at 300 °C, whereas V_2O_5 and Fe_3O_4 demonstrated rapid hydrogen desorption. The enhanced performance was attributed to the high defect density in the metal oxide particles achieved through high energy ball milling (Oelerich, Klassen, and Bormann, 2001). Barkhordarian et al. studied the de/hydrogenation kinetics of MgH_2 catalyzed by several metal oxides. Results revealed that Nb_2O_5 was the superior catalyst for the hydrogen sorption reaction of Mg. The catalytic effect of Nb_2O_5 was attributed to electronic exchange with H_2 molecules and the multiple valence states of Nb metal, accelerating the gas-solid reaction (Barkhordarian, Klassen, and Bormann, 2003, 2004). In addition, large content of Nb_2O_5 (17 wt. %) was added to MgH_2. The enhanced kinetics performance was explained by the properties of Nb_2O_5, acting as the lubricant, dispersant, and cracking agent during mechanical ball milling process (K. F. Aguey-Zinsou, Ares Fernandez, Klassen, and Bormann, 2007). Interestingly, the structure of catalysts can affect the catalytic properties. Kumar et al. found that the mesoporous Nb_2O_5 with a larger specific surface area than crystalline Nb_2O_5 showed very fast kinetics during the dehydrogenation process. MgH_2 doped with mesoporous Nb_2O_5 required less than 200 °C for dehydrogenation (Figure 2.8(A)) and was able to absorb H_2 up to 5.9 wt. % in 1 min at 1.8 MPa and room temperature while MgH_2

doped with crystalline Nb_2O_5 absorbed 3.5 wt. % H_2 in 5 min (Figure 2.8(B)) (Kumar, Kojima, and Dey, 2017).

(A) (B)

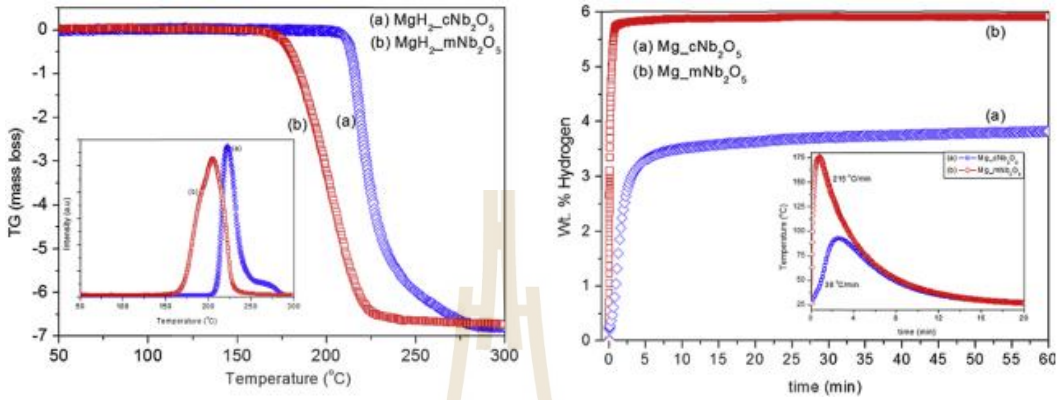

Figure 2.8 Thermogravimetric (TG)-mass spectrometry (MS) analysis (A) and hydrogenation at room temperature (B) of MgH_2-cNb_2O_5 (a) and Mg-mNb_2O_5 (b). Reprinted with permission from Kumar et al., 2017. Copyright 2017 Hydrogen Energy Publications LLC. Published by Elsevier Ltd.

Metal halides, specifically Cl- and F-containing phases have been explored as catalysts for the Mg/MgH_2 system. Ma et al. conducted a comparative study on the catalytic impact of TiF_3 and $TiCl_3$ on MgH_2 through mechanical milling. Results suggested that TiF_3 exhibits better catalytic effects than $TiCl_3$. TiX_3 (X = halide) reacted with MgH_2, resulting in the formation of TiH_2 and MgX_2. X-ray photoelectron spectroscopy (XPS) analysis revealed the formation of a metastable active Ti–F–Mg phase in the TiF_3-doped system (L. P. Ma et al., 2009b). Jin et al. observed the hydrogen sorption of MgH_2 catalyzed with transition metal halides. Faster hydrogenation and lower dehydrogenation temperature were obtained after adding transition metal fluorides. They also mentioned that transition metal fluorides were capable to react with MgH_2 to generate hydrides or solid solutions of metal-hydrogen and the enhanced performances of hydrogen sorption due to the reaction between MgH2 and transition metal halides (TiH_2, V_3H_2, NbH) (Jin, Shim, Cho, and Yi, 2007).

2.2.3.2 Carbon additives

At 400 °C, sintering of MgH_2 during cycling can leads to agglomeration and sluggish hydrogen sorption kinetics. To address this issue, various carbon materials, such as activated carbon (AC), expanded natural graphite (ENG), multi-walled carbon nanotubes (MWCNTs), and carbon nanofibers (CNFs), have been added into MgH_2. This not only prevents agglomeration but also improves hydrogen diffusion, thermal conductivity, and provides sample loading sites for MgH_2 and catalyst. (Adelhelm and De Jongh, 2011; Awad et al., 2016; Chaise et al., 2009; Fuster, Castro, Troiani, and Urretavizcaya, 2011; Jia, Guo, Zou, and Yao, 2012; Lillo-Ródenas, Guo, Aguey-Zinsou, Cazorla-Amorós, and Linares-Solano, 2008). Activated carbon, with adjustable pore sizes present unique advantages. They are cost-effective, commercially viable, and allow for mass production (Bastos-Neto et al., 2012; Im, Park, Kim, Kim, and Lee, 2008; Im, Park, and Lee, 2009; Sevilla and Mokaya, 2014). Several reports show the positive effects of AC on hydrogen sorption of Mg including the enhanced hydrogen absorption rate and capacity together with the maintained de/rehydrogenation performance upon cycling (Grigorova, Khristov, Stoycheva, and Tsyntsarski, 2017; Grigorova et al., 2011), (Chaise et al., 2009; Rud and Lakhnik, 2012; Rud et al., 2008). Introduction of MWCNTs leads to the lower dehydrogenation temperature and the activation energy for the dehydrogenation process. The unique structure of MWCNTs plays a positive role by reducing the particle agglomeration (Ismail, Juahir, and Mustafa, 2014). For graphite, its high thermal conductivity benefits the heat transfer inside the storage tank, leading to the enhanced sorption kinetics. Moreover, it also prevents the formation of an oxide layer and the agglomeration of powder (Huot, Tremblay, and Schulz, 2003; Shang and Guo, 2004).

2.2.4 Upscaling to hydrogen storage tank

Besides the experiments in laboratory scale, we aim to design and fabricate hydrogen storage tank with the heat exchanger. Among several designs of heat exchangers for hydride-based tanks, such as inner spiral finned tube combined with concentric triple-tube heat exchanger ($LaNi_5$-based tanks) (Chibani and Bougriou, 2017; Kaplan, 2009; Souahlia et al., 2014), metallic honeycomb structure with hexagonal cells

($NaAlH_4$-based tank) (Bhouri, Goyette, Hardy, and Anton, 2011), copper fins combined with central cooling tube and helical coil (MgH_2-based tanks) (Chaise et al., 2009; Garrier et al., 2011; Wu, Yang, Zhang, and Bao, 2014), central tube heat exchanger is the most practical when convenience and efficiency during hydride packing are considered. Compacted pellets of MgH_2 with 5 wt. % ENG placed in a storage tank equipped with the heat exchanger (copper fins and a forced air tube) (Figure 2.9) exhibited the improved absorption kinetics up to 5.8 wt. % H_2 at 300 °C under 10 bar H_2 in 25 min. (Chaise et al., 2009). Garrier et al. studied hydrogen sorption behavior of MgH_2 in intermediate tank scale with copper the fins and central cooling tube (Figure 2.10). The tank allows absorption at low pressure (0.6 MPa) and onset temperature of 90 °C with complete hydrogenation (6 wt. % H_2). Dehydrogenation occurred with an outlet hydrogen pressure range of 0.3 to 0.1 MPa. Placing internal heating elements in contact with powder beds showed more efficient than an external heating system. This led to the maximum outlet hydrogen flow directly correlated with heating system power. The gravimetric capacity of 0.8 wt. % H_2 corresponding to a specific energy of ~270 Wh/kg resulted in a system energy density of 42 g/L (1.44 kWh/L) (Garrier et al., 2011).

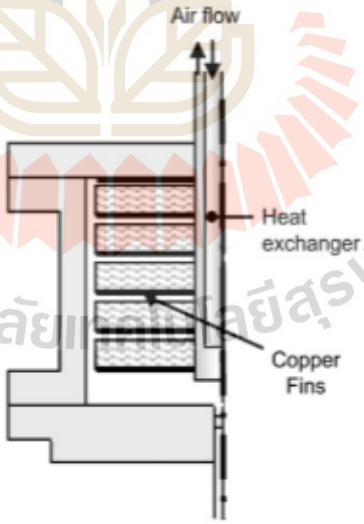

Figure 2.9 Schematic diagram of compacted disks in the tank with a heat exchanger (copper fins air tube). Reprinted with permission from Chaise et al., 2009. Copyright 2009 Professor T. Nejat Veziroglu. Published by Elsevier Ltd.

(A) (B)

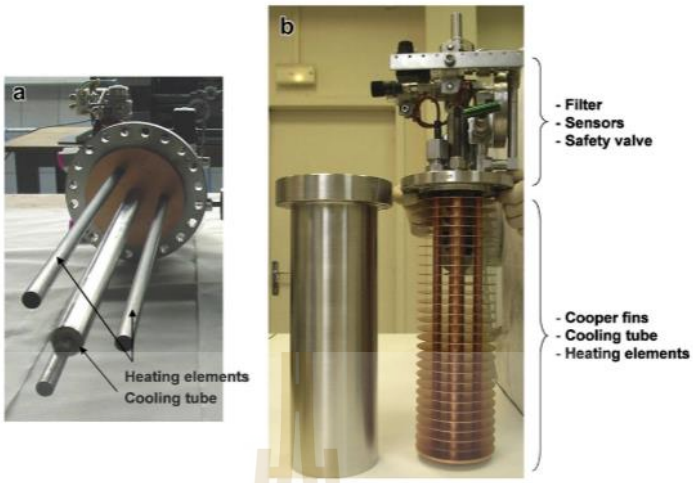

Figure 2.10 Electrical heating elements and central cooling tube (A) and external stainless-steel container and stack of copper fins connected to the vessel cap (B). Reprinted with permission from Garrier et al., 2011. Copyright 2011 Hydrogen Energy Publications, LLC. Published by Elsevier Ltd.

In this thesis, we focus on the development of the kinetic and thermodynamic properties of MgH_2 by adding catalysts and carbon materials as well as the packing methods, designs, and fabrication of hydrogen storage tank.

2.3 Thermal energy storage

Solar energy is abundant and can be converted into electricity through concentrated solar plants (CSP), which consist of concentrators, receivers, transport systems, and power conversion machines. However, a significant challenge is the heat storage materials for solar energy. To address this, thermal energy storage (TES) systems are being developed. These systems store heat during the sun periods and release it when solar irradiation is weak or absent. Integrating TES with CSP ensures a continuous electricity supply. High efficient TES systems advance solar technology and enable electricity production from thermal energy day and night without emitting greenhouse gases. Among the heat storage technologies, thermochemical heat storage (THS) is one of the best TES materials due to the high volumetric heat capacity of 500 kWh/m^3, greater than those of sensible and latent heat systems (50 and 100 kWh/m^3, respectively) (Aydin, Casey, and Riffat, 2015; Pardo et al., 2014; Prieto, Cooper,

Fernández, and Cabeza, 2016). Moreover, THS system enables efficient high-temperature power generation cycles, such as the Stirling engine, supercritical Rankine cycle, and supercritical CO_2 power cycle. It overcomes the operational limitation of molten salt heat-transfer fluid above 550 °C, while offering higher energy density and extended storage at ambient temperature. In addition, the wide operating temperature and almost no heat loss in the reaction are the advantages of THS (Gil et al., 2010). THS-based materials stored and released heat following the reversible endo/exothermic reaction (equation (2.3)). The energy densities of stored and released heat are expressed in equation (2.4).

$$AB + \Delta H \leftrightarrow A+B \tag{2.3}$$

$$Q = n_A \Delta H_R \tag{2.4}$$

Where Q is the stored heat (kJ), n_A is the mole of the reactant A (mol), and ΔH_R is the reaction enthalpy (kJ mol^{-1}). During the endothermic reaction step, heat is stored equal to the reaction enthalpy (ΔH) to dissociate AB into the products (A and B). This step is called heat charging step. For heat discharging step, A and B react to reversibly form AB, releasing exothermic heat.

2.3.1 Metal hydrides for TES

Metal hydrides are of significant interest to be used as THS due to their high energy density. It stores and release heat through reversible exothermic and endothermic reactions between hydrogen and metal (equation (2.5)) (Figure 2.11). The latter provides energy up to 2814 kJ/kg with a wide operating pressure and temperature range and it is environmentally friendly (Rönnebro et al., 2015).

$$M + \frac{x}{2} H_2 \leftrightarrow MH_X + \Delta H \tag{2.5}$$

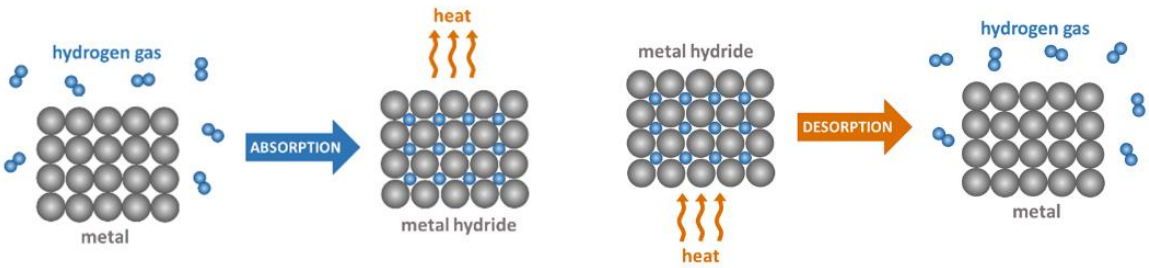

Figure 2.11 schematic diagram of heat charge/discharge mechanisms of metal hydride ("Our Story – Hystorsys AS," n.d.).

Several metal hydrides have been used as THS, such as LiH, CaH_2, and NaH. LiH has formation enthalpies of 181 kJ mol/H_2 for solid LiH and 133.5 kJ mol/H_2 for liquid LiH above 690 °C together with high theoretical H_2 capacity of 12.7 wt. % H_2. However, high temperature ~950 °C is required to generate H_2 equilibrium pressure (P_{eq}) of 1 bar. Besides, the corrosiveness of liquid LiH at this temperature and its high cost hinder practical uses. For CaH_2, very high operating temperature at ~1000 °C requires the use of expensive nickel-based alloy for the container. NaH has favorable operating temperatures for CSP applications. It has P_{eq} of 1 bar H_2 at 425 °C with the capacity of 4.2 wt. % H_2. However, the reversibility of NaH is extremely limited. Liquid Na (melting point of 97.8 °C) forms during the dehydrogenation process and upon the rehydrogenation, a thin NaH layer on the surface of the molten Na restricts further hydrogenation. Due to these disadvantages, the development of metal hydride materials is needed for practical use (Xiaoyi Chen, Zhang, Qi, Ling, and Peng, 2018; Sheppard et al., 2016).

2.4 Coupling of high- and low-temperature hydrides for THS

The idea of coupling high-temperature hydride (HTMH) (e.g., Mg-based hydride) with low-temperature hydride (LTMH) such as AB, AB_2, and AB_5 alloy (e.g. TiFe, $TiMn_x$, $LaNi_5$) has been proposed. In this system, LTMH functions as a hydrogen reservoir, while HTMH acts as the heat storage. During daylight hours, the power plant generates electricity using solar heat, while the excess heat is stored in TES system. The HTMH stores heat at high temperatures (depicted as the red line in Figure 2.12), releasing hydrogen stored in LTMH. HTMH stores significant amount of heat through the

endothermic process at high temperature with high reaction enthalpy. LTMH absorbs hydrogen via the exothermic process, releasing low-temperature heat. During nighttime without sunlight or when additional thermal power is required, the process is reversed. Hydrogen flows from LTMH to HTMH. The external heat is supplied to LTMH and hydrogen absorbs (Figure 2.12). The hydrogen is absorbed by HTMH via exothermic reaction, providing high-temperature heat to the power plant (depicted as the blue line from the HTMH tank in Figure 2.12).

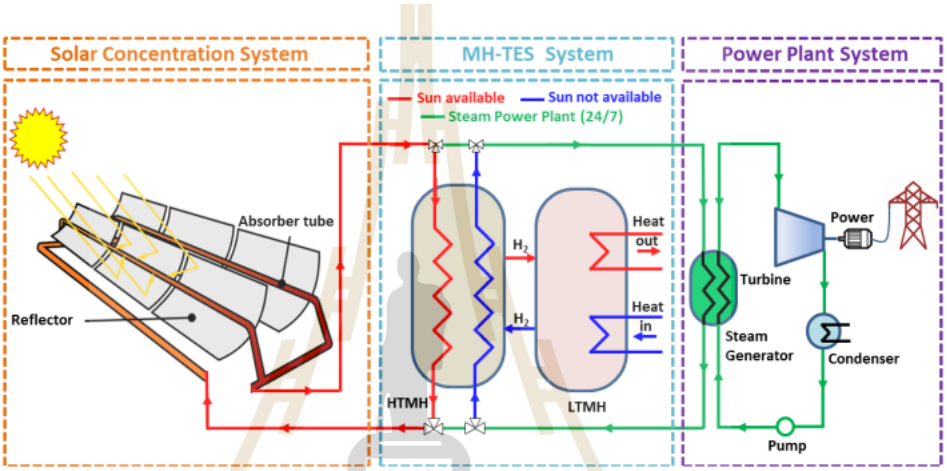

Figure 2.12 Schematic diagram of the concentrating solar power plant using coupled HTMH-LTMH based THS Reprinted with permission from Mellouli et al., 2018. Copyright 2018 Elsevier Ltd.

The ideal Van't Hoff diagram (Figure 2.13) outlines the operational stages of the coupled HTMH-LTMH system. At state 1, HTMH is fully hydrogenated at its minimum working temperature, while LTMH is fully dehydrogenated at ambient temperature. When the heat is introduced during the daytime, dehydrogenation at HTMH takes place, leading to the increase in system pressure. Hydrogenation of LTMH begins when the system pressure exceeds its P_{eq} (state 1 to 2). During nighttime, the temperature of HTMH decreases resulting in the lowering in P_{eq} and activating exothermic hydrogenation process (3 to 4). Simultaneously, LTMH provides hydrogen to HTMH due to the driving force to maintain the P_{eq} of HTMH. When hydrogenation of HTMH is complete, pressure and temperature of both hydrides are returned to state 1.

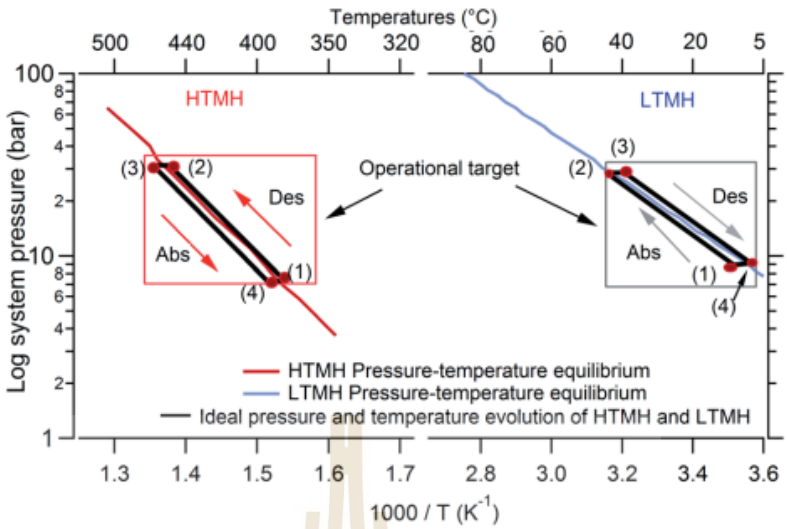

Figure 2.13 Ideal cycle of the selected HTMH and LTMH along with their respective Van't Hoff plots (Poupin, Humphries, Paskevicius, and Buckley, 2019). Reprinted with permission from Poupin et al., 2019. Copyright 2019 Royal Society of Chemistry.

To utilize the coupled HTMH-LTMH heat storage system, compatible reaction temperature and pressure range as well as the fast reaction rate are required for efficiently exchange hydrogen between hydride pair. Figure 2.14 shows the Van’t Hoff plot of some LTMHs versus MgH_2 (HTMH). An ideal LTMH must have an equilibrium line in the shaded area, corresponding to the operating conditions of HTMH.

Among several metal hydrides, MgH_2 with various kinetics improvement methods is attractive for HTMH according to its high reaction enthalpy of 74.5 kJ/mol, leading to large amount of heat released during the exothermic reaction (Aydin et al., 2015). LTMH, such as Ti-based alloys and $LaNi_5$ alloys, are promising as hydrogen reservoir THS systems. $LaNi_5$ alloy with AB_5 structure exhibits rapid sorption kinetics at ambient temperature with low hysteresis (Goodell, Sandrock, and Huston, 1980), (Vucht, Kuijpers, and Bruning, 1970). Moreover, It shows low sensitivity to impurities and can be easily activated (Modi and Aguey-Zinsou, 2021).

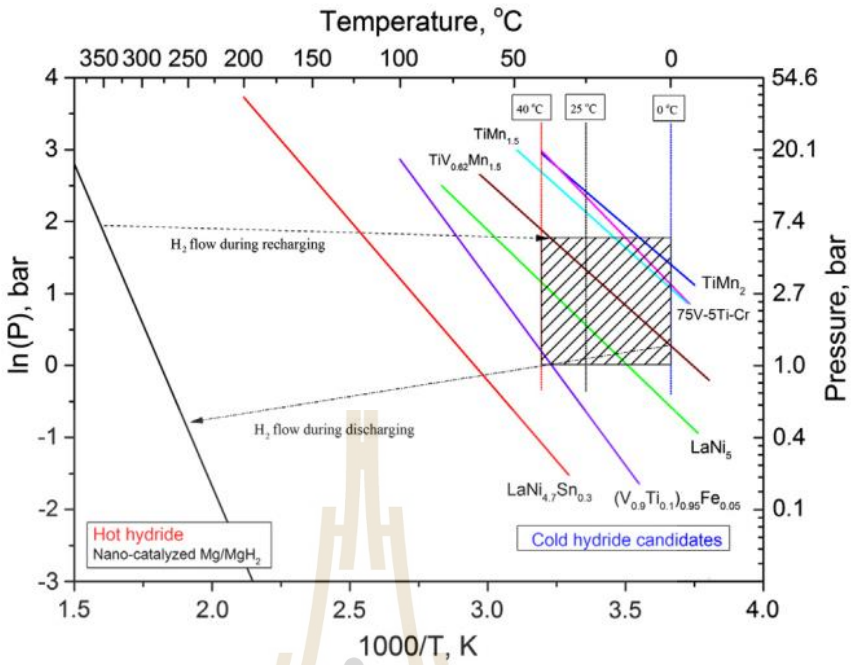

Figure 2.14 Selection of a working pair of hydride materials based on Van't Hoff plot. Reprinted with permission from Fang et al., 2015. Copyright 2015 Elsevier B.V. Published by Elsevier B.V.

Experimental and computational investigations have proposed the use of Mg-based HTMHs paired with various LTMHs for TES systems. For example, Mg_2FeH_6 paired with $TiMn_{1.5}H_x$ or Na_3AlH_6 (d'Entremont et al., 2017; Mellouli et al., 2018), Mg_2Ni-$LaNi_5$ (Malleswararao, N, Srinivasa Murthy, and Dutta, 2020; Nyamsi and Tolj, 2021), $NaMgH_2F$-$Ti_{1.2}Mn_{1.8}$ (Sheppard et al., 2014), MgH_2+$LaNi_5$ coupled with $LaNi_{(5-x)}Al_x$ (x=0.3 and 0.4) or $La_{(1-y)}Ce_yNi_5$ (y=0.1 and 0.2) (Sarath Babu, Anil Kumar, and Srinivasa Murthy, 2023), MgH_2 coupled with $Ti_{0.98}Zr_{0.02}V_{0.43}Fe_{0.09}Cr_{0.05}Mn_x$ (x=1.2 and 1.5) (Bogdanović, Ritter, and Spliethoff, 1990; Wierse, Werner, and Groll, 1991) or $(TiZr)(MnFCr)_2$ (Nyamsi, Davids, Tolj, Pasupathi, and Lototskyy, 2023), and $TiMn_2$-catalyzed MgH_2-$TiV_{0.62}Mn_{1.5}$ (Fang et al., 2015). Mg_2FeH_6-based HTMH combined with $TiMn_{1.5}H_x$ operating at the temperature range of 350-500 °C achieved an impressive energy storage density (ESD) of 1488 kJ/kg (Poupin et al., 2019). On the other hand, the Mg_2FeH_6-Na_3AlH_6 system showed potential for utilization at higher temperatures of 450-500 °C, with the volumetric energy density of 132 kWh/m^3 (more than 5 times larger than the U.S. DOE SunShot target of 25 kWh/m^3 (d'Entremont et al., 2017)). Composite of MgH_2+$LaNi_5$ (5–50 wt. %) were

combined with $LaNi_{(5-x)}Al_x$ (x = 0.3 and 0.4) or $La_{(1-y)}Ce_yNi_5$ (y = 0.1 and 0.2) to optimize TES performance. The pairing of Mg+20 wt. % $LaNi_5$ with $LaNi_{4.7}Al_{0.3}$ demonstrated the highest operating temperature range, leading to the maximum heat upgradation of 34 °C. The combination of Mg+5 wt. % $LaNi_5$ with $La_{0.8}Ce_{0.2}Ni_5$ revealed the highest coefficient of performance (COP) and ESD up to 0.705 and 418.84 kJ/kg, respectively. This superior performance was attributed to the high hydrogen absorption capacity and reaction enthalpy of Mg+5 wt. % $LaNi_5$ (Sarath Babu et al., 2023).

2.5 References

Adelhelm, P., and De Jongh, P. E. (2011). The impact of carbon materials on the hydrogen storage properties of light metal hydrides. *Journal of Materials Chemistry*, *21*(8), 2417–2427. https://doi.org/10.1039/c0jm02593c

Aguey-Zinsou, K. F., Ares Fernandez, J. R., Klassen, T., and Bormann, R. (2007). Effect of Nb_2O_5 on MgH_2 properties during mechanical milling. *International Journal of Hydrogen Energy*, *32*(13), 2400–2407. https://doi.org/10.1016/J.IJHYDENE.2006.10.068

Aguey-Zinsou, Kondo Franois, and Ares-Fernández, J. R. (2010). Hydrogen in magnesium: new perspectives toward functional stores. *Energy and Environmental Science*, *3*(5), 526–543. https://doi.org/10.1039/B921645F

Awad, A. S., Nakhl, M., Zakhour, M., Santos, S. F., Souza, F. L., and Bobet, J. L. (2016). Effect of microwave irradiation on hydrogen sorption properties of hand mixed MgH_2 - 10 wt.% carbon fibers. *Journal of Alloys and Compounds*, *676*, 1–8. https://doi.org/10.1016/j.jallcom.2016.03.008

Aydin, D., Casey, S. P., and Riffat, S. (2015). The latest advancements on thermochemical heat storage systems. *Renewable and Sustainable Energy Reviews*, Vol. 41, pp. 356–367. Elsevier Ltd. https://doi.org/10.1016/j.rser.2014.08.054

Barkhordarian, G., Klassen, T., and Bormann, R. (2003). Fast hydrogen sorption kinetics of nanocrystalline Mg using Nb_2O_5 as catalyst. *Scripta Materialia*, *49*(3), 213–217. https://doi.org/10.1016/S1359-6462(03)00259-8

Barkhordarian, G., Klassen, T., and Bormann, R. U. (2004). Effect of Nb_2O_5 content on hydrogen reaction kinetics of Mg. *Journal of Alloys and Compounds*, *364*(1–2), 242–246. https://doi.org/10.1016/S0925-8388(03)00530-9

Bastos-Neto, M., Patzschke, C., Lange, M., Möllmer, J., Möller, A., Fichtner, S., ... Gläser, R. (2012). Assessment of hydrogen storage by physisorption in porous materials. *Energy and Environmental Science*, *5*(8), 8294–8303. https://doi.org/10.1039/C2EE22037G

Bhouri, M., Goyette, J., Hardy, B. J., and Anton, D. L. (2011). Honeycomb metallic structure for improving heat exchange in hydrogen storage system. *International*

Journal of Hydrogen Energy, *36*(11), 6723–6738. https://doi.org/10.1016/j.ijhydene.2011.02.092

Bogdanović, B., Ritter, A., and Spliethoff, B. (1990). Active MgH_2-Mg Systems for Reversible Chemical Energy Storage. *Angewandte Chemie International Edition in English*, *29*(3), 223–328. https://doi.org/10.1002/anie.199002233

Cabo, M., Garroni, S., Pellicer, E., Milanese, C., Girella, A., Marini, A., ... Baró, M. D. (2011). Hydrogen sorption performance of MgH_2 doped with mesoporous nickel- and cobalt-based oxides. *International Journal of Hydrogen Energy*, *36*(9), 5400–5410. https://doi.org/10.1016/j.ijhydene.2011.02.038

Chaise, A., de Rango, P., Marty, P., Fruchart, D., Miraglia, S., Olivès, R., and Garrier, S. (2009). Enhancement of hydrogen sorption in magnesium hydride using expanded natural graphite. *International Journal of Hydrogen Energy*, *34*(20), 8589–8596. https://doi.org/10.1016/j.ijhydene.2009.07.112

Chen, Xi, Zou, J., Zeng, X., and Ding, W. (2016). Hydrogen storage in $Mg_2Fe(Ni)H_6$ nanowires synthesized from coarse-grained Mg and nano sized γ-Fe(Ni) precursors. *International Journal of Hydrogen Energy*, *41*(33), 14795–14806. https://doi.org/10.1016/J.IJHYDENE.2016.06.024

Chen, Xiaoyi, Zhang, Z., Qi, C., Ling, X., and Peng, H. (2018). State of the art on the high-temperature thermochemical energy storage systems. *Energy Conversion and Management*, *177*(September), 792–815. https://doi.org/10.1016/j.enconman.2018.10.011

Chibani, A., and Bougriou, C. (2017). Effect of the tank geometry on the storage and destocking of hydrogen on metal hydride ($LaNi_5$–H_2). *International Journal of Hydrogen Energy*, *42*(36), 23035–23044. https://doi.org/10.1016/j.ijhydene.2017.07.102

Cui, J., Liu, J., Wang, H., Ouyang, L., Sun, D., Zhu, M., and Yao, X. (2014). Mg–TM (TM: Ti, Nb, V, Co, Mo or Ni) core–shell like nanostructures: synthesis, hydrogen storage performance and catalytic mechanism. *Journal of Materials Chemistry A*, *2*(25), 9645–9655. https://doi.org/10.1039/C4TA00221K

Cui, J., Wang, H., Liu, J., Ouyang, L., Zhang, Q., Sun, D., ... Zhu, M. (2013). Remarkable enhancement in dehydrogenation of MgH_2 by a nano-coating of multi-valence Ti-

based catalysts. *Journal of Materials Chemistry A*, *1*(18), 5603–5611. https://doi.org/10.1039/C3TA01332D

d'Entremont, A., Corgnale, C., Sulic, M., Hardy, B., Zidan, R., and Motyka, T. (2017). Modeling of a thermal energy storage system based on coupled metal hydrides (magnesium iron – sodium alanate) for concentrating solar power plants. *International Journal of Hydrogen Energy*, *42*(35), 22518–22529. https://doi.org/10.1016/J.IJHYDENE.2017.04.231

Dornheim, M., Doppiu, S., Barkhordarian, G., Boesenberg, U., Klassen, T., Gutfleisch, O., and Bormann, R. (2007). Hydrogen storage in magnesium-based hydrides and hydride composites. *Scripta Materialia*, *56*(10), 841–846. https://doi.org/10.1016/j.scriptamat.2007.01.003

El Khatabi, M., Bhihi, M., Naji, S., Labrim, H., Benyoussef, A., El Kenz, A., and Loulidi, M. (2016). Study of doping effects with 3d and 4d-transition metals on the hydrogen storage properties of MgH_2. *International Journal of Hydrogen Energy*, *41*(8), 4712–4718. https://doi.org/10.1016/j.ijhydene.2016.01.001

Fang, Z. Z., Zhou, C., Fan, P., Udell, K. S., Bowman, R. C., Vajo, J. J., ... Kekelia, B. (2015). Metal hydrides based high energy density thermal battery. *Journal of Alloys and Compounds*, *645*(S1), S184–S189. https://doi.org/10.1016/J.JALLCOM.2014.12.260

Fuster, V., Castro, F. J., Troiani, H., and Urretavizcaya, G. (2011). Characterization of graphite catalytic effect in reactively ball-milled MgH_2-C and Mg-C composites. *International Journal of Hydrogen Energy*, *36*(15), 9051–9061. https://doi.org/10.1016/j.ijhydene.2011.04.153

G. Liang, J. Huot, S. Boily, A. Van Neste, and R. Schulz. (1999). Catalytic effect of transition metals on hydrogen sorption innanocrystalline ball milled MgH –Tm (Tm5Ti, V, Mn, Fe and Ni). *Journal of Alloys and Compounds*, *292*, 247–292.

Garrier, S., Chaise, A., De Rango, P., Marty, P., Delhomme, B., Fruchart, D., and Miraglia, S. (2011). MgH_2 intermediate scale tank tests under various experimental conditions. *International Journal of Hydrogen Energy*, *36*(16), 9719–9726. https://doi.org/10.1016/j.ijhydene.2011.05.017

Gil, A., Medrano, M., Martorell, I., Lázaro, A., Dolado, P., Zalba, B., and Cabeza, L. F. (2010). State of the art on high temperature thermal energy storage for power generation. Part 1—Concepts, materials and modellization. *Renewable and Sustainable Energy Reviews*, *14*(1), 31–55. https://doi.org/10.1016/J.RSER.2009.07.035

Goodell, P. D., Sandrock, G. D., and Huston, E. L. (1980). Kinetic and dynamic aspects of rechargeable metal hydrides. *Journal of the Less Common Metals*, *73*(1), 135–142. https://doi.org/10.1016/0022-5088(80)90352-5

Grigorova, E., Khristov, M., Stoycheva, I., and Tsyntsarski, B. (2017). Effect of activated carbon from polyolefin wax on the hydrogensorption properties of magnesium. *International Journal of Hydrogen Energy*, *42*(43), 26872–26876. https://doi.org/10.1016/J.IJHYDENE.2017.06.155

Grigorova, E., Mandzhukova, T., Tsyntsarski, B., Budinova, T., Khristov, M., Tzvetkov, P., ... Petrov, N. (2011). Effect of activated carbons derived from different precursors on the hydrogen sorption properties of magnesium. *Fuel Processing Technology*, *92*(10), 1963–1969. https://doi.org/10.1016/J.FUPROC.2011.05.016

Gupta, A., Baron, G. V., Perreault, P., Lenaerts, S., Ciocarlan, R. G., Cool, P., ... Denayer, J. F. M. (2021, October 1). Hydrogen Clathrates: Next Generation Hydrogen Storage Materials. *Energy Storage Materials*, Vol. 41, pp. 69–107. Elsevier B.V. https://doi.org/10.1016/j.ensm.2021.05.044

Hanada, N., Ichikawa, T., and Fujii, H. (2005). Catalytic effect of nanoparticle 3d-transition metals on hydrogen storage properties in magnesium hydride MgH_2 prepared by mechanical milling. *Journal of Physical Chemistry B*, *109*(15), 7188–7194. https://doi.org/10.1021/jp044576c

Hardian, R., Pistidda, C., Chaudhary, A. L., Capurso, G., Gizer, G., Cao, H., ... Dornheim, M. (2018). Waste Mg-Al based alloys for hydrogen storage. *International Journal of Hydrogen Energy*, *43*(34), 16738–16748. https://doi.org/10.1016/j.ijhydene.2017.12.014

Herrich, M., Ismail, N., Lyubina, J., Handstein, A., Pratt, A., and Gutfleisch, O. (2004). Synthesis and decomposition of Mg_2FeH_6 prepared by reactive milling. *Materials*

Science and Engineering: B, *108*(1–2), 28–32. https://doi.org/10.1016/J.MSEB.2003.10.031

Hitam, C. N. C., Aziz, M. A. A., Ruhaimi, A. H., and Taib, M. R. (2021). Magnesium-based alloys for solid-state hydrogen storage applications: A review. *International Journal of Hydrogen Energy*, *46*(60), 31067–31083. https://doi.org/10.1016/j.ijhydene.2021.03.153

Huot, J., Liang, G., Boily, S., Van Neste, A., and Schulz, R. (1999). Structural study and hydrogen sorption kinetics of ball-milled magnesium hydride. *Journal of Alloys and Compounds*, *293–295*, 495–500. https://doi.org/10.1016/S0925-8388(99)00474-0

Huot, J., Tremblay, M. L., and Schulz, R. (2003). Synthesis of nanocrystalline hydrogen storage materials. *Journal of Alloys and Compounds*, *356–357*, 603–607. https://doi.org/10.1016/S0925-8388(03)00120-8

Im, J. S., Park, S. J., Kim, T. J., Kim, Y. H., and Lee, Y. S. (2008). The study of controlling pore size on electrospun carbon nanofibers for hydrogen adsorption. *Journal of Colloid and Interface Science*, *318*(1), 42–49. https://doi.org/10.1016/J.JCIS.2007.10.024

Im, J. S., Park, S. J., and Lee, Y. S. (2009). Superior prospect of chemically activated electrospun carbon fibers for hydrogen storage. *Materials Research Bulletin*, *44*(9), 1871–1878. https://doi.org/10.1016/J.MATERRESBULL.2009.05.010

Ismail, M., Juahir, N., and Mustafa, N. S. (2014). Improved hydrogen storage properties of MgH_2 Co-doped with $FeCl_3$ and carbon nanotubes. *Journal of Physical Chemistry C*, *118*(33), 18878–18883. https://doi.org/10.1021/JP5046436/ASSET/IMAGES/MEDIUM/JP-2014-046436_0013.GIF

Jia, Y., Guo, Y., Zou, J., and Yao, X. (2012). Hydrogenation/dehydrogenation in MgH_2-activated carbon composites prepared by ball milling. *International Journal of Hydrogen Energy*, *37*(9), 7579–7585. https://doi.org/10.1016/j.ijhydene.2012.01.015

Jin, S. A., Shim, J. H., Cho, Y. W., and Yi, K. W. (2007). Dehydrogenation and hydrogenation characteristics of MgH_2 with transition metal fluorides. *Journal of Power Sources*, *172*(2), 859–862. https://doi.org/10.1016/J.JPOWSOUR.2007.04.090

Kaplan, Y. (2009). Effect of design parameters on enhancement of hydrogen charging in metal hydride reactors. *International Journal of Hydrogen Energy*, *34*(5), 2288–2294. https://doi.org/10.1016/j.ijhydene.2008.12.096

Khan, D., Zou, J., Zeng, X., and Ding, W. (2018). Hydrogen storage properties of nanocrystalline Mg_2Ni prepared from compressed $2MgH_2$–Ni powder. *International Journal of Hydrogen Energy*, *43*(49), 22391–22400. https://doi.org/10.1016/J.IJHYDENE.2018.10.055

Klopčič, N., Grimmer, I., Winkler, F., Sartory, M., and Trattner, A. (2023). A review on metal hydride materials for hydrogen storage. *Journal of Energy Storage*, *72*, 108456. https://doi.org/10.1016/J.EST.2023.108456

Korablov, D., Nielsen, T. K., Besenbacher, F., and Jensen, T. R. (2015). Mechanism and kinetics of early transition metal hydrides, oxides, and chlorides to enhance hydrogen release and uptake properties of MgH_2. *Powder Diffraction*, *30*, S9–S15. Cambridge University Press. https://doi.org/10.1017/S0885715615000056

Kumar, S., Kojima, Y., and Dey, G. K. (2017). Morphological effects of Nb_2O_5 on Mg–MgH_2 system for thermal energy storage application. *International Journal of Hydrogen Energy*, *43*(2), 809–816. https://doi.org/10.1016/J.IJHYDENE.2017.11.039

Lee, S. Y., Lee, J. H., Kim, Y. H., Kim, J. W., Lee, K. J., and Park, S. J. (2022). Recent Progress Using Solid-State Materials for Hydrogen Storage: A Short Review. *Processes*, *10*(2). https://doi.org/10.3390/PR10020304

Ley, M. B., Jepsen, L. H., Lee, Y. S., Cho, Y. W., Bellosta Von Colbe, J. M., Dornheim, M., ... Jensen, T. R. (2014). Complex hydrides for hydrogen storage - New perspectives. *Materials Today*, Vol. 17, pp. 122–128. Elsevier B.V. https://doi.org/10.1016/j.mattod.2014.02.013

Lillo-Ródenas, M. A., Guo, Z. X., Aguey-Zinsou, K. F., Cazorla-Amorós, D., and Linares-Solano, A. (2008). Effects of different carbon materials on MgH_2 decomposition. *Carbon*, *46*(1), 126–137. https://doi.org/10.1016/j.carbon.2007.10.033

Liu, T., Ma, X., Chen, C., Xu, L., and Li, X. (2015). Catalytic effect of Nb nanoparticles for improving the hydrogen storage properties of Mg-based nanocomposite. *Journal of Physical Chemistry C*, *119*(25), 14029–14037. https://doi.org/10.1021/ACS.JPCC.5B03442/ASSET/IMAGES/LARGE/JP-2015-03442J_0008.JPEG

Lu, Z.-Y., Yu, H.-J., Lu, X., Song, M.-C., Wu, F.-Y., Zheng, J.-G., ... Zhang, L.-T. (2021). Two-dimensional vanadium nanosheets as a remarkably effective catalyst for hydrogen storage in MgH_2. *Rare Metals*. https://doi.org/10.1007/s12598

Ma, L. P., Kang, X. D., Dai, H. B., Liang, Y., Fang, Z. Z., Wang, P. J., ... Cheng, H. M. (2009a). Superior catalytic effect of TiF_3 over $TiCl_4$ in improving the hydrogen sorption kinetics of MgH_2: Catalytic role of fluorine anion. *Acta Materialia*, *57*(7), 2250–2258. https://doi.org/10.1016/j.actamat.2009.01.025

Ma, Z., Liu, J., Zhu, Y., Zhao, Y., Lin, H., Zhang, Y., ... Li, L. (2020). Crystal-facet-dependent catalysis of anatase TiO_2 on hydrogen storage of MgH_2. *Journal of Alloys and Compounds*, *822*. https://doi.org/10.1016/j.jallcom.2019.153553

Malleswararao, K., N, A., Srinivasa Murthy, S., and Dutta, P. (2020). Performance prediction of a coupled metal hydride based thermal energy storage system. *International Journal of Hydrogen Energy*, *45*(32), 16239–16253. https://doi.org/10.1016/J.IJHYDENE.2020.03.251

Mellouli, S., Askri, F., Edacherian, A., Alqahtani, T., Algarni, S., Abdelmajid, J., and Phelan, P. (2018). Performance analysis of a thermal energy storage system based on paired metal hydrides for concentrating solar power plants. *Applied Thermal Engineering*, *144*, 1017–1029. https://doi.org/10.1016/J.APPLTHERMALENG.2018.09.014

Modi, P., and Aguey-Zinsou, K. F. (2021). Room Temperature Metal Hydrides for Stationary and Heat Storage Applications: A Review. *Frontiers in Energy Research*, *9*, 616115. https://doi.org/10.3389/FENRG.2021.616115/BIBTEX

Nguyen, H. Q., and Shabani, B. (2021). Review of metal hydride hydrogen storage thermal management for use in the fuel cell systems. *International Journal of Hydrogen Energy*, *46*(62), 31699–31726. https://doi.org/10.1016/J.IJHYDENE.2021.07.057

Nielsen, T. K., and Jensen, T. R. (2012). MgH_2-Nb_2O_5 investigated by in situ synchrotron X-ray diffraction. *International Journal of Hydrogen Energy*, *37*(18), 13409–13416. https://doi.org/10.1016/j.ijhydene.2012.06.082

Nielsen, T. K., Manickam, K., Hirscher, M., Besenbacher, F., and Jensen, T. R. (2009). Confinement of MgH_2 Nanoclusters within nanoporous aerogel scaffold materials. *ACS Nano*, *3*(11), 3521–3528. https://doi.org/10.1021/nn901072w

Nishimura, C., Komaki, M., and Amano, M. (1999). Hydrogen permeation through magnesium. *Journal of Alloys and Compounds*, *293–295*, 329–333. https://doi.org/10.1016/S0925-8388(99)00373-4

Nyamsi, S. N., Davids, W., Tolj, I., Pasupathi, S., and Lototskyy, M. (2023). Heat discharge performance of metal hydride thermal battery under different heat transfer conditions: Experimental findings. *Journal of Energy Storage*, *72*, 108353. https://doi.org/10.1016/J.EST.2023.108353

Nyamsi, S. N., and Tolj, I. (2021). The impact of active and passive thermal management on the energy storage efficiency of metal hydride pairs based heat storage. *Energies*, *14*(11), 1–24. https://doi.org/10.3390/en14113006

Oelerich, W., Klassen, T., and Bormann, R. (2001). Metal oxides as catalysts for improved hydrogen sorption in nanocrystalline Mg-based materials. *Journal of Alloys and Compounds*, *315*(1–2), 237–242. https://doi.org/10.1016/S0925-8388(00)01284-6

Our story – Hystorsys AS. (n.d.). Retrieved January 18, 2024, from https://www.hystorsys.no/our-story/

Ouyang, L., Liu, F., Wang, H., Liu, J., Yang, X. S., Sun, L., and Zhu, M. (2020, August 15). Magnesium-based hydrogen storage compounds: A review. *Journal of Alloys and Compounds*, Vol. 832. Elsevier Ltd. https://doi.org/10.1016/j.jallcom.2020.154865

Pardo, P., Deydier, A., Anxionnaz-Minvielle, Z., Rougé, S., Cabassud, M., and Cognet, P. (2014, April). A review on high temperature thermochemical heat energy storage. *Renewable and Sustainable Energy Reviews*, Vol. 32, pp. 591–610. https://doi.org/10.1016/j.rser.2013.12.014

Plerdsranoy, P., Thiangviriya, S., Dansirima, P., Thongtan, P., Kaewsuwan, D., Chanlek, N., and Utke, R. (2019). Synergistic effects of transition metal halides and activated

carbon nanofibers on kinetics and reversibility of MgH_2. *Journal of Physics and Chemistry of Solids*, *124*, 81–88. https://doi.org/10.1016/j.jpcs.2018.09.001

Poupin, L., Humphries, T. D., Paskevicius, M., and Buckley, C. E. (2019). An experimental high temperature thermal battery coupled to a low temperature metal hydride for solar thermal energy storage. *Sustainable Energy and Fuels*, *4*(1), 285–292. https://doi.org/10.1039/c9se00538b

Prieto, C., Cooper, P., Fernández, A. I., and Cabeza, L. F. (2016). Review of technology: Thermochemical energy storage for concentrated solar power plants. *Renewable and Sustainable Energy Reviews*, *60*, 909–929. https://doi.org/10.1016/J.RSER.2015.12.364

Pukazhselvan, D., Sandhya, K. S., Ramasamy, D., Shaula, A., and Fagg, D. P. (2020). Transformation of Metallic Ti to TiH_2 Phase in the Ti/MgH_2 Composite and Its Influence on the Hydrogen Storage Behavior of MgH_2. *ChemPhysChem*, *21*(11), 1195–1201. https://doi.org/10.1002/CPHC.202000031

Rahmaninasab, M. A., Raygan, S., Abdizadeh, H., Pourabdoli, M., and Mirghaderi, S. H. (2018). Properties of activated MgH_2 + mischmetal nanostructured composite produced by ball-milling. *Materials for Renewable and Sustainable Energy*, *7*(3), 1–11. https://doi.org/10.1007/S40243-018-0122-Z/FIGURES/13

Rönnebro, E. C. E., Whyatt, G., Powell, M., Westman, M., Zheng, F., and Fang, Z. Z. (2015). Metal hydrides for high-temperature power generation. *Energies*, *8*(8), 8406–8430. https://doi.org/10.3390/en8088406

Rud, A. D., and Lakhnik, A. M. (2012). Effect of carbon allotropes on the structure and hydrogen sorption during reactive ball-milling of Mg–C powder mixtures. *International Journal of Hydrogen Energy*, *37*(5), 4179–4187. https://doi.org/10.1016/J.IJHYDENE.2011.11.123

Rud, A. D., Lakhnik, A. M., Ivanchenko, V. G., Uvarov, V. N., Shkola, A. A., Dekhtyarenko, V. A., ... Kuskova, N. I. (2008). Hydrogen storage of the Mg–C composites. *International Journal of Hydrogen Energy*, *33*(4), 1310–1316. https://doi.org/10.1016/J.IJHYDENE.2007.12.032

Sarath Babu, K., Anil Kumar, E., and Srinivasa Murthy, S. (2023). Thermochemical energy storage using coupled metal hydride beds of Mg-$LaNi_5$ composites and $LaNi_5$

based hydrides for concentrated solar power plants. *Applied Thermal Engineering*, *219*, 119521. https://doi.org/10.1016/J.APPLTHERMALENG.2022.119521

Schlapbach, L., and Züttel, A. (2001). *Hydrogen-storage materials for mobile applications*. Retrieved from www.nature.com

Sevilla, M., and Mokaya, R. (2014). Energy storage applications of activated carbons: supercapacitors and hydrogen storage. *Energy and Environmental Science*, *7*(4), 1250–1280. https://doi.org/10.1039/C3EE43525C

Shang, C. X., and Guo, Z. X. (2004). Effect of carbon on hydrogen desorption and absorption of mechanically milled MgH_2. *Journal of Power Sources*, *129*(1), 73–80. https://doi.org/10.1016/J.JPOWSOUR.2003.11.013

Sheffield, J. W., Martin, K. B., and Folkson, R. (2014). Electricity and hydrogen as energy vectors for transportation vehicles. In *Alternative Fuels and Advanced Vehicle Technologies for Improved Environmental Performance: Towards Zero Carbon Transportation* (pp. 117–137). Elsevier Inc. https://doi.org/10.1533/9780857097422.1.117

Sheppard, D. A., Corgnale, C., Hardy, B., Motyka, T., Zidan, R., Paskevicius, M., and Buckley, C. E. (2014). Hydriding characteristics of $NaMgH_2F$ with preliminary technical and cost evaluation of magnesium-based metal hydride materials for concentrating solar power thermal storage. *RSC Advances*, *4*(51), 26552–26562. https://doi.org/10.1039/C4RA01682C

Sheppard, D. A., Paskevicius, M., Humphries, T. D., Felderhoff, M., Capurso, G., Bellosta von Colbe, J., ... Buckley, C. E. (2016). Metal hydrides for concentrating solar thermal power energy storage. *Applied Physics A: Materials Science and Processing*, *122*(4). https://doi.org/10.1007/s00339-016-9825-0

Si, T. Z., Zhang, X. Y., Feng, J. J., Ding, X. L., and Li, Y. T. (2021). Enhancing hydrogen sorption in MgH_2 by controlling particle size and contact of Ni catalysts. *Rare Metals*, *40*(4), 995–1002. https://doi.org/10.1007/s12598-018-1087-x

Souahlia, A., Dhaou, H., Mellouli, S., Askri, F., Jemni, A., and Ben Nasrallah, S. (2014). Experimental study of metal hydride-based hydrogen storage tank at constant supply pressure. *International Journal of Hydrogen Energy*, *39*(14), 7365–7372. https://doi.org/10.1016/j.ijhydene.2014.02.121

Sterl, F., Linnenbank, H., Steinle, T., Mörz, F., Strohfeldt, N., and Giessen, H. (2018). Nanoscale Hydrogenography on Single Magnesium Nanoparticles. *Nano Letters*, *18*(7), 4293–4302. https://doi.org/10.1021/acs.nanolett.8b01277

Thaweelap, N., Thongtan, P., Sitthiwet, C., Thiangviriya, S., Eiamlamai, P., and Utke, R. (2017). Hydrogen sorption, kinetics, reversibility, and reaction mechanisms of MgH_2-x$LiBH_4$ doped with activated carbon nanofibers for reversible hydrogen storage-based laboratory powder and tank scales. *International Journal of Hydrogen Energy*, *42*(39), 24915–24926. https://doi.org/10.1016/j.ijhydene.2017.08.075

Valentoni, A., Mulas, G., Enzo, S., and Garroni, S. (2018). Remarkable hydrogen storage properties of MgH2 doped with $VNbO_5$. *Physical Chemistry Chemical Physics*, *20*(6), 4100–4108. https://doi.org/10.1039/c7cp07157d

Varin, R. A., Czujko, T., Chiu, C., and Wronski, Z. (2006). Particle size effects on the desorption properties of nanostructured magnesium dihydride (MgH_2) synthesized by controlled reactive mechanical milling (CRMM). *Journal of Alloys and Compounds*, *424*(1–2), 356–364. https://doi.org/10.1016/J.JALLCOM.2005.12.087

Vucht, J. V., Kuijpers, F., and Bruning, H. (1970). Reversible room-temperature absorption of large quantities of hydrogen by intermetallic compounds.

Wang, P., Tian, Z., Wang, Z., Xia, C., Yang, T., and Ou, X. (2021). Improved hydrogen storage properties of MgH_2 using transition metal sulfides as catalyst. *International Journal of Hydrogen Energy*, *46*(53), 27107–27118. https://doi.org/10.1016/j.ijhydene.2021.05.172

Wang, Y., Wang, Y., Zhang, Q., Jiao, L., and Yuan, H. (2015). Catalytic effects of different Ti-based materials on dehydrogenation performances of MgH_2. *Journal of Alloys and Compounds*, *645*(S1), S509–S512. https://doi.org/10.1016/J.JALLCOM.2014.12.071

Wierse, M., Werner, R., and Groll, M. (1991). Magnesium hydride for thermal energy storage in a small-scale solar-thermal power station. *Journal of the Less Common Metals*, *172–174*(PART 3), 1111–1121. https://doi.org/10.1016/S0022-5088(06)80018-4

Wu, Z., Yang, F., Zhang, Z., and Bao, Z. (2014). Magnesium based metal hydride reactor incorporating helical coil heat exchanger: Simulation study and optimal design. *Applied Energy*, *130*, 712–722. https://doi.org/10.1016/j.apenergy.2013.12.071

Xie, L., Liu, Y., Wang, Y. T., Zheng, J., and Li, X. G. (2007). Superior hydrogen storage kinetics of MgH_2 nanoparticles doped with TiF_3. *Acta Materialia*, *55*(13), 4585–4591. https://doi.org/10.1016/j.actamat.2007.04.020

Yu, H., Bennici, S., and Auroux, A. (2014). Hydrogen storage and release: Kinetic and thermodynamic studies of MgH_2 activated by transition metal nanoparticles. *International Journal of Hydrogen Energy*, *39*(22), 11633–11641. https://doi.org/10.1016/j.ijhydene.2014.05.069

Zaluska, A, Zaluski, L., and Strom-Olsen´centre, J. O. (1999). Nanocrystalline magnesium for hydrogen storage. In *Journal of Alloys and Compounds* (Vol. 288).

Zhang, J., Zhu, Y., Lin, H., Liu, Y., Zhang, Y., Li, S., Li, L. (2017). Metal Hydride Nanoparticles with Ultrahigh Structural Stability and Hydrogen Storage Activity Derived from Microencapsulated Nanoconfinement. *Advanced Materials (Deerfield Beach, Fla.)*, *29*(24). https://doi.org/10.1002/ADMA.201700760

Zhou, C., Zhang, J., Bowman, R. C., and Fang, Z. Z. (2021). Roles of Ti-Based Catalysts on Magnesium Hydride and Its Hydrogen Storage Properties. *Inorganics 2021, Vol. 9, Page 36*, *9*(5), 36. https://doi.org/10.3390/INORGANICS9050036

Zhou, S., Zhang, X., Li, T., Wang, N., Chen, H., Zhang, T., Liu, D. (2014). Nano-confined magnesium for hydrogen storage from reactive milling with anthracite carbon as milling aid. *International Journal of Hydrogen Energy*, *39*(25), 13628–13633. https://doi.org/10.1016/J.IJHYDENE.2014.02.092

Zlotea, C., Oumellal, Y., Hwang, S. J., Ghimbeu, C. M., De Jongh, P. E., and Latroche, M. (2015). Ultrasmall MgH_2 Nanoparticles Embedded in an Ordered Microporous Carbon Exhibiting Rapid Hydrogen Sorption Kinetics. *Journal of Physical Chemistry C*, *119*(32), 18091–18098. https://doi.org/10.1021/acs.jpcc.5b05754

Züttel, A. (2003). Materials for hydrogen storage. *Materials Today*, *6*(9), 24–33. https://doi.org/10.1016/S1369-7021(03)00922-2

CHAPTER III

EXPERIMENTAL SECTION

3.1 Sample preparation

This research involved the use of hydrides, which are highly reactive with moisture and oxygen. All operations were carried out in an inert gas atmosphere in a N_2-filled glove box (Figure 3.1).

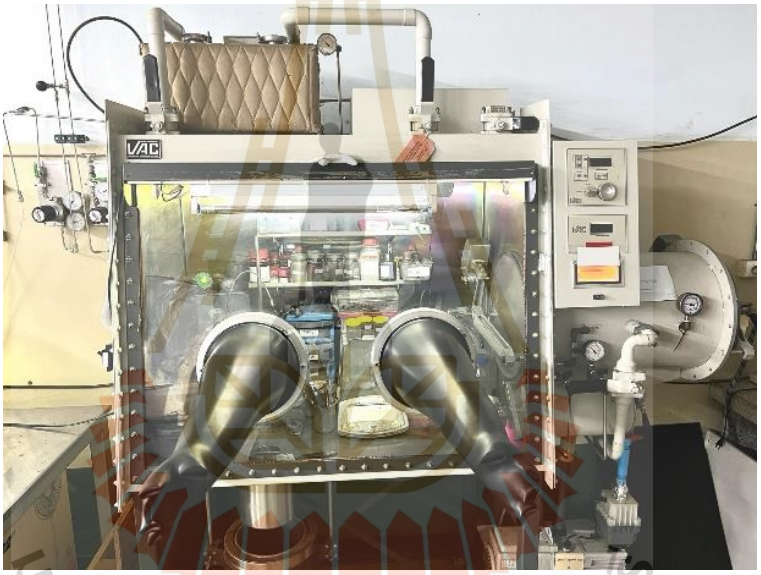

Figure 3.1 N_2-filled glove box (Omni-Lab System, VAC).

3.1.1 MgH_2-based hydrogen storage materials

3.1.1.1 MgH_2 doped with TiF_4 and activated carbon

As-received Mg powder (≥99.0%, Aldrich) was hydrogenated at 350 °C under 80 bar H_2 for 12 h to obtain as-prepared MgH_2. As-received TiF_4 (99%, Acros Organics) and as-prepared MgH_2 was milled for 3 and 2 h, respectively, by using a QM0.4L Planetary Ball Mill, Nanjing Chishun Science & Technology (Figure 3.2(A)).

(A) (B)

Figure 3.2 QM0.4L 4 pots planetary ball mill (A) and Retch PM100 planetary ball mill (B).

Ball-to-powder weight ratio (BPR) and rotational speed were 20:1 and 600 rpm, respectively. As-prepared MgH_2 was doped with 5 wt. % milled TiF_4 by milling for 30 min with BPR of 20:1. Hydrogenation was repeated by pressurizing 80 bar H_2 on MgH_2-5 wt. % TiF_4 at 350 °C for 12 h. Activated carbon (AC, a C. Gigantic Carbon Co., Ltd., Thailand) was treated at 500 °C under vacuum for 3 h to remove oxygen and moisture. Hydrogenated sample of MgH_2-5 wt. % TiF_4 was doped with 5 wt. % treated AC by ball milling for 30 min to obtain MgH_2-5 wt. % TiF_4-5 wt. % AC, denoted as MgH_2-TiF_4-AC. The powder sample of MgH_2-TiF_4-AC (14.4918 g) was packed tightly into a cylindrical tank with packing volume of 28.8 mL (SS304) (Figure 3.3(A)) under nitrogen atmosphere in the glove box. The other cylindrical tank with flanges (packing volume and inner diameter of 96.2 mL and 35 mm, respectively) (Figure 3.3(B)) was densely filled with two beds of MgH_2-TiF_4-AC powder (67.018 g and ~33.5 g/bed) separated by round-shaped stainless steel (SS) mesh sheets (SS304, No. 120). To improve hydrogen permeability, the number of MgH_2-TiF_4-AC beds was increased from two to four (60.551 g and ~15 g/bed) together with the insertion of SS mesh tube at the tank center.

(A) (B) (C)

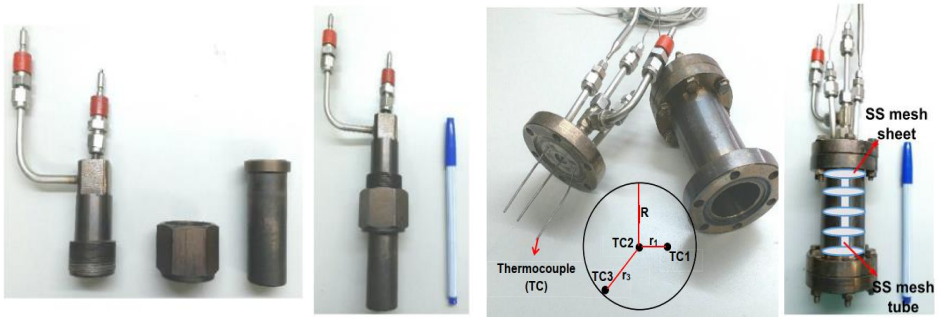

Figure 3.3 Hydrogen storage tanks with packing volumes of 28.8 mL (A), 96.2 mL (B) with the positions of temperature sensors (TCs) along the tank radius, and four hydride beds with SS mesh tube at the tank center (C).

3.1.1.2 MgH_2 doped with NbF_5 and MWCNT

Mg powder (grain size of 50–150 mesh, ≥99.0%, Sigma Aldrich) was hydrogenated at 350 °C under 10–15 bar H_2 for 12 h and milled for 10 h using the BPR and rotational regime of 10:1 and 500 rpm, respectively using a QM0.4L Planetary Ball Mill, Nanjing Chishun Science & Technology. The as-obtained powder sample was milled with 5 wt. % NbF_5 (98%, Sigma-Aldrich) for 3 h using the BPR of 10:1 and hydrogenated at 350 °C under 10–15 bar H_2 for 12 h. The powder sample was repeatedly milled and hydrogenated three times using similar temperature, pressure, time, and milling conditions to obtain the as-prepared MgH_2-5 wt. % NbF_5. Multi-walled carbon nanotube (MWCNTs, tube diameter = 12 nm, Nano Generation Co., Ltd. Thailand) was treated at 500 °C under vacuum for 3 h and milled (5 and 10 wt. % MWCNTs) with the as prepared MgH_2-5 wt. % NbF_5 for 30 min using the BPR of 10:1 to obtained MgH_2–NbF_5-MWCNTs samples, denoted as MgH_2-NbF_5-5%CNT and MgH_2-NbF_5-10%CNT for the samples containing 5 and 10 wt. % MWCNTs, respectively.

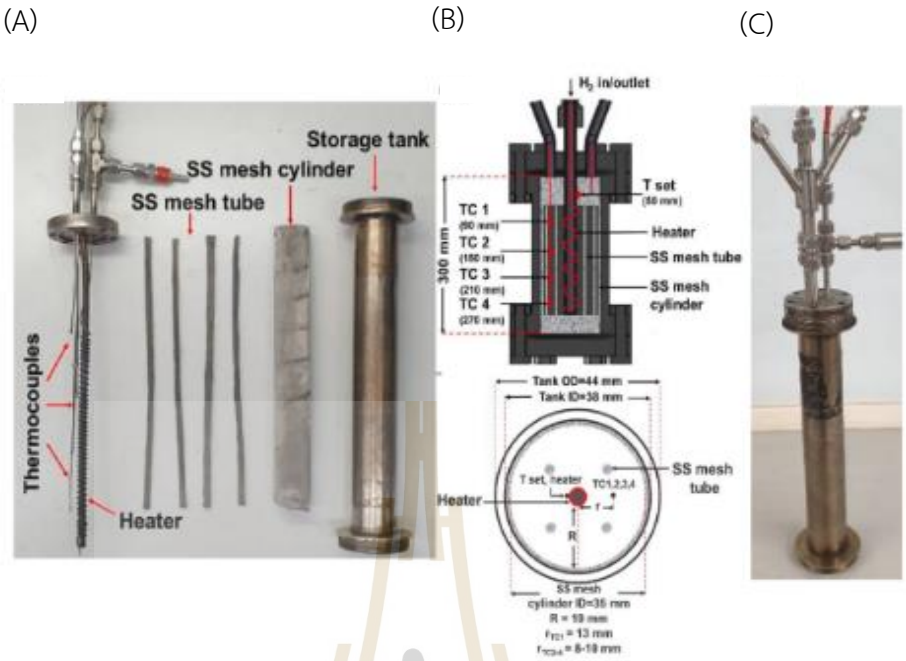

Figure 3.4 The component of hydrogen storage tank (A), the position of thermocouples in the radial and axial directions (B) and the assembled hydrogen tank (C).

The powder samples of MgH_2-NbF_5-5%CNT and MgH_2-NbF_5-10%CNT (76.3002 and 71.6518 g, respectively) were packed tightly into a SS mesh cylinder (SS304, No. 120) and placed inside a storage tank with a packing volume of 337.40 mL (Figure 3.4(A)). The tank cover was mounted with the H_2 inlet/outlet tube, central heater, and K type thermocouples (TCs, –250 to 1300 °C, SL heater). Four SS mesh tubes were inserted in the powder sample at the locations shown in Figure 3.4(B). Four TCs (TC1-TC4) were located at 8–13 and 90–270 mm in the radial and axial directions, respectively. The setting temperature for each measurement was controlled by another TC (T_{set}) placed adjacent to the central heater (Figure 3.4(B)). The powder sample packed in the SS mesh cylinder and all components of the tank were assembled to form the MgH_2-NbF_5-5%CNT and MgH_2-NbF_5-10%CNT tanks (Figure 3.4(C)).

3.1.2 MgH_2-based thermal storage materials

Mg powder (≥99.0%, Aldrich) was hydrogenated at 350 °C under 40 bar H_2 for 12 h and milled for 5 h with the BPR and a rotational regime of 10:1 and 500 rpm, respectively using a Retch PM100 planetary ball mill (Figure 3.2(B)). As-prepared MgH_2

was milled using BPR of 10:1 with 5 wt. % Nb_2O_5 for 20 h and with 5 wt. % graphite for 30 min to obtain MgH_2-5 wt. % Nb_2O_5-5 wt. % graphite. Hydrogenation was repeated by pressurizing 40 bar H_2 on MgH_2-Nb_2O_5-graphite at 350 °C for 12 h**.** To obtain MgH_2-Nb_2O_5-graphite used as high-temperature metal hydride, denoted as HTMH. As-received $LaNi_5$ alloy (hydrogen storage grade, Whole Win Materials Sci. & Tech. Co. Ltd., Beijing) was activated at room temperature (25–27 °C) by hydrogenating under 40 bar H_2 and dehydrogenating under vacuum for several cycles. The activated $LaNi_5$ alloy was used as low-temperature metal hydride, denoted as LTMH.

The weight ratio of HTMH:LTMH for the coupled MgH_2–$LaNi_5$ thermal storage system was 1:6. The powder samples of HTMH (40 g) and LTMH (240 g) were packed tightly into the SS mesh cylinders (SS304, No. 120) and placed into the storage tanks with the packing volumes of 96.2 mL mounted with double tube heat exchanger for both HTMH and LTMH (Figure 3.5). In HTMH tank, four thermocouples (TC1-TC4) were placed in the powder beds in the axial direction of the tank (Figure 3.5(A)) to measure the sample temperatures during heat charging and discharging reaction. Round-shaped SS mesh were inserted into the tank to enhance hydrogen diffusion. The similar method and design of packing was use for LTMH tank, but only three thermocouples were used (TC1-TC3) (Figure 3.5(B)).

(A)

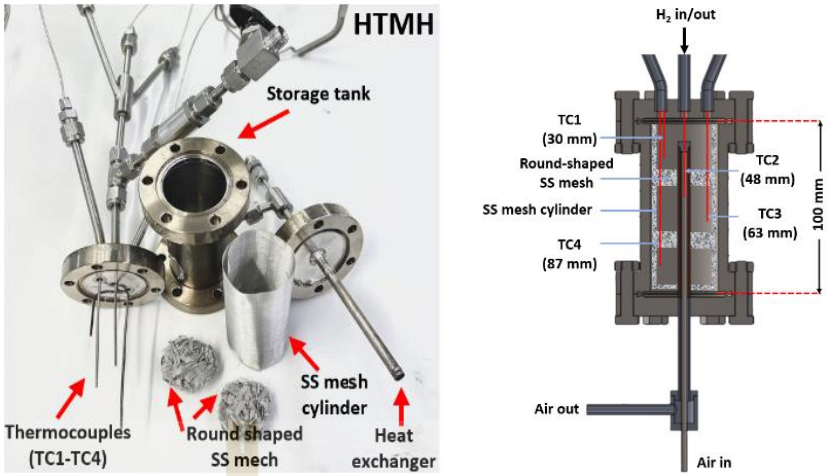

(B)

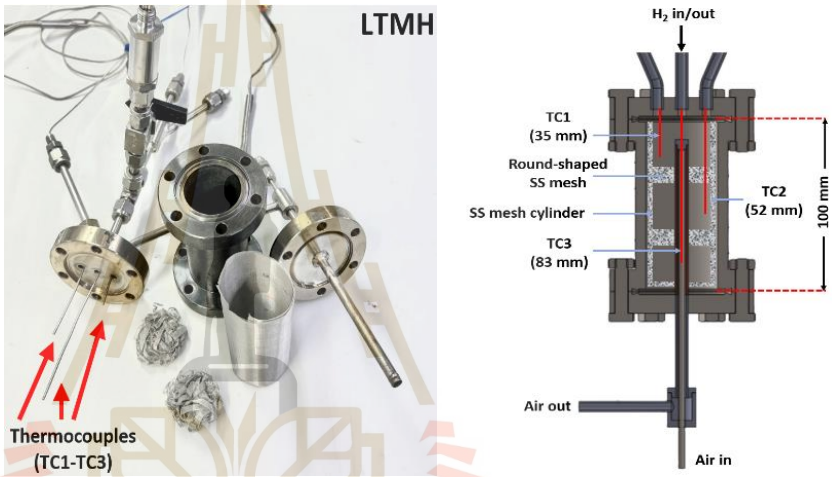

Figure 3.5 The components and schematic diagrams of the cylindrical containers for HTMH (A) and LTMH (B).

3.2 Characterizations

3.2.1 Powder X-ray diffraction (PXD)

Powder x-ray diffraction (PXD) was carried out using a Bruker D2 PHASER with Cu K_α radiation (λ=1.5406 Å). The powder sample was packed in an airtight sample holder covered with a poly(methyl methacrylate)(PMMA) dome (Figure 3.6) in the N_2-filled glove box to prevent oxygen and humidity. The diffractograms were collected in the 2θ range of 10-80 ° using the scanning steps and acquisition time of 0.02 ° /s and 400 s/step, respectively.

Figure 3.6 An airtight PXD sample holder covered with PMMA dome.

3.2.2 Simultaneous differential scanning calorimetry (DSC)-thermogravimetry (TG)-mass spectrometry (MS)

Simultaneous differential scanning calorimetry (DSC)-thermogravimetry (TG) measurements were performed using a Netzsch STA449F3 Jupiter (Figure 3.7). The powder sample (10-15 mg) was heated from room temperature to 500 °C (5 °C /min) under N_2 flow of 50 mL/min. The relative signal of hydrogen was simultaneously detected by a Netzsch QMS 403C mass spectrometer (MS).

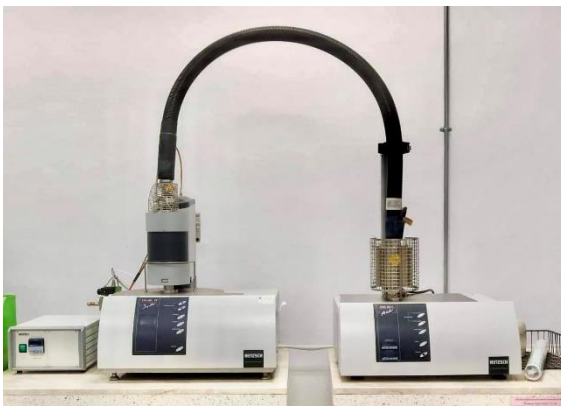

Figure 3.7 Simultaneous DSC-TG-MS.

3.2.3 Sievert type apparatus

De/rehydrogenation kinetics of MgH_2-based in laboratory and tank scales were studied using a test station controlled by the program developed in LabVIEW® (Figure 3.8). Pressure transducers with operating pressure ranges of 0–1500 and 0–3000 Psig (PX409-1.5KGI and PX309-3KGI, OMEGA Engineering) were used to measure the system pressure during the experiments. Hydrogen gas applied to and released from the system was controlled using the direct-acting plunger solenoid valves (Type 0255, Bürkert). A mass flow controller (MFC, a Bronkhorst EL-FLOW selected F–201CV) with an operating flow rate of 0–2 standard L/min (SLM) at the standard temperature (T_s) and pressure (P_s) of 294.15 K and 1.0085 bar, respectively was used to measure the hydrogen released during dehydrogenation. The temperature, pressure, and mass flow rate signals were transferred to the computer using module data loggers (NI USB-6009, National Instruments and AI210, Wisco). Hydrogenation of MgH_2-TiF_4-AC was done under isothermal condition at setting temperature (T_{set}) of 250 and 300 °C under 10-20 bar H_2. Dehydrogenation was carried out at T_{set} 300 °C under ~1 bar H_2.

For MgH_2–NbF_5-MWCNTs, hydrogenation was carried out at T_{set} = 250 °C under 10–15 bar H_2, while dehydrogenation was performed at T_{set} = 300 °C with the initial pressure of ~15 bar H_2, remaining from the previous hydrogenation. The volume of hydrogen gas released from the tank was calculated by integrating the area of the hydrogen flow rate (SLM) versus time (min) plot. The total hydrogen storage capacity,

which was the combination of material storage capacity and hydrogen content remaining from the hydrogenation was calculated using the following equations.

$$V_{STP} = \frac{P_s V_s T_{STP}}{T_s P_{STP}} \tag{3.1}$$

$$n_{H_2} = \frac{V_{STP}}{22.4\ \text{L/mol}} \tag{3.2}$$

$$H_2\ \text{capacity (wt. \%)} = \frac{n_{H_2} \times 2.016\ \text{g/mol}}{\text{sample weight}} \times 100 \tag{3.3}$$

where V_{STP} (L) and V_s (SL) are the volumes of hydrogen gas under the standard temperature and pressure conditions (T_{STP} = 273.15 K, and P_{STP} = 1.0133 bar) and under the standard condition of the MFC, respectively. n_{H_2} (mol) is the number of moles of hydrogen and the standard molar volume is 22.4 L/mol.

(A) (B)

Figure 3.8 Sievert type apparatus test station in laboratory (A) and tank (B) scales.

3.2.4 Coupled HTMH-LTMH for thermal storage

The laboratory test station (Thiangviriya, Thongtan, Thaweelap, Plerdsranoy, & Utke, 2024) (Figure 3.9) was employed to investigate the heat charging and discharging performance as well as cycling stability of the coupled MgH_2–$LaNi_5$ thermal storage system. K-type thermocouples and pressure transmitters (Kistler) were used to monitor the temperature and pressures, respectively, inside HTMH and LTMH tanks. Temperature and pressure signals were transferred to the computer using data

loggers (National Instruments NI USB-6009 and Wisco AI210). Direct-acting plunger solenoid valves and an electric actuator 3-way ball valve were used to control the hydrogen flow direction between HTMH and LTMH during heat charging and discharging. Activation involved heating HTMH to T_{set} = 370 °C under 0.2 bar H_2. Heat discharging of HTMH began with heating LTMH to T_{set} = 50 °C and switching off the HTMH heater. Meanwhile, the hydrogen flow direction was assigned as LTMH⟶HTMH. Compressed air at room temperature (~10 L/min) applied through a mass flow meter (FMA-4000, an OMEGA Engineering) was used as the heat transfer fluid (HTF) during charging and discharging. At T_{set} = 200 °C, heat charging was done by heating HTMH to T_{set} = 370 °C and cooling LTMH to room temperature as well as changing hydrogen flow direction to HTMH⟶LTMH. Hydrogen flows between HTMH and LTMH was measured using a mass flow meter (FMA-767A, OMEGA Engineering 0-1000 SCCM). The number of hydrogen moles and capacities were calculated by integrating the peak area of the hydrogen flow rate (SCCM) versus time (min) plot and equations (3.1)–(3.3).

(A) (B)

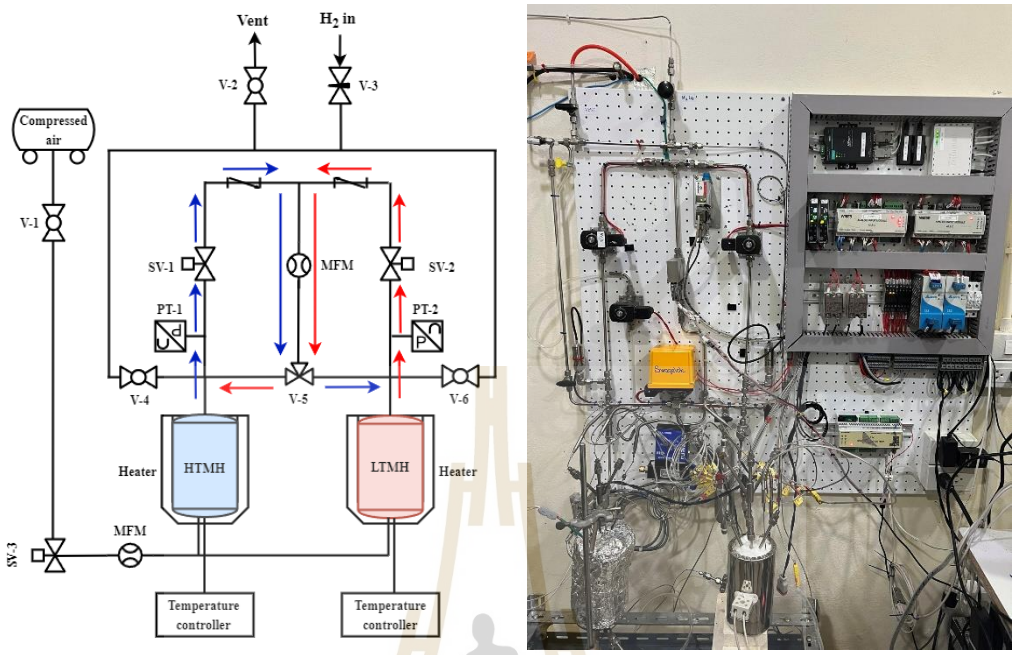

Figure 3.9 Schematic diagram (A) and photo (B) of the test station for investigating heat charging and discharging performances and cycling stability (SV1-3 = solenoid valve, V1-2 and V4-6 = ball valve, V3 = needle valve, MFM = mass flow meter, PT1-2 = pressure transmitters (0.50 and 0.35), HTMH/LTMH = high/low temperature metal hydride).

3.3 References

Thiangviriya, S., Thongtan, P., Thaweelap, N., Plerdsranoy, P., and Utke, R. (2024). Heat charging and discharging of coupled MgH_2–$LaNi_5$ based thermal storage: Cycling stability and hydrogen exchange reactions. *International Journal of Hydrogen Energy*, *49*, 59–66. https://doi.org/10.1016/J.IJHYDENE.2023.10.312

CHAPTER IV

RESULTS AND DISCUSSION

4.1 MgH_2-based hydrogen storages

4.1.1 Hydrogen storage and performances of MgH_2-TiF_4-AC-based tank

The chemical composition of as-prepared sample was characterized using Powder x-ray diffraction (PXD) technique. PXD pattern is dominated by diffraction peaks of MgH_2 with slight content of Mg (Figure 4.1), indicating successful hydrogenation during sample preparation.

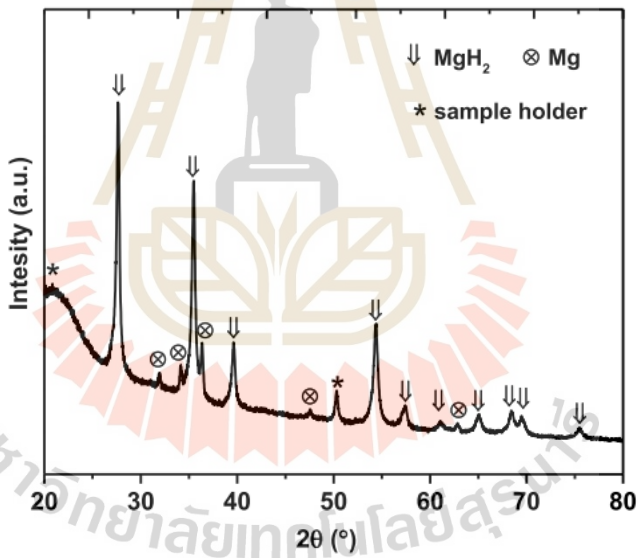

Figure 4.1 PXD spectrum of MgH_2-TiF_4-AC.

Dehydrogenation profiles of as-prepared MgH_2-TiF_4-AC were studied by simultaneous DSC-TG-MS. From Figure 4.2, the DSC curve of as-received MgH_2 shows onset and main endothermic peaks at 410 and 433 °C, respectively, approaching to previous reports (Sulaiman and Ismail, 2016; Thaweelap et al., 2017). Meanwhile, onset and main endothermic peak of MgH_2-TiF_4-AC are at 272 and 324 °C, respectively. Onset and main decomposition temperatures of MgH_2 reduce by 138 and 109 °C, respectively, corresponding to the results of MgH_2 doped with other transition metal-

based additives (Ma et al., 2011; Malka, Pisarek, Czujko, and Bystrzycki, 2011; Mustafa and Ismail, 2017; Wang, Wang, Zhang, Jiao, and Yuan, 2015; Yu, Bennici, and Auroux, 2014) and carbon materials (Chaise et al., 2009; Lillo-Ródenas, Guo, Aguey-Zinsou, Cazorla-Amorós, and Linares-Solano, 2008; J. Zhang et al., 2015). TGA and H_2-MS results of both samples reveal single-steps dehydrogenation with 6.4 and 4.4 wt. % H_2 for as-received MgH_2 and MgH_2-TiF_4-AC, respectively. Considering 10 wt. % of non-hydride additives, theoretical capacity of MgH_2-TiF_4-AC is 6.8 wt. % H_2 (theoretical hydrogen storage capacity of MgH_2 = 7.6 wt. % H_2). TG thermogram in Figure 4.2 shows 4.4 wt. % H_2 released from MgH_2-TiF_4-AC, Deficient hydrogen content released from MgH_2-TiF_4-AC can be due to incomplete hydrogenation of Mg to MgH_2, in accordance with the diffraction peaks of residual Mg in as-prepared MgH_2-TiF_4-AC (Figure 4.1).

Afterwards, dehydrogenation kinetics of MgH_2-TiF_4-AC based small hydrogen storage tank is investigated. During dehydrogenation, MgH_2-TiF_4-AC tank is heated to 300 °C (T_{set}) the initial pressure (P_{in}) of 5.0 bar is assigned to obtain the proper flow rate in the operating range of MFM. From Figure 4.3(A), hydrogen pressure of MgH_2-TiF_4-AC tank reaches P_{in} (5.0 bar) at 283 °C which is slightly higher than onset dehydrogenation temperature of MgH_2-TiF_4-AC powder (272 °C) obtained from STA thermogram (Figure 4.2). During dehydrogenation, continuous hydrogen gas liberation occurs at the flow rate of 0.06-0.8 SLM through MFM with an outlet pressure of 1 bar (atmospheric pressure). The system pressure steadily decreases from 5 to 1.6 bar. Dehydrogenation ends after 70 min due to slow kinetics demonstrated as a constant flow rate of 0.06 SLM for 15 min (Figure 4.3(A)). Considering the peak area of the plot between hydrogen flow rate (SLM) and time (min), hydrogen gas volume is 6.13 SL, yielding hydrogen storage capacity of 3.54 wt. %. H_2. To confirm successful dehydrogenation of MgH_2-TiF_4-AC tank, dehydrogenated samples collected at the top, middle, and bottom positions of the tank (Figure 4.3(B)) are characterized by PXD technique. Diffraction patterns of Mg, MgH_2, and MgF_2 are observed at the bottom and middle position, while those of Mg and MgH_2 are found at the top position (Figure 4.3(C)).

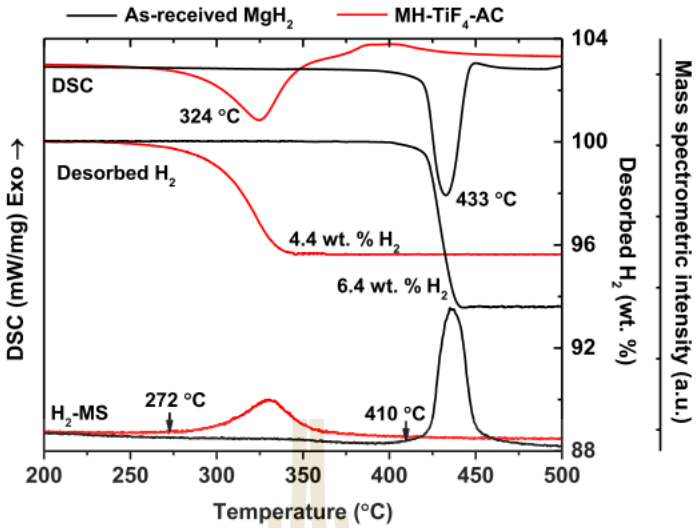

Figure 4.2 Simultaneous DSC-TG-MS thermogram of MgH_2-TiF_4-AC and as-received MgH_2.

Although dehydrogenation of MgH_2-TiF_4-AC can proceed confirmed by the formations of Mg and MgF_2, residual MgH_2 suggests incomplete dehydrogenation. This corresponds to deficient hydrogen content released of 3.54 wt. % H_2 (Figure 4.3(A)) with respect to 4.4 wt. % H_2 detected by TG thermogram (Figure 4.2). It should be noticed that the bottom and middle positions have high relative content of Mg to MgH_2 and the creation of MgF_2 indicates successful dehydrogenation. This could be attributed to the fact that the middle and bottom positions of the tank are completely inside the furnace, which homogeneous heat transfer can be achieved. During dehydrogenation, the system pressure of 1.6 bar H_2 (Figure 4.3(A)), which is higher than the equilibrium pressure of MgH_2 at 300 °C (1 bar H_2) (Bogdanović, Ritter, and Spliethoff, 1990; Felderhoff and Bogdanović, 2009) probably suppresses dehydrogenation.

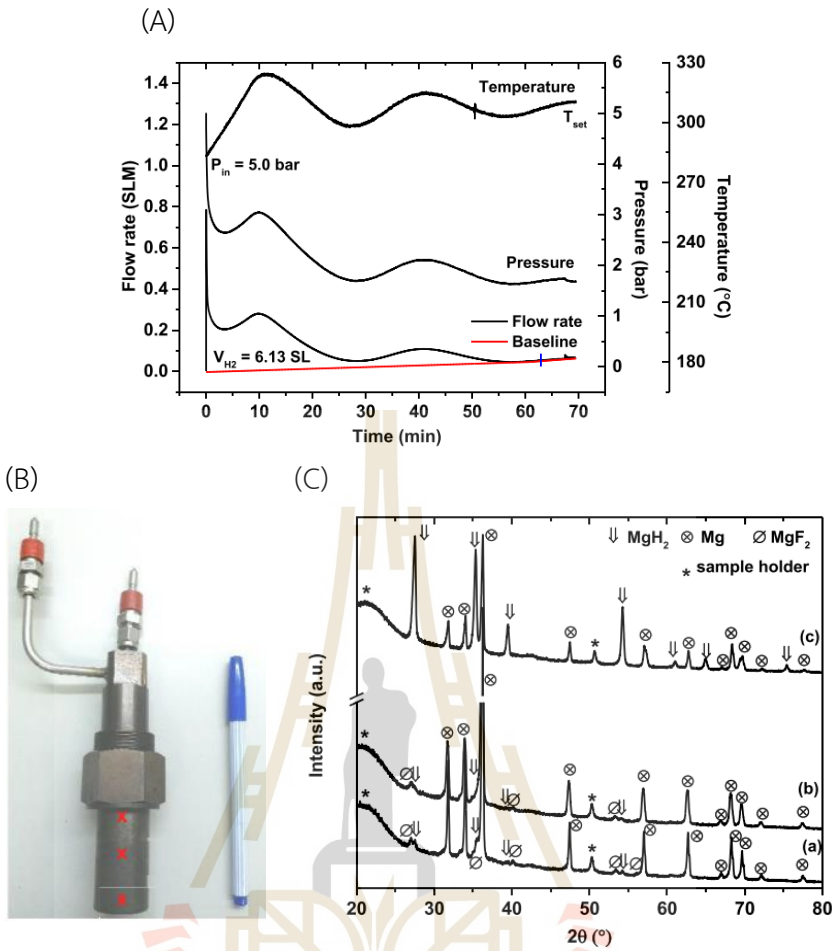

Figure 4.3 Dehydrogenation (T_{set} = 300 °C and P(H_2) = 1 bar) of MgH_2-TiF_4-AC tank (28.8 mL) (A), the positions of TC (B), and PXD spectra of the dehydrogenated samples at the bottom (a), middle (b), and top (c) positions of the tank (C).

Furthermore, the packing volume of the hydrogen storage tank and the quantity of MgH_2-TiF_4-AC are enhanced to 96.2 mL and 67.018 g, respectively (Figure 4.4(A)). To investigate heat transfer inside the MgH_2-TiF_4-AC tank, three K-type thermocouples (TC1, TC2, and TC3) are strategically placed at different in the radial direction of the tank (r/R = 0.43, 0, and 0.91, respectively (Figure 4.4). All thermocouples are located approximately at the middle position of the tank to facilitate comprehensive analyses. To enhance hydrogen permeability and heat transfer, MgH_2-TiF_4-AC powder sample is arranged to pack into the twin beds divided by circular SS mesh sheets (Figure 4.4(A)). By heating MgH_2-TiF_4-AC tank to T_{set} ~220

°C, the system pressure increases slightly from 1.16 to 1.24 bar due to heat expansion (grey frame (a) in Figure 4.4(B)). At T_{set} = 225-275 °C (grey frame (b) in Figure 4.4(B)), considerable reduction of the system pressure (from 1.24 to 0.6 bar) suggests hydrogenation of residual Mg, corresponding to diffraction peaks of Mg found in PXD spectra of as-prepared MgH_2-TiF_4-AC (Figure 4.1). As the pressure approaches 0.6 bar, approaching the equilibrium pressure of MgH_2 at 275 °C, the hydrogenation process terminates.

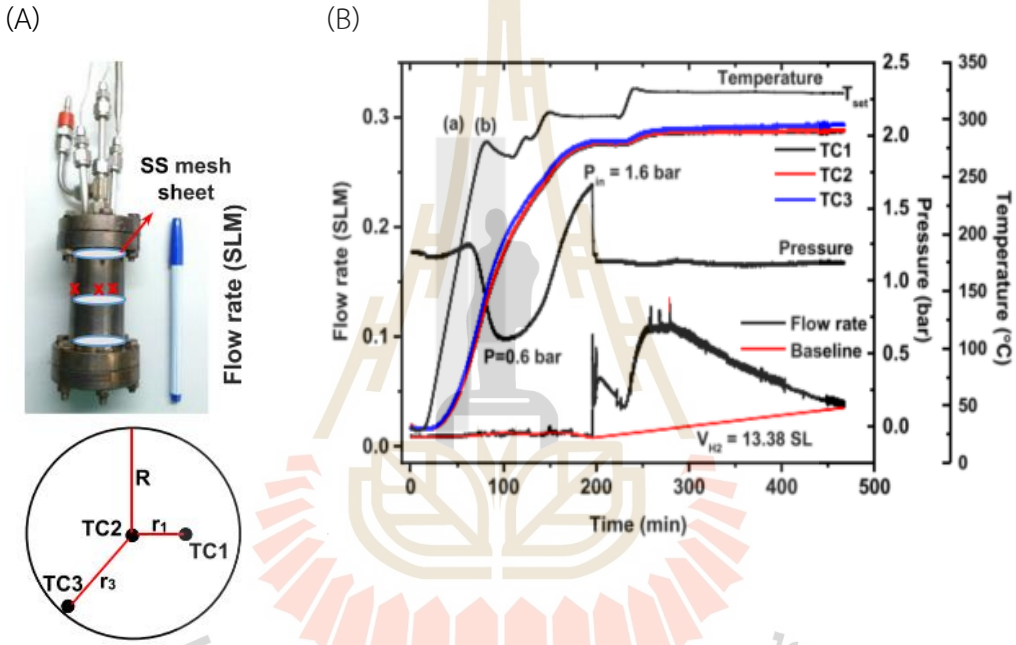

Figure 4.4 Dehydrogenation (T_{set} = 300 °C and $P(H_2)$ = 1 bar) of MgH_2-TiF_4-AC tank (96.2 mL).

To overcome thermodynamic restriction and improve kinetic properties, T_{set} is increased to 300-325 °C. Dehydrogenation is observed by significant enhancement of hydrogen pressure to 1.6 bar (P_{in} in Figure 4.4(B)). Approximately 13.38 SL of H_2 (1.67 wt. % H_2) release from the MgH_2-TiF_4-AC tank within ~ 250 min. Temperatures detected by all TCs are approximately identical, suggesting uniform dehydrogenation performance and effective thermal conductivity along the tank's radius (17.5 mm). Slightly elevated temperature observed at TC3 with respect to other TCs can be due to the fact that TC3 is adjacent to the heater (tank wall). Previous studies have indicated the preference for elongated metal hydride tanks with smaller diameters

due to reduced heat transfer distances and enhanced heat dissipation compared to wider tanks (Lototskyy et al., 2017). However, the hydrogen content released from the MgH_2-TiF_4-AC tank (1.67 wt. % H_2) is lower than 4.4 wt. % H_2 observed from TG thermogram (Figure 4.2). This indicates incomplete dehydrogenation probably due to poor hydrogen permeability inside the tightly packed powder sample, especially at the tank center.

To address the enhancement of hydrogen permeability within the MgH_2-TiF_4-AC tank, the dehydrogenated powder sample of MgH_2-TiF_4-AC from Figure 4.4 is unpacked and milled for 30 min with BPR of 20:1. The milled sample is divided into four beds separated by round-shaped ss mesh sheets together with the insertion of ss mesh tube at the tank center (Figure 4.5(A)). Hydrogenation is carried out at isothermal condition (T_{set} ~ 300 °C) under automatically controlled hydrogen pressure of 15-20 bar (Figure 4.5(B)). At the initial state, all TCs show temperature of 296.5 °C, suggesting homogeneous heat distribution along the tank radius. By pressurization of ~17 bar H_2, temperature of the powder sample at TC3 increases considerably to 377 °C together with slight reduction of the system pressure (grey frame in Figure 4.5(B)), indicating rapid hydrogenation due to the pressure applied greater than the equilibrium pressure. However, temperatures of sample at the positions close to the tank center (TC1 and TC2) significantly decrease to 185 and 265 °C, respectively, hinting at dehydrogenation of MgH_2-TiF_4-AC. Despite hydrogenation progressing at TC3, the system pressure stabilizes at 16-17 bar H_2 for roughly 30 min due to ongoing dehydrogenation at TC1 and TC2 (grey frame in Figure 4.5(B)). This phenomenon can be probably due to the fact that progressive hydrogenation at TC3, leading to quick reduction of the system pressure is a driving potential for dehydrogenation at TC1 and TC2. Superior dehydrogenation observed at the tank center (r/R = 0) can be explained by the efficient hydrogen permeability facilitated by the insertion of the SS mesh tube.

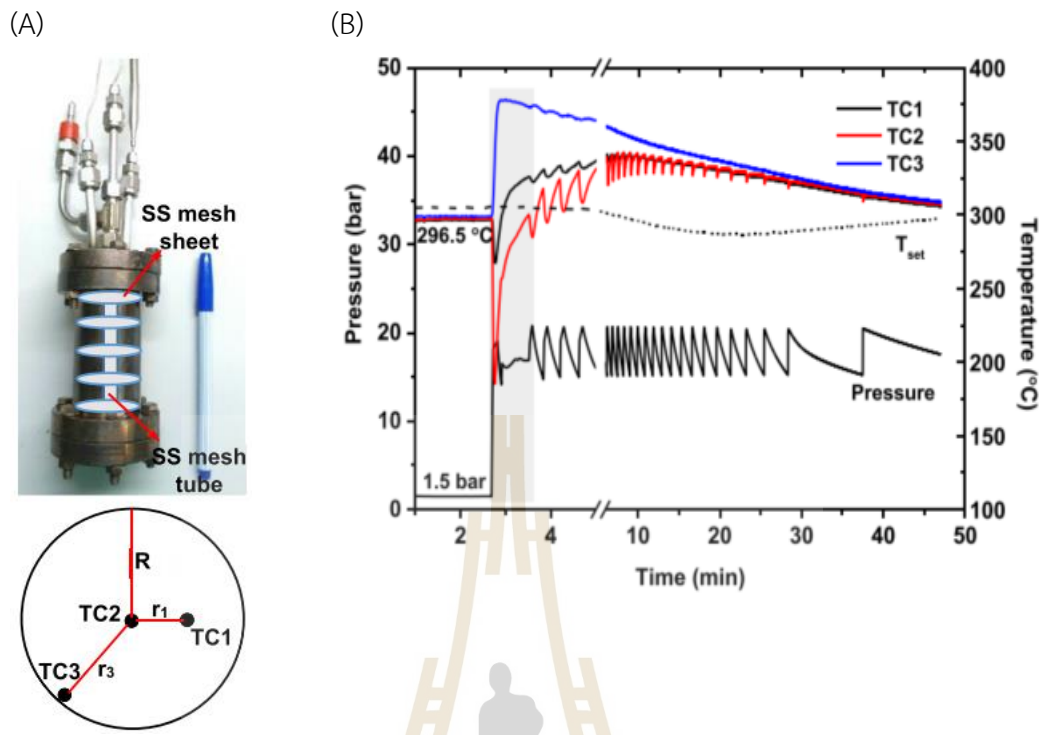

Figure 4.5 Hydrogenation (T_{set} = 250 °C and $P(H_2)$ = 15-20 bar) of MgH_2-TiF_4-AC tank (packing volume of 96.2 mL).

Afterwards, temperatures at TC2 and TC1 gradually increase to the maximum temperatures of 296.5 and 325 °C, respectively. This indicates that dehydrogenation is nearly complete. Hydrogenation proceeds at all positions and completes after 48 min confirmed by the reduction of temperatures at all TCs to the initial temperature (296.5 °C) (Figure 4.5(B)). This hydrogenated sample is designated as the as-prepared sample for a further 15 hydrogen release and uptake cycles.

Dehydrogenation conditions including T_{set} and P_{in} for MgH_2-TiF_4-AC tank are at 300 °C and 1.4 bar H_2, respectively. Since onset dehydrogenation temperature of MgH_2-TiF_4-AC is at 272 °C (Figure 4.2), a pre-cooling step to 250 °C is done prior to dehydrogenation to prevent undesired decomposition. Upon heating to T_{set} 300 °C, temperatures recorded at all TCs rise at comparable rate (Figure 4.6(A)). At temperature approaching onset dehydrogenation of MgH_2-TiF_4-AC (275-283 °C), the system pressure enhances sharply and reaches P_{in} within 15 min, implying fast kinetics of MgH_2-TiF_4-AC tank and comparable performance with laboratory scale. During

dehydrogenation, the steady state of system pressure at 1.03 bar (slightly higher than the outlet pressure of ~1 bar) drives hydrogen gas flow through MFM (Figure 4.6(A)). Within 3.5 h, the MgH_2-TiF_4-AC tank releases 32.3 SL of H_2 in two steps, in accordance with gravimetric and volumetric capacities of 4.46 wt. % H_2 and 28 gH_2/L, respectively. It should be mentioned that the MgH_2-TiF_4-AC tank demonstrates superior volumetric hydrogen capacity compared to high-pressure compressed hydrogen tanks fabricated from steel cylinders at 200 bar and type IV composite cylinders at 700 bar, offering 9 and 23 gH_2/L, respectively (Klell, 2010). Further enhancement of hydrogen capacity by compaction of MgH_2 based materials and assembly of heat exchanger to the tank is in progress. During dehydrogenation, the plateau temperatures at 295, 300, and 307 °C (TC1-TC3) are detected (Figure 4.6(A). Regarding good heat transfer along the tank radius (Figure 4.4 and Figure 4.5), the enhancement of plateau temperature toward the tank wall (r/R ratio from 0 to 0.43 and 0.91) can be explained by poor diffusion of hydrogen desorbed (Garrier et al., 2011). Although the insertion of the SS mesh tube at the tank center results in superior hydrogen permeability at r/R = 0, the permeability gradually decreases with increasing r/R ratios. Moreover, the plateau temperature range, suggesting continuous release of hydrogen is considerably prolonged at r/R = 0 and decays with enhancing r/R to 0.43 and 0.91. Early in the first step (within 30 min after P_{in}), high hydrogen flow rate of up to 0.52 SLM corresponds to simultaneous dehydrogenation at all positions, consistent with the observed plateau temperatures.

(A)

(B)

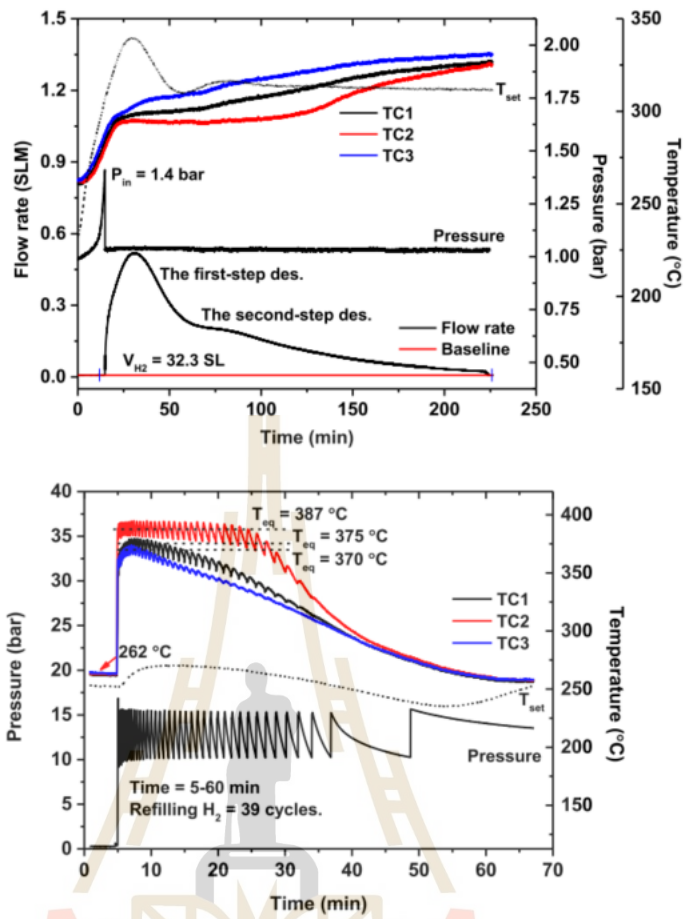

Figure 4.6 Dehydrogenation (T_{set} = 300 °C and P(H_2) = 1 bar) (A) and hydrogenation (T_{set}= 250 °C and P(H_2) = 10-15 bar) (B) during the 1st cycle of MgH_2-TiF_4-AC tank.

After 75 min, the second step shows significant reduction of hydrogen flow rate to ~0.2 SLM. This possibly attributes to hydrogen release mainly from r/R = 0 position, where plateau temperature continues (Figure 4.6(A)). The dehydrogenation process ends once temperatures at all positions reach and stabilize at the same set point around 325 °C.

Rehydrogenation is done into the tank, at T_{set} = 250 °C under 10-15 bar H_2. Before introducing hydrogen, similar temperatures (262 °C) are recorded at all thermocouples (Figure 4.6(B)), suggesting good heat transfer within the sample. Upon pressurization, temperatures rapidly rise to equilibrium values at 370-387 °C, indicating fast hydrogenation with low heat transfer. High refilling rate of hydrogen gas to maintain hydrogenation pressure in the range of 10-15 bar H_2 during the first 5 min implies effective hydrogenation at all positions (Figure 4.6(B). After 10 min, slower hydrogen refilling rate (i.e., hydrogenation) is observed at r/R = 0.43 and 0.91. Thereafter,

temperatures at all r/R ratios decrease to the initial values at 262 °C within 60 min together with significantly slow hydrogen refilling rate, implying end of hydrogenation. Hydrogen refilling for hydrogenation during 5-60 min is totally 39 cycles (Figure 4.6(B)). Short plateau temperature ranges detected at r/R = 0.43 and 0.91 with respect to that of r/R = 0 can be explained by either fast hydrogenation kinetics or limitation of hydrogenation due to poor hydrogen permeability.

Interestingly, despite similar heat transfer across the tank radius, different equilibrium temperatures are found at 387, 375, and 370 °C for r/R = 0, 0.43, and 0.91, respectively. These equilibrium temperatures correspond to the equilibrium pressures of 12.4, 9.8, and 8.4 bar H_2, respectively (Chaise, De Rango, Marty, and Fruchart, 2010). Notably, the equilibrium pressure at r/R = 0 (12.4 bar H_2) matches the applied hydrogen pressure (10-15 bar H_2), while those at other positions are lower. This implies poor hydrogen permeability and limited hydrogenation towards the tank wall. Therefore, the de/rehydrogenation performance of the MgH_2-TiF_4-AC tank is superior at the center and deteriorates towards the tank wall. Further examination of de/rehydrogenation stability upon 15 cycles is studied (T_{set} = 300 °C and P_{in} = 1.4 bar H_2 for dehydrogenation and T_{set} = 250 °C and $P(H_2)$ = 10-15 bar H_2 for hydrogenation). Form Figure 4.7, hydrogen content released during the 1st-2nd cycles are comparable of 4.46 wt. % H_2 (28 gH_2/L), while those during the 3rd-15th cycles reduce to the stabilized values of 3.42-3.62 wt. % H_2 (22-23 gH_2/L). To explain the inferior hydrogen content reproduced, the chemical compositions and physical appearance of the sample after cycling are taken into account.

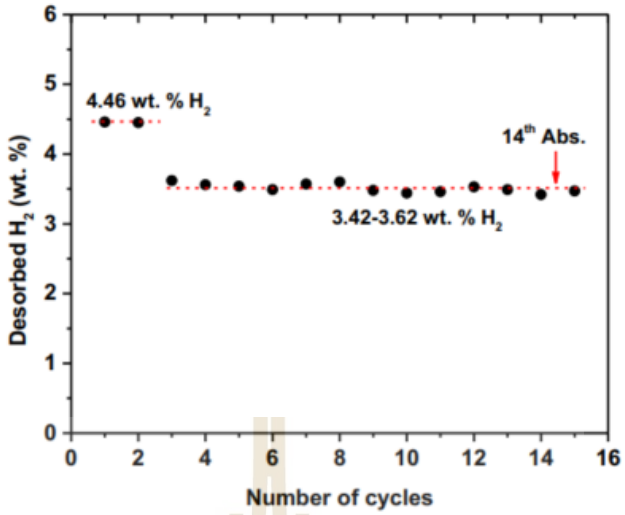

Figure 4.7 Hydrogen contents released and reproduced upon 15 cycles of MgH_2-TiF_4-AC tank.

Prior to hydrogen pressurization, all TCs show similar set-point temperatures at 255 °C (Figure 4.8(A)), indicating uniform heat distribution across the tank radius. From Figure 4.6(B) and Figure 4.8(A), equilibrium temperatures at r/R = 0 during the 1st and 14th hydrogenations maintain consistency at 387 °C, while those at r/R = 0.43 and 0.91 decrease from 370 to 375 and 365 °C, corresponding to equilibrium pressure of ~7.5 bar H_2 (Chaise et al., 2010). Lower equilibrium pressures at r/R = 0.43 and 0.91 to the applied pressure of 10-15 bar H_2 suggest insufficient hydrogen permeability, influencing the hydrogenation performance. Comparing with the initial cycle, the 14th hydrogenation displays the shortened plateaus at all radial positions (r/R) and the reduced hydrogen refilling rate, requiring only 32 cycles instead of 39 cycles within the 5-60 min timeframe (Figure 4.8(A)). The latter hints at sluggish sorption kinetics within the MgH_2-TiF_4-AC tank, contributing to the decreased hydrogen content observed after repeated cycling (Figure 4.7).

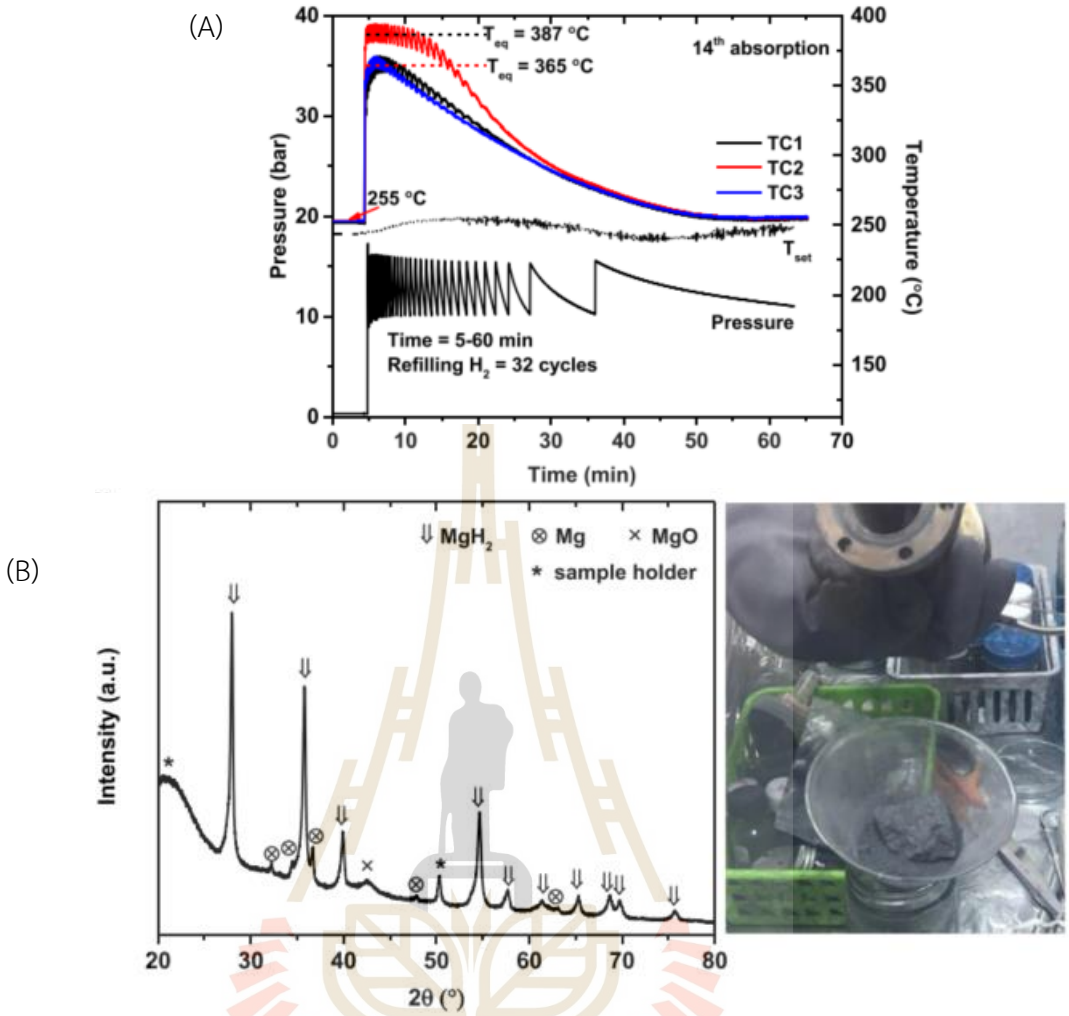

Figure 4.8 The 14th hydrogenation (T_{set} = 250 °C and P (H_2) = 10-15 bar) of MgH_2-TiF_4-AC tank (A) as well as PXD spectrum and physical appearance of MgH_2-TiF_4-AC after the 15th hydrogenation (B).

Moreover, the chemical compositions of MgH_2-TiF_4-AC powder are studied by PXD technique as well as physical appearance of the sample after cycling is recorded after the 15th hydrogenation. From Figure 4.8(B), the powder sample after cycling shows diffraction peaks of Mg, MgO, and MgH_2. Although the presence of Mg indicates incomplete hydrogenation, the substantial MgH_2 content suggests significant reversibility upon cycling. Moreover, agglomeration and/or sintering of the MgH_2-TiF_4-AC powder unpacked from the tank after cycling is found (Figure 4.8(B)). These result in inferior reversibility during the 3rd-15th cycles (Figure 4.7). Therefore, the enhancement of hydrogen diffusion pathways during de/rehydrogenation is taken into

account for the new tank design. Additionally, expanding the tank length while maintaining the inner diameter increases the MgH_2 packing volume and ensures efficient heat transfer.

In conclusion, MgH_2 doped with TiF_4 and activated carbon (AC) exhibits significant reduction in dehydrogenation temperatures. Incomplete hydrogenation during sample preparation leads to the lower hydrogen capacity with respect to the theoretical values. Hydrogen content released from the MgH_2-TiF_4-AC tank shows inferior capacity due to incomplete reactions. By increasing the number of hydride beds from two to four and insertion of SS mesh tube at the tank center, hydrogen permeability is improved, leading to superior de/rehydrogenation kinetics. Gravimetric and volumetric capacities during the initial cycles are 4.46 wt. % H_2 and 28 gH_2/L, respectively. In the subsequent cycles, they maintain at 3.42-3.62 wt. % H_2 and 22-23 gH_2/L, respectively. While homogeneous heat transfer is achieved along the tank radius, hydrogen permeability decays toward the tank wall. This results in poor kinetics. Issues with particle sintering or agglomeration upon cycling lead to inferior hydrogen content.

4.1.2 Hydrogen storage and performances of MgH_2-NbF_5-CNT tank

This study focuses on the development of the hydrogen storage tank containing MgH_2 doped with NbF_5 and MWCNTs with considerably enlarged packing volume of up to 337.40 mL. The packing volume is more than three times larger than the previously work (96.20 mL) (Thiangviriya et al., 2019; Thongtan et al., 2018). NbF_5 demonstrates superior catalytic effects compared to other transition metal halides (such as TiF_4 and $ZrCl_4$) in MgH_2 dehydrogenation on a lab scale, effectively reducing activation energy and dehydrogenation temperature (Luo, Wang, Ma, and Cheng, 2008; Plerdsranoy et al., 2019), while MWCNTs were beneficial to the thermal conductivity and hydrogen diffusion inside the bulk hydride. The powder sample is packed tightly into the tank assembled with SS mesh tubes to enhance hydrogen diffusion during the de/rehydrogenation process. The effects of the MWCNTs content (5–10 wt. %) on the de/rehydrogenation kinetics and mechanism at different positions in the tank as well as the reversibility are investigated.

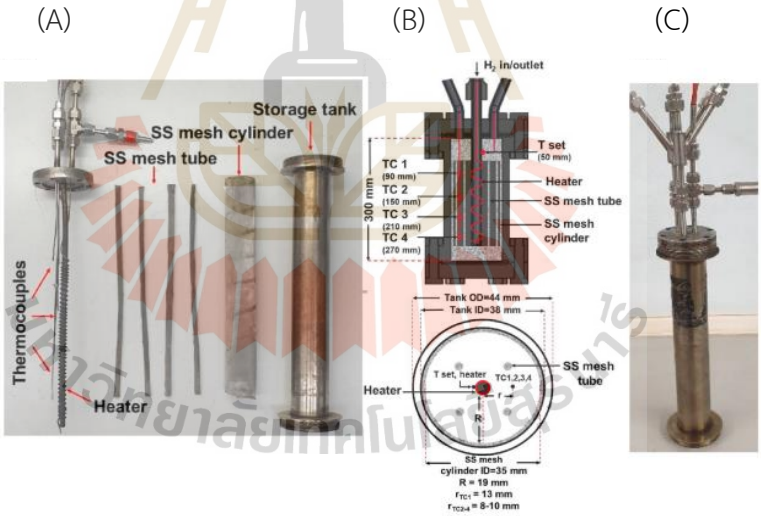

Figure 4.9 The components of hydrogen storage tank (A), the positions of thermocouples in the radial and axial directions (B) and the assembled hydrogen storage tank (C).

The de/rehydrogenation performance and behavior at different positions of the MgH_2-NbF_5-5%CNT and MgH_2-NbF_5-10%CNT tanks are characterized. The dehydrogenation experiment (T_{set} = 300 °C) starts at an initial pressure of ~15 bar H_2, remaining from the previous absorption, while the hydrogenation is carried out by

reducing the temperature to T_{set} = 250 °C under 10–15 bar H_2. Temperature sensors (TC1–TC4) are placed at different lengths in the axial direction with comparable distances of 8–10 mm from the central heater (TC2–TC4) (Figure 4.9(B)). Since the hydrogen sorption kinetics at TC1 benefits from its location approaching the H_2 inlet/outlet, TC1 is placed slightly away from the central heater to study the performance in the radial direction (13 mm) (Figure 4.9(B)). From Figure 4.10(A), the MgH_2-NbF_5-5%CNT tank shows different initial temperatures (T_{in}) of 329–366 °C (TC2 > TC3 > TC4 > TC1). The lowest T_{in} at TC1 is likely due to the long distance in the radial direction from the central heater. Since the TC used to control the T_{set} of the heater is attached to the copper tube at the position without the heating wire (Figure 4.9(A)), the temperatures at the central heater and powder sample (T_{in}) are significantly higher than T_{set}.

When the system pressure (P_{sys}) drops below the equilibrium pressure (P_{eq}), the dehydrogenation step proceeds, evident through a consistent temperature decrease across all TCs. The initial temperatures recorded in the MgH_2-NbF_5-5%CNT tank, ranging from 329–366 °C, correspond to the P_{eq} of 4–9 bar H_2 (Jianfeng Zhang et al., 2018). After hydrogen release from the MgH_2-NbF_5-5%CNT tank until $P_{sys} < P_{eq}$, dehydrogenation begins at an onset pressure ($P_{onset\ des.}$) of 3.60 bar H_2 (Figure 4.10(A)). The endothermic dehydrogenation completes within 150 min, demonstrated by the temperature rising to ~T_{in}. The lowest temperatures across all positions are 317–332 °C, corresponding to P_{eq} of 3–4 bar H_2 (Jianfeng Zhang et al., 2018). Due to the higher P_{eq} (3–4 bar H_2) in relation to P_{sys} (1.1 bar H_2), the dehydrogenation is encouraged. Total hydrogen volume of 27.80 SL, in accordance with the total and material hydrogen capacities of 3.03 and 2.80 wt. %, respectively, is obtained from the MgH_2-NbF_5-5%CNT tank (Figure 4.10(A)).

(A)

(B)

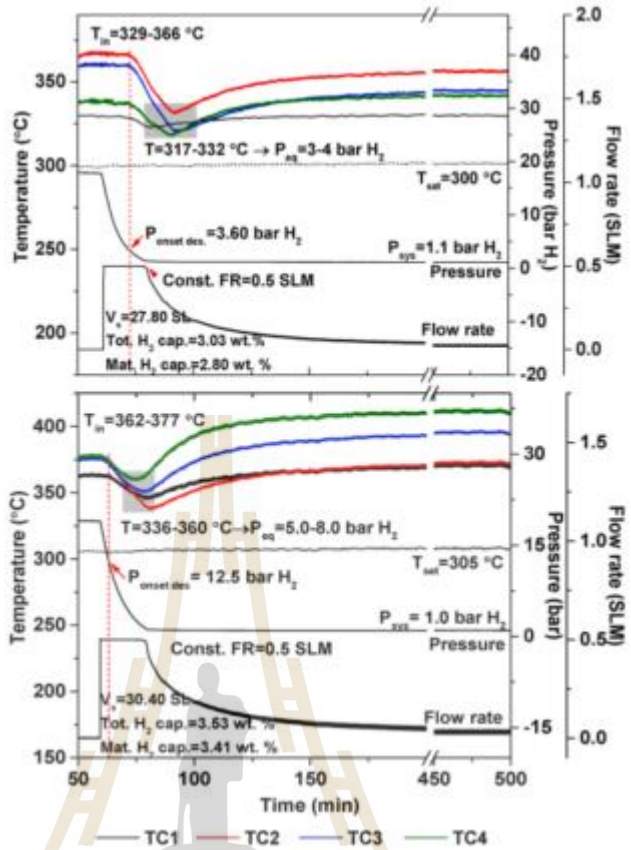

Figure 4.10 Temperatures, pressure, and hydrogen flow rate profiles during dehydrogenation of MgH_2-NbF_5-5%CNT (A) and MgH_2-NbF_5-10%CNT (B) tanks

For the MgH_2-NbF_5-10%CNT tank, temperatures at all TCs (362–377 °C) are higher as compared to those of MgH_2-NbF_5-5%CNT tank (T_{in} = 329–366 °C) at comparable T_{set} = 305 °C (Figure 4.10(B)). Additionally, T_{in} along the length of the MgH_2-NbF_5-10%CNT tank (TC2–TC4) are consistent at 377 °C. These observations imply an enhancement in the thermal conductivity of the MgH_2-based tank with the increase in MWCNTs content from 5 to 10 wt. %. (Popilevsky, Skripnyuk, Amouyal, and Rabkin, 2017; Thiangviriya et al., 2019). Desorption begins at significantly high $P_{onset\ des.}$ of 12.5 bar H_2 due to the considerable T_{in} of the MgH_2-NbF_5-10%CNT tank up to 377 °C (P_{eq} ~ 12 bar H_2 (Jianfeng Zhang et al., 2018)) (Figure 4.10(B)). Dehydrogenation reaches the lowest temperatures of 336–360 °C, corresponding to the P_{eq} of 5–8 bar H_2. These elevated P_{eq} values in comparison to P_{sys} (1.0 bar H_2) lead to complete dehydrogenation within 150 min. Total hydrogen released from the MgH_2-NbF_5-10%CNT tank is 30.40 SL, resulting in total and material hydrogen capacities of 3.53

and 3.41 wt. % H_2, respectively (Figure 4.10(B)). With comparable dehydrogenation time of 150 min and T_{set} = 300–305 °C, MgH_2-NbF_5-10%CNT demonstrates an improved material hydrogen capacity (3.41 wt. % H_2) as compared to the MgH_2-NbF_5-5%CNT (2.80 wt. % H_2). This confirms the enhanced dehydrogenation kinetics after increasing the MWCNTs content. The most effective dehydrogenation occurs at the central positions (TC2 and TC3) in both the MgH_2-NbF_5-5%CNT and MgH_2-NbF_5-10%CNT tanks. TC4, positioned at the opposite end of the hydrogen inlet/outlet exhibits sluggish desorption kinetics in the MgH_2-NbF_5-5%CNT tank, likely due to limited hydrogen diffusion and lower T_{in} with respect to the central positions (TC2–TC3) (Figure 4.10(A)). For MgH_2-NbF_5-10%CNT tank, poor kinetics at TC2-TC4 is only due to deficient hydrogen diffusion (Figure 4.10(B)). At TC1, deficient kinetics is attributed to low T_{in} observed from both tanks because of the long distance in the radial direction from the central heater (Figure 4.9(B)).

Furthermore, rehydrogenation was carried out by reducing T_{set} to 250–260 °C and increasing the pressure to 10–15 bar H_2. Due to exothermic hydrogenation, the temperatures at all positions in both tanks increase rapidly after applying the hydrogen pressure (Figure 4.11). The temperature fluctuations along the exothermic event correspond to the hydrogen refilling cycles. Under isothermal conditions (T_{set} = 250 °C) of MgH_2-NbF_5-5%CNT tank, TC2 and TC3 show short plateau temperature at 367–382 °C, in accordance with P_{eq} of 9–13 bar H_2 (Jianfeng Zhang et al., 2018) (Figure 4.11(A). For TC1 and TC4, the fast temperature reduction suggests sluggish hydrogenation process, especially at TC1. Absorption proceeding through 11 hydrogen refilling cycles is mainly observed at TC2 and TC3, and the reaction is complete within 50 min (Figure 4.11(B)).

(A)

(B)

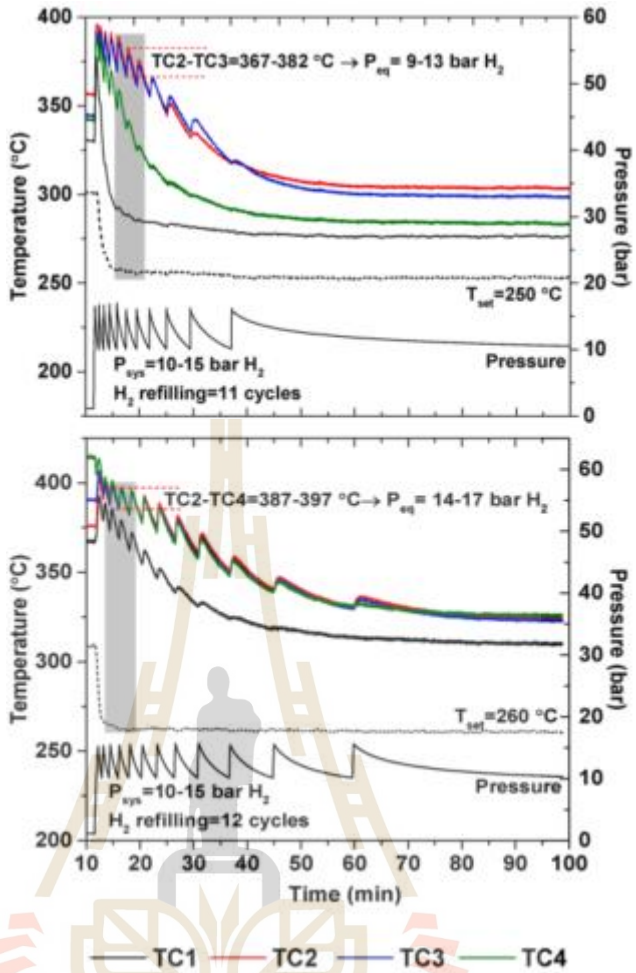

Figure 4.11 Temperatures, pressure, and hydrogen flow rate profiles during rehydrogenation of MgH_2-NbF_5-5%CNT (A) and MgH_2-NbF_5-10%CNT (B) tanks.

For hydrogenation at MgH_2-NbF_5-10%CNT tank at T_{set} = 260 °C, comparable plateau temperatures of 387–397 °C (P_{eq} = 14–17 bar H_2) are detected at TC2–TC4 (Figure 4.11(B)). Over 12 hydrogen refilling cycles, the hydrogenation at TC2–TC4 is effectively achieved and completes within 70 min, while that at TC1 terminates earlier at ~50 min. The P_{eq} values of MgH_2-NbF_5-10%CNT tank (14–17 bar H_2) approach P_{sys} (10–15 bar H_2) and are greater than those of the MgH_2-NbF_5-5%CNT tank (9–13 bar H_2). This suggests the enhancement of hydrogen diffusion after increasing the MWCNTs content, corresponding to the previous reports on hydrides doped with carbon materials (Plerdsranoy, Chanthee, and Utke, 2016; Sitthiwet, Plerdsranoy, and Dansirima, 2020; Thaweelap et al., 2017).

The superior hydrogenation performances at the middle positions of both tanks (TC2–TC3) can be explained by not only the suitable temperature, but also good hydrogen diffusion due to the location near the SS mesh tubes and central heater (Figure 4.9). With respect to the performance observed at TC2–TC3, the hydrogen absorption at TC4 in the MgH_2-NbF_5-10%CNT tank is competitive, while that in the MgH_2-NbF_5-5%CNT tank is significantly reduced. In the case of TC1, its hydrogenation kinetics is sluggish when compared with the other positions for both tanks although it is placed directly at the H_2 inlet/outlet side. Considering the long distance from the tank center of TC1, hydrogen diffusion in the radial direction of the tank is not effective. However, the absorption performances at TC1 and TC4 enhance remarkedly after increasing the MWCNTs content (MgH_2-NbF_5-10%CNT tank in Figure 4.11(B)). The latter is likely due to the improvement in hydrogen diffusion in both the radial and axial directions.

The cycling stability upon 10–15 hydrogen release and uptake cycles of both tanks is further characterized. The average total and material hydrogen capacities of the MgH_2-NbF_5-5%CNT tank are 2.80 and 2.66 wt. % H_2, respectively (Figure 4.12(A)), while those of the MgH_2-NbF_5-10% CNT tank are higher up to 3.51 and 3.39 wt. % H_2, respectively (Figure 4.12(B)). Slight particle agglomeration in the powder samples from both tanks is observed after cycling (Figure 4.12), which benefited from the MWCNTs. Considering the total NbF_5 and MWCNTs contents (10 and 15 wt. % with respect to MgH_2), the theoretical hydrogen capacities of MgH_2-NbF_5-5%CNT and MgH_2-NbF_5-10%CNT are 6.84 and 6.46 wt. % H_2, respectively.

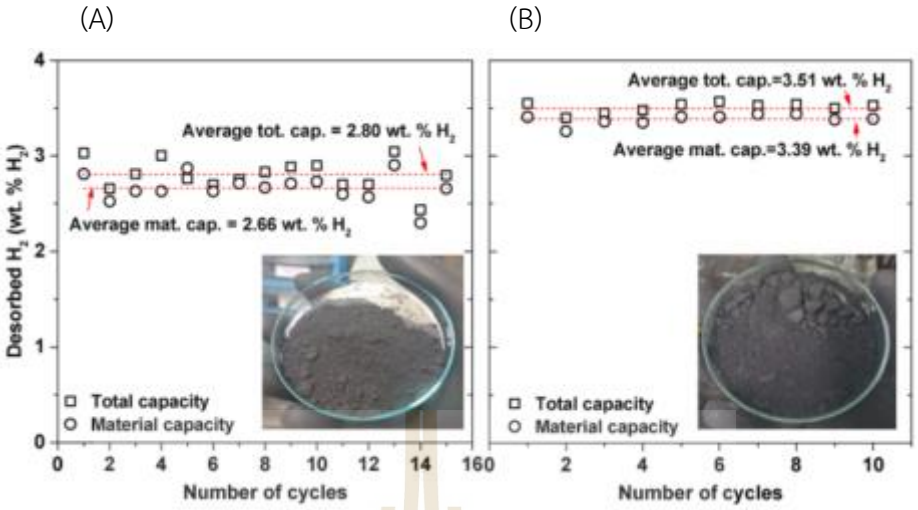

Figure 4.12 Hydrogen contents released and reproduced upon 10–15 cycles of MgH_2-NbF_5- 5%CNT (A) and MgH_2-NbF_5-10%CNT (B) tanks as well as the appearance of the powder samples after cycling.

Upon cycling, the MgH_2-NbF_5-10%CNT tank stores hydrogen up to 52.5% of the theoretical capacity, while the MgH_2-NbF_5-5%CNT tank preserves only 38.9%. According to the enhancement in the thermal conductivity and hydrogen diffusion obtained from increasing MWCNTs content, the de/rehydrogenation kinetics and reversibility of the MgH_2-based tank are considerably improved.

To explain de/rehydrogenation performance of the powder samples located at different positions in the tanks, the chemical compositions after cycling are investigated using PXD technique. Due to the comparable kinetics observed upon cycling (Figure 4.12), the powder samples after 10–15 de/rehydrogenation cycles from both tanks are selected for characterizations. From Figure 4.13(A), the as-prepared MgH_2NbF_5-5%CNT and the 15th dehydrogenated samples collected from the TC1–TC4 positions of the MgH_2-NbF_5-5%CNT tank show comparable diffractions of MgH_2, Mg, and MgO. Slight content of Mg in as-prepared sample suggests incomplete hydrogenation of Mg into MgH_2 during sample preparation, while MgO implies partial oxidation of Mg-containing phases during the experiments. The residual MgH_2 observed at all of the positions indicates incomplete dehydrogenation, corresponding to deficient hydrogen capacity with respect to the theoretical value (Figure 4.12). The higher the relative content of Mg to MgH_2, the more the effective dehydrogenation

($MgH_2 \longrightarrow Mg + H_2$). The content of Mg relative to MgH_2 at TC2 and TC3 is significantly greater than those at TC1 and TC4 (Figure 4.13(A)).

(A)

(B)

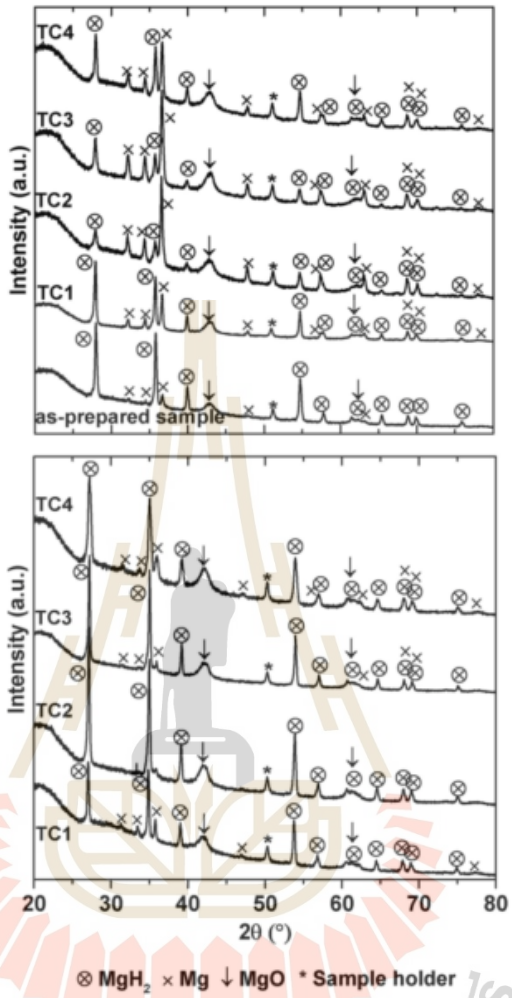

Figure 4.13 PXD patterns of MgH_2-NbF_5-5%CNT at as-prepared state and after the 15th dehydrogenation (A) and the 15th rehydrogenation (B) at different positions inside the tanks.

For rehydrogenation, the 15th hydrogenated powder sample mainly exhibits the diffraction of MgH_2 together with a small amount of unreacted Mg, indicating the successful hydrogenation (Figure 4.13(B)). For the MgH_2-NbF_5-10%CNT tank, the 10th dehydrogenated sample exhibits diffraction patterns of Mg, MgO, and MgH_2 (only at TC1–TC3) (Figure 4.14(A)). The formation of Mg together with the reduction of the MgH_2 indicates successful dehydrogenation of MgH_2 into Mg. With respect to TC1, the high relative contents of Mg to MgH_2 at TC2–TC3 and the disappearance of MgH_2 at TC4 suggest effective dehydrogenation, in accordance with the temperature, pressure,

and hydrogen flow rate profiles observed during the dehydrogenation of the MgH_2-NbF_5-10%CNT tank (Figure 4.10(B)). After the 10th rehydrogenation, the samples at all positions of the MgH_2-NbF_5-10%CNT tank reveal the diffraction peaks of MgH_2 and MgO (Figure 4.14(B)). The formation of MgH_2 without Mg indicates successful rehydrogenation. Considering the diffraction patterns of all samples in the as-prepared state and after cycling (Figure 4.13 and Figure 4.14), there are no characteristic peaks of Nb and F-containing phases, which can be attributed to their small amount, amorphous state, and/or inhomogeneity.

From the previously reported MgH_2-based tank with the smaller packing volume (96.20 mL) and coupling with external heater and central tube heat exchanger, the reversible hydrogen capacity of up to 5.6 wt. % was obtained upon 20 cycles (Thiangviriya et al., 2019; Thongtan et al., 2018). The poorer de/rehydrogenation performance of the current MgH_2-based hydrogen storage tank can be explained by the deficient hydrogen diffusion and heat management due to the greater amount of sample and no heat exchanger. Thus, further studies will focus on designing and fabricating the hydrogen storage tank to favor gas diffusion and heat management inside the hydride bulk material.

(A)

(B)

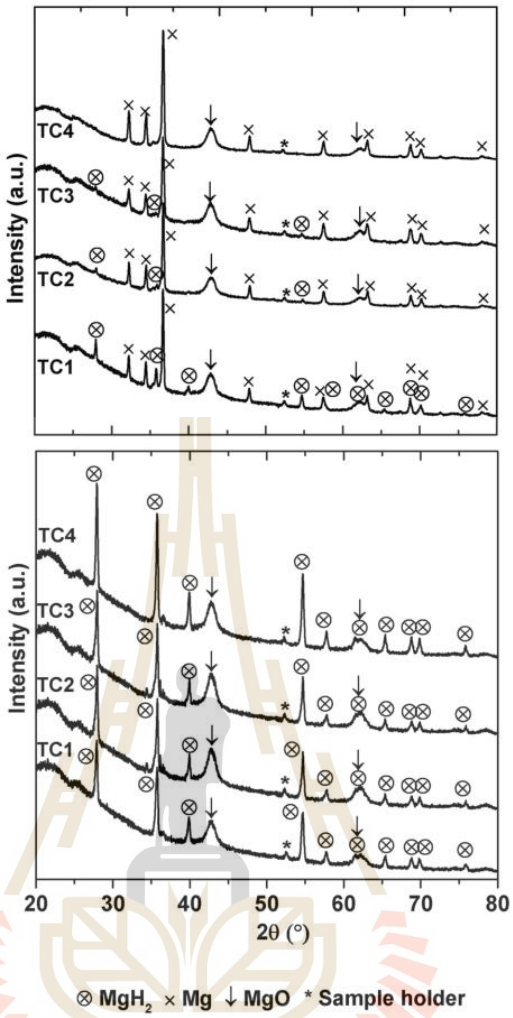

Figure 4.14 PXD patterns of MgH_2-NbF_5-10%CNT after the 10th dehydrogenation (A) and the 10th rehydrogenation (B) at different positions inside the tanks.

In this study, MgH_2 doped with NbF_5 and 5-10 wt. % MWCNTs are packed in the cylindrical tank with central heater. The investigation reveals superior de/rehydrogenation kinetics at the middle positions of the tank due to effective heat supply and hydrogen diffusion. However, radial direction performance is hindered by insufficient thermal conductivity and hydrogen diffusion, leading to sluggish hydrogen sorption kinetics. Increasing MWCNTs content significantly improvs hydrogen de/absorption kinetics at all tank positions, resulting in increased capacities over multiple cycles. The MgH_2-based tank with 10 wt. % MWCNTs demonstrates superior reversibility and effective de/rehydrogenation, despite challenges in homogeneity. Design modifications, incorporating a heat exchanger and gas diffusion pathways, are suggested to address these issues.

4.2 MgH_2-based thermal storage tank and system

Phase compositions of HTMH (MgH_2–Nb_2O_5-graphite) are characterized by PXD. From Figure 4.15, PXD pattern of HTMH reveals the diffractions of MgH_2 and slight Mg, implying successful hydrogenation. The residual Mg content is likely due to partial dehydrogenation and/or incomplete hydrogenation during sample preparation. The absence of Nb_2O_5 signal can be explained by the amorphous state and/or the nanosized particles, resulting from ball milling process.

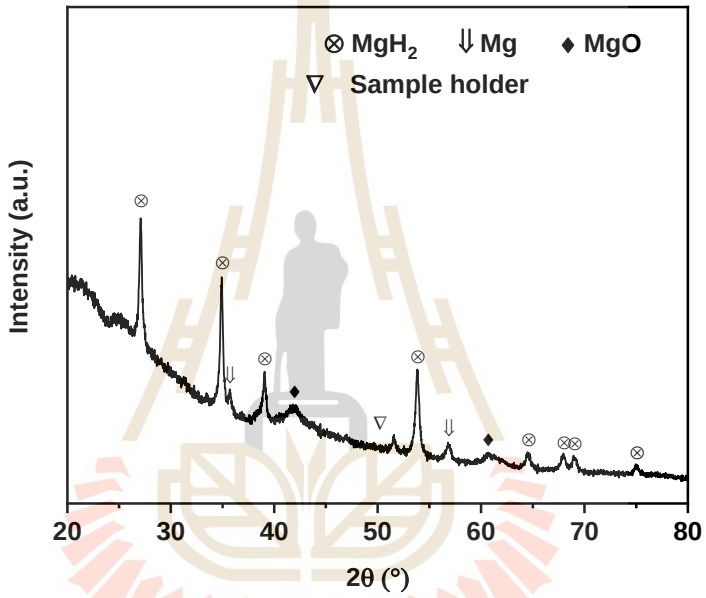

Figure 4.15 PXD spectrum of as-prepared HTMH.

According to the theoretical H_2 capacity of MgH_2 (HTMH) and $LaNi_5$ (LTMH) (7.6 and 1.4 wt. % H_2, respectively (Prigent and Joubert, 2011; Shang, Pistidda, Gizer, Klassen, and Dornheim, 2021)), the weight ratio of HTMH:LTMH is assigned as 1:6 to ensure that LTMH is capable to absorb all H_2 released from HTMH during the H_2 exchange reaction. HTMH (40 g) and LTMH (240 g) are packed separately into the SS mesh cylinders and placed inside the storage tank with the packing volume of 96.2 mL. Round-shaped SS mesh sheets are inserted in the powder to improve hydrogen permeability inside the tanks (Figure 3.5). Both tanks are mounted with double tube heat exchanger.

The performance and the reaction mechanisms of the coupled HTMH-LTMH involve monitoring (i) temperatures at various positions in HTMH and LTMH beds, as

well as heat transfer fluid (HTF), (ii) hydrogen pressures, (iii) hydrogen flow rates exchanging between HTMH and LTMH, and (iv) HTF flow rate. The process initiates with activating HTMH at T_{set} = 370 °C under the initial hydrogen pressure of 0.25 bar with the hydrogen flow direction of HTMH ⟶ LTMH. Heat discharging occurs by cooling HTMH to T_{set} = 200 °C, while heat charging involves reheating HTMH to T_{set} = 370 °C. The hydrogen flow directions during heat charging and discharging are HTMH ⟶ LTMH and LTMH ⟶ HTMH, respectively. Cycling stability of the coupled HTMH-LTMH reveals consistent patterns in temperatures, pressures, and H_2 flow rates over 16 heat dis/charging cycles (Figure 4.16). To inspect the detailed mechanisms of the initial state and after cycling, variations in (i) temperatures of hydrides (TC1-TC4 for HTMH and TC1-TC3 for LTMH) and HTF ($T_{air\text{-}in}$ and $T_{air\text{-}out}$,), (ii) pressures of HTMH and LTMH (P_{HT} and P_{LT}, respectively), and (iii) H_2-flow rate during the 1st-2nd cycle (t= 0–12 h) and the 15th cycle (t= 102–108 h) are considered. For activation process (t=0-2 h), temperatures at all positions in HTMH beds rise up to T_{set} = 370 °C along with the increased P_{HT} up to 3.8 bar H_2 due to hydrogen desorption (Figure 4.17). At t~1h, the increase of H_2 frow rate and pressure indicates HTMH hydrogen desorption of T_{onset} = 250 °C (Figure 4.17). H_2-flow rate (HTMH ⟶ LTMH) and P_{LT} enhance to 268 SCCM and 3.8 bar H_2, respectively (Figure 4.17(B)). Hydrogen absorption at LTMH is assured by the elevated temperatures at TC1-TC3 to the equilibrium temperature (T_{eq}) of 39-43 °C (Figure 4.17(A)).

(A)

(B)

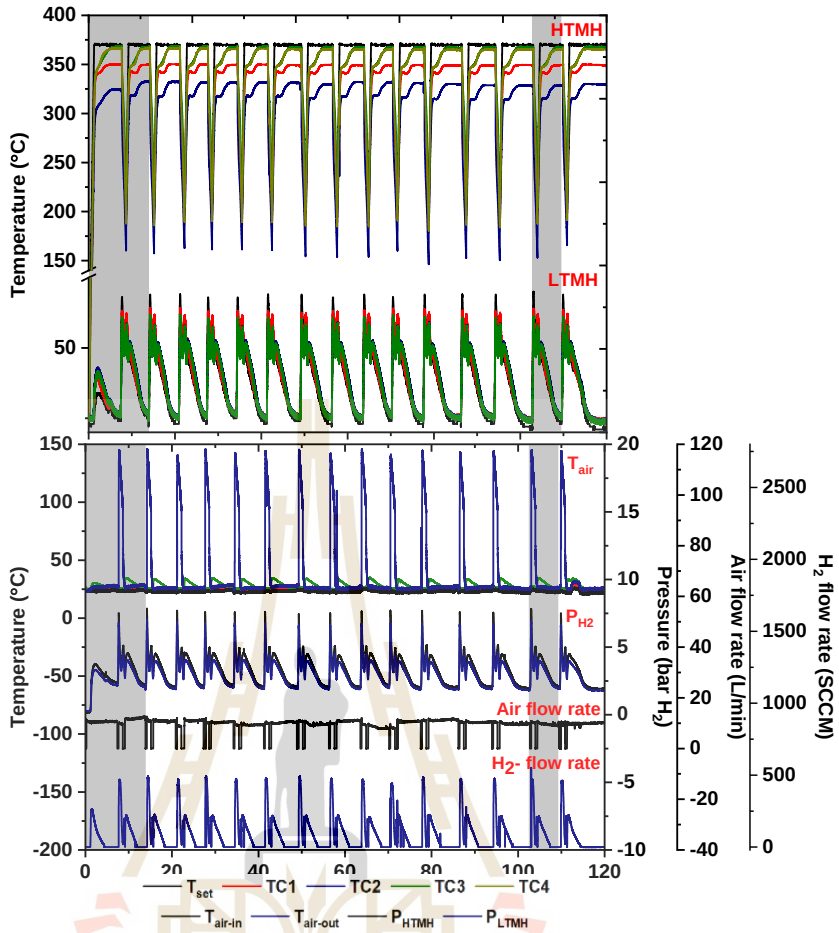

Figure 4.16 Temperatures of HTMH, LTMH, and HTF (compressed air), pressures of HTMH and LTMH, and hydrogen mass flow rate exchanging between HTMH and LTMH upon 16 heat storage cycles of the coupled MgH_2–$LaNi_5$ thermal storage.

The decrease in temperature in HTMH, detected by TC1-TC4 is due to the endothermic reaction (Figure 4.17(A)). Within 4 h and 27 min, temperature at TC3 and TC4 stabilize at T_{set} = 370 °C, while those at TC1 and TC2 are lower at 350 and 325 °C, respectively (Figure 4.17(A)). Low temperature at TC1 and TC2 may be attributed to their positions away

(A)

(B)

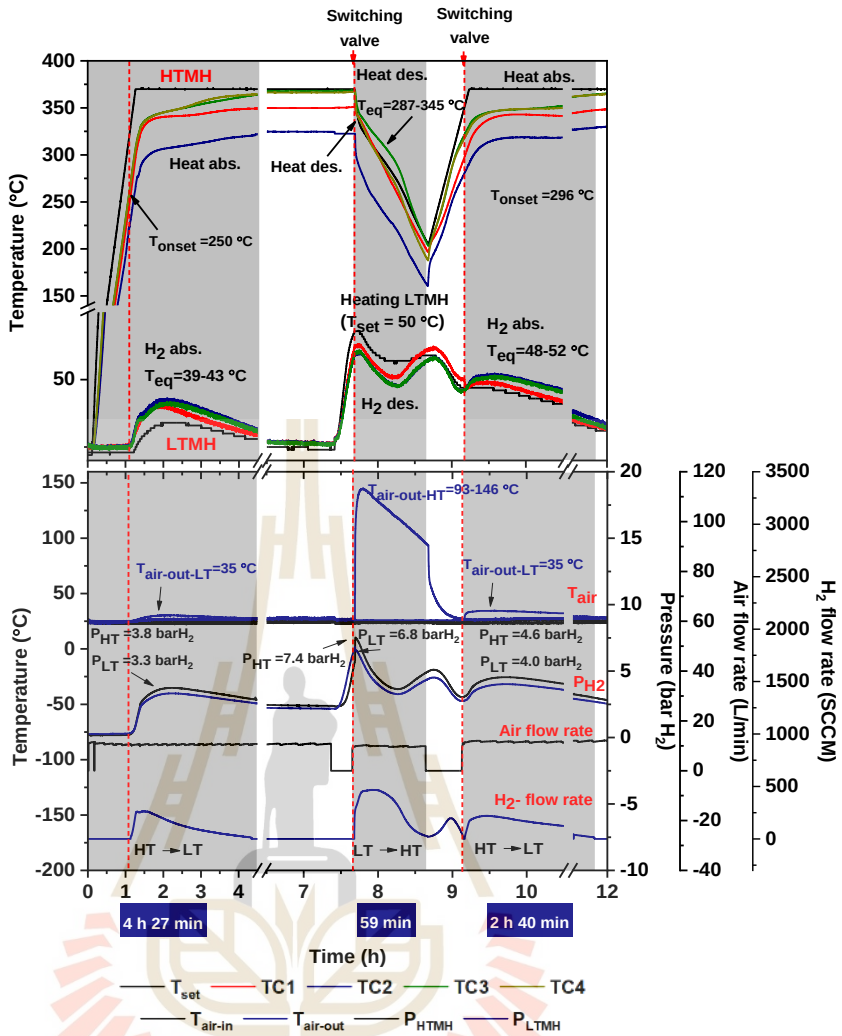

Figure 4.17 Temperatures of HTMH, LTMH, and HTF (compressed air), pressures of HTMH and LTMH, and hydrogen mass flow rate exchanging between HTMH and LTMH during activation and the 1st cycle of the coupled MgH_2–$LaNi_5$ thermal storage.

from the tank wall, where the heater is attached. Complete activation is observed by the reduction of H_2-flow rate (Figure 4.17(B)). In LTMH, comparable temperature profiles are found at TC1-TC3 (39-43 °C), suggesting homogeneous hydrogen absorption performance at all positions in the tank (Figure 4.17(A)).

Furthermore, the reaction mechanisms during the 1st heat discharging are studied. Dehydrogenation of LTMH is carried out by heating to T_{set} = 50 °C (t~7 h 30 min), leading to the enhanced P_{LT} to 6.8 bar H_2 (Figure 4.17(A)). An increase of P_{HT} to 7.4 bar H_2 indicates the continuous incomplete HTMH dehydrogenation at a very low rate. Comparable temperature profiles at TC1-TC3 of LTMH tank indicate

homogeneous dehydrogenation. Meanwhile, the heater at HTMH is turned off and compressed air used as HTF is applied through heat exchanger inside the tank at a 10 L/min. The increased H_2-flow rate, corresponding to the hydrogen flow signal from LTMH to HTMH confirms heat discharging or hydrogen absorption at the HTMH. The plateau temperatures at 287-345 °C are observed at TC1-TC4 of HTMH (Figure 4.17(A)) and the increase of HTF temperature ($T_{air\text{-}out}$) to 93–146 °C suggests heat discharging (Figure 4.17(B)). The greater P_{HT} (7.4 bar H_2) than the equilibrium pressure (P_{eq}) of MgH_2 at these plateau temperatures (~5.7 bar H_2 (Chawla, Yadav, Bajpai, Kumar, and Lal, 2021)) encourages heat discharging (hydrogen absorption) of HTMH. Due to the poor heat transfer inside HTMH tank, temperature gradient at different locations are observed. This may result in an uneven reaction in HTMH beds. At t~8.3 h, both P_{HT} and P_{LT} increase to 5.1 and 4.5 bar H_2, respectively. This indicates no further hydrogen absorption at HTMH due to not sufficient heat to overcome the activation barrier. Meanwhile, LTMH still releases hydrogen causing an increase of system pressure. Complete heat discharge is observed within 59 min, revealed as the reduction of H_2-flow rate, $T_{air\text{-}out}$, and P_{HT} and P_{LT}.

Afterwards, heat charging is continued (t~8.5 h) by heating HTMH to T_{set} = 370 °C and turned off the heater at LTMH. Upon heating HTMH, the H_2-flow rate signal increases and corresponds to the hydrogen flow direction of LTMH⟶HTMH is observed. This implies the additional hydrogen absorption of HTMH upon heat charging. It is likely due to hydrogen absorption of HTMH cannot be fully obtained due to poor kinetics and/or fast temperature reduction rate. The latter results in deficient heat release from HTMH. Such issue might be solved by slowing down the cooling rate during heat discharging of HTMH or improving absorption kinetics of hydride materials used as HTMH. At t ~9 h 10 min, H_2-flow rate decreases to 0 SCCM, indicating no further flow of H_2 from LTMH to HTMH. To start heat charging, several valves are switched to redirect the hydrogen flow from HTMH to LTMH. The HTF at the same condition as heat discharging step is applied to LTMH. At ~296 °C, HTMH undergoes heat charging process, indicated by the slightly interrupted period in temperature profiles at TC3 and TC4 along with the increase of P_{LT} and P_{HT} to 4.0 and 4.6 bar H_2, respectively. (Figure 4.17). Since P_{HT} is greater than P_{LT}, the hydrogen flow

direction of HTMH⟶LTMH is assigned. The increase of H_2-flow rate and temperatures of all TCs in LTMH (48–52 °C) is attributed to exothermic hydrogen absorption of LTMH. The reactions upon heat charging of HTMH are complete within 2 h 40 min, shown as the reduction of H_2-flow rate and all temperatures of LTMH as well as comparable P_{HT} and P_{LT} (Figure 4.17).

To validate the cycling stability of the MgH_2–$LaNi_5$ thermal storage system, the performance and hydrogen exchange reactions during the 15th cycle are analyzed. The temperature and pressure profiles during the 15th cycle are comparable to those of the 1st cycle (Figure 4.17). During heat discharging, plateau temperatures at HTMH at TC3 and $T_{air\text{-}out}$ are 284–344 °C and 85–145 °C, respectively, while maximum P_{HT} and P_{LT} are 7.8 and 6.9 bar H_2, respectively. Additionally, during heat charging at t~104 h, HTMH exhibits additional hydrogen absorption, indicated by the increase of H_2-flow rate signal upon heating. The heat charging process begins at an onset temperature of 298 °C leading to the maximum P_{HT} of 3.9 bar H_2. Simultaneously, hydrogen absorption of LTMH is observed as elevated temperatures at all TCs to 48–52 °C (Figure 4.18). It's notable that all parameters for HTMH, LTMH, and HTF (temperature, pressure, and H_2-flow rate) during the 1st and 15th heat dis/charging cycles are comparable, suggesting good cycling stability of the heat storage system. The reaction time during the 1st and 15th heat discharging are comparable at around 59 min, while the heat discharging time enhances by 16 min upon cycling. This might be explained by poor hydrogen diffusion in the hydride beds due to particle sintering or agglomeration upon cycling under temperature and pressure conditions.

(A)

(B)

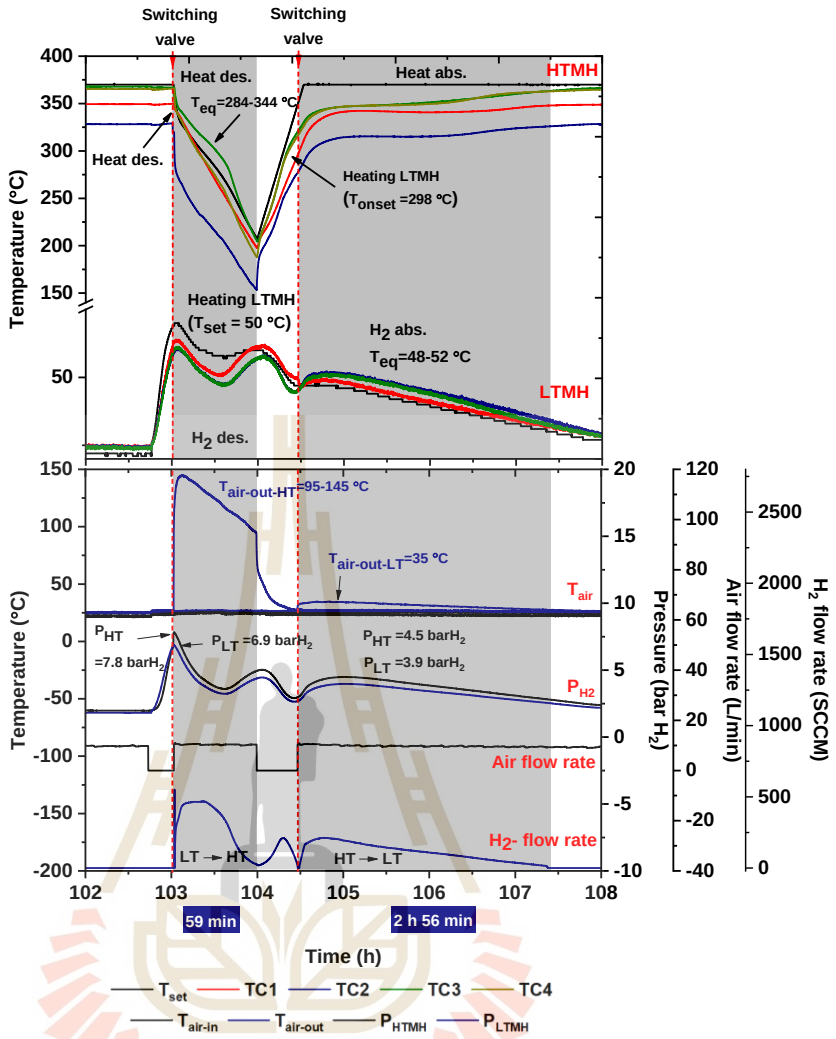

Figure 4.18 Temperatures of HTMH, LTMH, and HTF (compressed air), pressures of HTMH and LTMH, and hydrogen mass flow rate exchanging between HTMH and LTMH during the 15th cycle of the coupled MgH_2–$LaNi_5$ thermal storage.

Hydrogen content exchange between HTMH and LTMH over 16 heat storage cycles are measured. From Figure 4.19, 0.95 mol H_2 transfer from HTMH to LTMH during activation. This is in accordance with the storage capacity of 4.78 wt. % H_2 for HTMH. Deficient H_2 capacity compared to theoretical of 7.6 wt. % H_2 is attributed to incomplete hydrogenation and the oxidation to MgO of sample during preparation process, corresponding to the PXD spectrum in Figure 4.15.

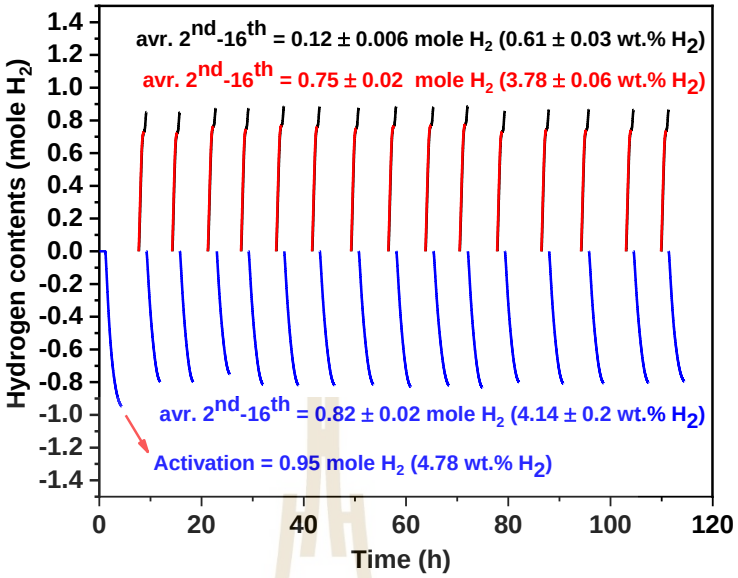

Figure 4.19 Hydrogen contents exchange between HTMH and LTMH upon 16 heat storage cycles.

Upon 16 heat discharging cycles, intrinsic hydrogen contents transferring from LTMH to HTMH are 0.75 ± 0.02 mol H_2 or 3.78 ± 0.06 wt. % H_2. During heat charging, HTMH slightly absorbs 0.12 ± 0.006 mol H_2 or 0.61 ± 0.03 wt. % H_2, as shown by the H_2-flow rate signal (LTMH⟶ HTMH) during heating to T_{set}~200–300 °C (Figure 4.17 and Figure 4.18). For heat charging, 0.82 ± 0.02 mol H_2 or 4.14 ± 0.2 wt. % H_2 transfer from HTMH to LTMH upon cycling. Considering the hydrogen content liberated from HTMH during activation (0.95 mol or 4.78 wt. % H_2), up to 86% of the total hydrogen content stored in the HTMH participates in the heat charging and discharging reactions. Moreover, consistent amounts of hydrogen exchange between HTMH and LTMH upon 16 cycles suggest superior cycling stability of the coupled MgH_2–$LaNi_5$ thermal storage. From our previous work, the inlet pressure (P_{inlet}) for mass flow controller (MFC) during heat charging and discharging was set at 5 bar H_2 using pressure regulator (PR) for safety reasons. This causes pressure retention inside HTMH and LTMH, resulting in inefficient hydrogen exchange reactions. This led to only 57% of total hydrogen capacity transferring between HTMH and LTMH (Thiangviriya, Thongtan, Thaweelap, Plerdsranoy, and Utke, 2024).

The energy densities during heat charging and discharging of the coupled MgH_2–$LaNi_5$ thermal storage are calculated using equation (4.1) (Urbanczyk, Peinecke, Peil, and Felderhoff, 2017). The number of hydrogen moles exchange between HTMH and LTMH upon 16 cycles during heat discharging and charging are 0.75 ± 0.02 and 0.82 ± 0.02 mol H_2, respectively (Figure 4.19). These result in the energy densities of 1406 ± 31 and 1513 ± 36 kJ/kg, for heat discharging and charging, respectively.

$$Q = \frac{(n_{H_2}\Delta H_R)\times 1000}{m_{HTMH}} \tag{4.1}$$

where n_{H_2} is the moles of consumed (Q_{des})/released (Q_{abs}) hydrogen, ΔH_R is the enthalpy of the reaction (~75 kJ/mol H_2 for MgH_2 (Shang et al., 2021)), and m_{HTMH} is the mass of HTMH powder (40 g). Moreover, the energy densities during heat discharging can be calculated using the temperature changes of HTF (compressed air) applied during heat discharging as shown in equation (4.2) ("A Heat Transfer Textbook, 5th Edition," n.d.).

$$Q = mc_p\Delta T \tag{4.2}$$

Where m is the mass of the HTF (kg), C_p is the specific heat of HTF over the operating temperature range operation (kJ/kgK^{-1}), and ΔT is the temperature difference (K). Considering air flowing through the hot system over a short period of time or a small volume of air. The air with a density (ρ) assumingly independent from temperature flows at a rate R(t) = dV/dt. With the mass of air (dm) flowing through the system and receives the reaction heat, thermal energy transports with the air (Q_{tot}) can be derived as following equations.

$$dQ = \rho R(t)\, c_p\, [\, T_{ex}(t)-T_{in}(t)\,]\, dt \tag{4.3}$$

$$Q_{tot} = \int_0^{Qtot} dQ \tag{4.4}$$

$$Q_{tot} = \rho c_p \int_{t_i}^{t_f} R(t)\, [\, T_{ex}(t)-T_{in}(t)\,]\, dt \tag{4.5}$$

In this work, ρ and C_p of air are considered to be constant of 1.168 kg/m^3 and 1.006 kJ/kgK^{-1}, respectively. From equation (4.5), the energy densities during 15 heat discharging cycles is 1583 ± 91 kJ/kg.

Furthermore, phase compositions of HTMH after the 16th heat charging at different positions inside the tank are investigated by PXD technique. From Figure 4.20, comparable diffraction patterns of Mg and MgO are observed at all positions. At the top position, slight signals of MgH_2 are observed. This can be attributed to a partial hydrogenation during cooling down, which HTMH can absorb the remaining pressure. The formation of Mg confirms successful dehydrogenation during heat charging of HTMH, while that of MgO indicates oxidation of Mg-containing phases with oxygen and/or humidity during the experiments. A signal of catalytic phase (NbO_2) is also found at all positions. The significant diffractions of Mg are found at all positions indicating complete reaction throughout the length of the tank. This probably benefits from inserting the SS meshes inside the powder beds, increasing the gas diffusion pathways.

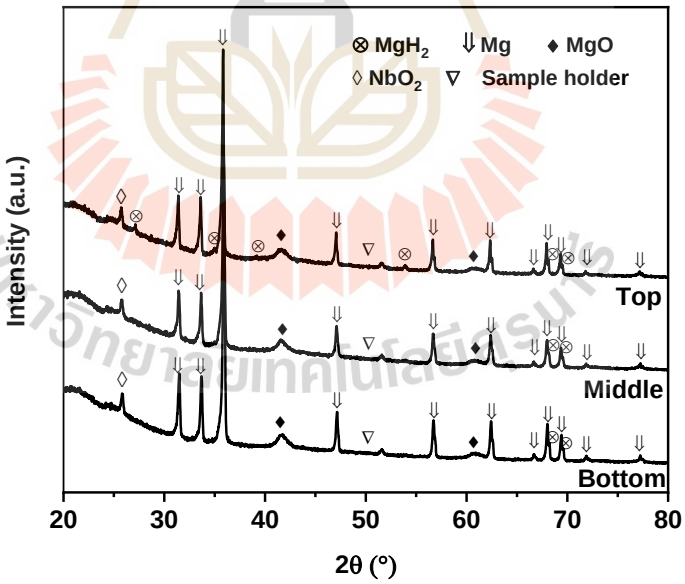

Figure 4.20 PXD spectra of HTMH after the 16th heat charging at different positions in the HTMH tank.

In conclusion, MgH_2 (40 g) and $LaNi_5$ (240 g) used as thermal battery (HTMH) and hydrogen reservoir (LTMH), respectively, are packed into small cylindrical tanks with the packing volumes of 96.2 mL. Thermal storage properties of MgH_2–$LaNi_5$ pair,

including heat charging and discharging performances, cycling stability, and hydrogen exchange reaction are investigated. Stability upon 16 heat storage cycles is observed with the hydrogen contents exchange between HTMH and LTMH up to 0.82 ± 0.02 mol H_2 or 4.14 ± 0.2 wt. % H_2. With respect to the hydrogen capacity of HTMH (4.78 wt. % H_2), up to 86% of theoretical capacity participates in heat storage cycles. The obtained heat storage densities during discharging and charging are 1406 ± 31 and 1513 ± 36 kJ/kg, respectively. The heat storage density calculated based on temperature changes of HTF applied during heat discharging process is 1583 ± 91 kJ/kg.

4.3 References

A Heat Transfer Textbook, 5th edition. (n.d.). Retrieved January 28, 2024, from https://ahtt.mit.edu/

Bogdanović, B., Ritter, A., and Spliethoff, B. (1990). Active MgH_2-Mg Systems for Reversible Chemical Energy Storage. *Angewandte Chemie International Edition in English*, *29*(3), 223–328. https://doi.org/10.1002/anie.199002233

Chaise, A., De Rango, P., Marty, P., and Fruchart, D. (2010). Experimental and numerical study of a magnesium hydride tank. *International Journal of Hydrogen Energy*, *35*(12), 6311–6322. https://doi.org/10.1016/j.ijhydene.2010.03.057

Chaise, A., de Rango, P., Marty, P., Fruchart, D., Miraglia, S., Olivès, R., and Garrier, S. (2009). Enhancement of hydrogen sorption in magnesium hydride using expanded natural graphite. *International Journal of Hydrogen Energy*, *34*(20), 8589–8596. https://doi.org/10.1016/j.ijhydene.2009.07.112

Chawla, K., Yadav, D. K., Bajpai, A., Kumar, S., and Lal, C. (2021). Hydrogenation properties and kinetic study of MgH_2 - x wt% AC nanocomposites prepared by ball milling. *Environmental Science and Pollution Research*, *28*(4), 3872–3879. https://doi.org/10.1007/S11356-020-08964-1

Felderhoff, M., and Bogdanović, B. (2009, January). High temperature metal hydrides as heat storage materials for solar and related applications. *International Journal of Molecular Sciences*, Vol. 10, pp. 335–344. https://doi.org/10.3390/ijms10010325

Garrier, S., Chaise, A., De Rango, P., Marty, P., Delhomme, B., Fruchart, D., and Miraglia, S. (2011). MgH_2 intermediate scale tank tests under various experimental conditions. *International Journal of Hydrogen Energy*, *36*(16), 9719–9726. https://doi.org/10.1016/j.ijhydene.2011.05.017

Klell, M. (2010). Storage of Hydrogen in the Pure Form. *Handbook of Hydrogen Storage: New Materials for Future Energy Storage*, 1–37. https://doi.org/10.1002/9783527629800.CH1

Lillo-Ródenas, M. A., Guo, Z. X., Aguey-Zinsou, K. F., Cazorla-Amorós, D., and Linares-Solano, A. (2008). Effects of different carbon materials on MgH_2 decomposition. *Carbon*, *46*(1), 126–137. https://doi.org/10.1016/j.carbon.2007.10.033

Lototskyy, M. V., Tolj, I., Pickering, L., Sita, C., Barbir, F., and Yartys, V. (2017, February 1). The use of metal hydrides in fuel cell applications. *Progress in Natural Science: Materials International*, Vol. 27, pp. 3–20. Elsevier B.V. https://doi.org/10.1016/j.pnsc.2017.01.008

Luo, Y., Wang, P., Ma, L. P., and Cheng, H. M. (2008). Hydrogen sorption kinetics of MgH_2 catalyzed with NbF_5. *Journal of Alloys and Compounds*, *453*(1–2), 138–142. https://doi.org/10.1016/J.JALLCOM.2006.11.113

Ma, T., Isobe, S., Morita, E., Wang, Y., Hashimoto, N., Ohnuki, S., ... Kojima, Y. (2011). Correlation between kinetics and chemical bonding state of catalyst surface in catalyzed magnesium hydride. *International Journal of Hydrogen Energy*, *36*(19), 12319–12323. https://doi.org/10.1016/J.IJHYDENE.2011.07.011

Malka, I. E., Pisarek, M., Czujko, T., and Bystrzycki, J. (2011). A study of the ZrF_4, NbF_5, TaF_5, and $TiCl_3$ influences on the MgH_2 sorption properties. *International Journal of Hydrogen Energy*, *36*(20), 12909–12917. https://doi.org/10.1016/J.IJHYDENE.2011.07.020

Mustafa, N. S., and Ismail, M. (2017). Hydrogen sorption improvement of MgH_2 catalyzed by CeO_2 nanopowder. *Journal of Alloys and Compounds*, *695*, 2532–2538. https://doi.org/10.1016/J.JALLCOM.2016.11.158

Plerdsranoy, P., Chanthee, S., and Utke, R. (2016). Compaction of $LiBH_4$ -MgH_2 doped with MWCNTs-TiO_2 for reversible hydrogen storage. 1–9. https://doi.org/10.1016/j.ijhydene.2016.11.066

Plerdsranoy, P., Thiangviriya, S., Dansirima, P., Thongtan, P., Kaewsuwan, D., Chanlek, N., and Utke, R. (2019). Synergistic effects of transition metal halides and activated carbon nanofibers on kinetics and reversibility of MgH_2. *Journal of Physics and Chemistry of Solids*, *124*, 81–88. https://doi.org/10.1016/j.jpcs.2018.09.001

Popilevsky, L., Skripnyuk, V. M., Amouyal, Y., and Rabkin, E. (2017). Tuning the thermal conductivity of hydrogenated porous magnesium hydride composites with the aid of carbonaceous additives. *International Journal of Hydrogen Energy*, *42*(35), 22395–22405. https://doi.org/10.1016/j.ijhydene.2017.04.088

Prigent, J., and Joubert, J. M. (2011). The phase diagrams of the ternary systems La-Ni-M (M = Re, Ru, Os, Rh, Ir, Pd, Ag, Au) in the La-poor region. *Intermetallics*, *19*(3), 295–301. https://doi.org/10.1016/j.intermet.2010.10.016

Shang, Y., Pistidda, C., Gizer, G., Klassen, T., and Dornheim, M. (2021, November 15). Mg-based materials for hydrogen storage. *Journal of Magnesium and Alloys*, Vol. 9, pp. 1837–1860. National Engg. Reaserch Center for Magnesium Alloys. https://doi.org/10.1016/j.jma.2021.06.007

Sitthiwet, C., Plerdsranoy, P., and Dansirima, P. (2020). Improved hydrogen sorption kinetics of compacted $LiNH_2$–LiH based small hydrogen storage tank by doping with TiF4 and MWCNTs. *Journal of Alloys and Compounds*, 155026. https://doi.org/10.1016/j.jallcom.2020.155026

Sulaiman, N. N., and Ismail, M. (2016). Enhanced hydrogen storage properties of MgH_2 co-catalyzed with K_2NiF_6 and CNTs. *Dalton Transactions*, *45*(48), 19380–19388. https://doi.org/10.1039/c6dt03646e

Thaweelap, N., Thongtan, P., Sitthiwet, C., Thiangviriya, S., Eiamlamai, P., and Utke, R. (2017). Hydrogen sorption, kinetics, reversibility, and reaction mechanisms of MgH_2-x$LiBH_4$ doped with activated carbon nanofibers for reversible hydrogen storage based laboratory powder and tank scales. *International Journal of Hydrogen Energy*, *42*(39), 24915–24926. https://doi.org/10.1016/j.ijhydene.2017.08.075

Thiangviriya, S., Plerdsranoy, P., Sitthiwet, C., Dansirima, P., Thongtan, P., Eiamlamai, P., … Utke, R. (2019). MgH_2–TiF_4-MWCNTs based hydrogen storage tank with central tube heat exchanger. *International Journal of Hydrogen Energy*, *44*(36), 20173–20182. https://doi.org/10.1016/j.ijhydene.2019.06.002

Thiangviriya, S., Thongtan, P., Thaweelap, N., Plerdsranoy, P., and Utke, R. (2024). Heat charging and discharging of coupled MgH_2–$LaNi_5$ based thermal storage: Cycling stability and hydrogen exchange reactions. *International Journal of Hydrogen Energy*, *49*, 59–66. https://doi.org/10.1016/J.IJHYDENE.2023.10.312

Thongtan, P., Dansirima, P., Thiangviriya, S., Thaweelap, N., Suthummapiwat, A., Plerdsranoy, P., and Utke, R. (2018). Reversible hydrogen sorption and kinetics of hydrogen storage tank based on MgH_2 modified by TiF_4 and activated carbon.

International Journal of Hydrogen Energy, *43*(27), 12260–12270. https://doi.org/10.1016/j.ijhydene.2018.04.171

Urbanczyk, R., Peinecke, K., Peil, S., and Felderhoff, M. (2017). Development of a heat storage demonstration unit on the basis of Mg_2FeH_6 as heat storage material and molten salt as heat transfer media. *International Journal of Hydrogen Energy*, *42*(19), 13818–13826. https://doi.org/10.1016/J.IJHYDENE.2017.02.160

Wang, Y., Wang, Y., Zhang, Q., Jiao, L., and Yuan, H. (2015). Catalytic effects of different Ti-based materials on dehydrogenation performances of MgH_2. *Journal of Alloys and Compounds*, *645*(S1), S509–S512. https://doi.org/10.1016/J.JALLCOM.2014.12.071

Yu, H., Bennici, S., and Auroux, A. (2014). Hydrogen storage and release: Kinetic and thermodynamic studies of MgH_2 activated by transition metal nanoparticles. *International Journal of Hydrogen Energy*, *39*(22), 11633–11641. https://doi.org/10.1016/J.IJHYDENE.2014.05.069

Zhang, J., Yu, X. F., Mao, C., Long, C. G., Chen, J., and Zhou, D. W. (2015). Influences and mechanisms of graphene-doping on dehydrogenation properties of MgH_2: Experimental and first-principles studies. *Energy*, *89*, 957–964. https://doi.org/10.1016/J.ENERGY.2015.06.037

Zhang, Jianfeng, Li, Z., Wu, Y., Guo, X., Ye, J., Yuan, B., ... Jiang, L. (2018). Recent advances on the thermal destabilization of Mg-based hydrogen storage materials. *RSC Advances*, *9*(1), 408–428. https://doi.org/10.1039/C8RA05596C

CHAPTER V
CONCLUSIONS

In summary, this thesis aimed to develop the hydrogen sorption kinetic properties of MgH_2 by doping with transition metal catalysts and carbon materials at laboratory and storage tank scales. In addition, the investigations of thermal storage system based on the coupled MgH_2 (HTMH) and $LaNi_5$ (LTMH) were also performed.

MgH_2 doped with TiF_4 and activated carbon (AC) demonstrated the notable reduction in dehydrogenation temperatures, although incomplete hydrogenation during sample preparation resulted in the lower-than-expected hydrogen capacity of 4.4 wt. % H_2. Dehydrogenation of the MgH_2-TiF_4-AC tank revealed deficient capacity due to incomplete reactions. Improvements were made by increasing the number of hydride beds and inserting the stainless-steel mesh tubes at the tank center. These enhanced hydrogen permeability and de/rehydrogenation kinetics. Initial cycles exhibited gravimetric and volumetric capacities of 4.46 wt. % H_2 and 28 g H_2/L. Upon cycling, the capacities stabilized at 3.42-3.62 wt. % H_2 and 22-23 gH_2/L. Despite homogeneous heat transfer along the tank radius, the decayed hydrogen permeability towards the tank wall resulted in inferior kinetics. Challenges relating to particle sintering and/or agglomeration upon cycling were responsible to the inferior hydrogen content.

MgH_2 doped with NbF_5 and 5-10 wt. % MWCNTs exhibited superior de/rehydrogenation kinetics in tank scale mounted with a central heater. Optimal performance was observed at the middle positions due to effective heat supply and hydrogen diffusion. However, the performance in the radial direction was hindered by insufficient thermal conductivity and hydrogen diffusion, leading to sluggish hydrogen sorption kinetics. Increasing MWCNTs content up to 10 wt. % significantly improved hydrogen de/absorption kinetics at all tank positions. This elevated the hydrogen capacities over multiple cycles. Suggestions for tank design and fabrication with

superior heat exchanger and gas diffusion pathways were proposed to address these issues.

Additionally, the coupled MgH_2 (HTMH)–$LaNi_5$ (LTMH) as the thermal storage system demonstrated stability over 16 heat storage cycles. Hydrogen contents exchanged between HTMH and LTMH were up to 0.82 ± 0.02 mol H_2 or 4.14 ± 0.2 wt. % H_2. Approximately 86% of the theoretical capacity of HTMH (4.78 wt. % H_2) participated in heat storage cycles. The obtained heat storage densities during discharging and charging were 1406 ± 31 and 1513 ± 36 kJ/kg, respectively. The calculated heat storage density based on temperature changes of the heat transfer fluid (compressed air) used during heat discharging was 1583 ± 91 kJ/kg.

CURRICULUM VITAE

Name Mr. Phutthimet Thongtan

Education

	2013-2017	B.Sc. (Chemistry), Suranaree University of Technology
	2017-present	Ph.D. candidate (Chemistry), Suranaree University of Technology

Research abroad

	2022-2023	Institute of Hydrogen Technology, Helmholtz-Zentrum Hereon, Geesthacht, Germany

Publication

Thiangviriya, S., Thongtan, P., Thaweelap, N., Plerdsranoy, P., & Utke, R. (2024). Heat charging and discharging of coupled MgH_2–$LaNi_5$ based thermal storage: Cycling stability and hydrogen exchange reactions. International Journal of Hydrogen Energy, 49, 59–66. https://doi.org/10.1016/J.IJHYDENE.2023.10.312.

Thongtan, P., Thiangviriya, S., Utke, O., & Utke, R. (2022). MgH_2-based hydrogen storage tank: Kinetics, reversibility, and MWCNTs content. Journal of Physics and Chemistry of Solids, 163, 110578. https://doi.org/10.1016/J.JPCS.2022.110578.

Plerdsranoy, P., Thiangviriya, S., Dansirima, P., Thongtan, P., Kaewsuwan, D., Chanlek, N., & Utke, R. (2019). Synergistic effects of transition metal halides and activated carbon nanofibers on kinetics and reversibility of MgH_2. Journal of Physics and Chemistry of Solids, 124, 81–88. https://doi.org/10.1016/J.JPCS.2018.09.001.

Thiangviriya, S., Plerdsranoy, P., Sitthiwet, C., Dansirima, P., Thongtan, P., Eiamlamai, P., Utke, R. (2019). MgH_2–TiF_4-MWCNTs based hydrogen storage tank with central tube heat exchanger. International Journal of Hydrogen Energy, 44(36), 20173–20182. https://doi.org/10.1016/J.IJHYDENE.2019.06.002.

Thongtan, P., Dansirima, P., Thiangviriya, S., Thaweelap, N., Suthummapiwat, A., Plerdsranoy, P., & Utke, R. (2018). Reversible hydrogen sorption and kinetics of hydrogen storage tank based on MgH_2 modified by TiF_4 and activated carbon. International Journal of Hydrogen Energy, 43(27), 12260–12270. https://doi.org/10.1016/J.IJHYDENE.2018.04.171.